INFORMATION TO USERS

This manuscript has been reproduced from the microfilm master. UMI films the text directly from the original or copy submitted. Thus, some thesis and dissertation copies are in typewriter face, while others may be from any type of computer printer.

The quality of this reproduction is dependent upon the quality of the copy submitted. Broken or indistinct print, colored or poor quality illustrations and photographs, print bleedthrough, substandard margins, and improper alignment can adversely affect reproduction.

In the unlikely event that the author did not send UMI a complete manuscript and there are missing pages, these will be noted. Also, if unauthorized copyright material had to be removed, a note will indicate the deletion.

Oversize materials (e.g., maps, drawings, charts) are reproduced by sectioning the original, beginning at the upper left-hand corner and continuing from left to right in equal sections with small overlaps.

Photographs included in the original manuscript have been reproduced xerographically in this copy. Higher quality 6" x 9" black and white photographic prints are available for any photographs or illustrations appearing in this copy for an additional charge. Contact UMI directly to order.

Bell & Howell Information and Learning
300 North Zeeb Road, Ann Arbor, MI 48106-1346 USA
800-521-0600

UMI®

UNIVERSITY OF OKLAHOMA

GRADUATE COLLEGE

CHARACTERIZATION OF ADMICELLAR POLYMERIZED AND OTHER THIN FILMS USING SCANNING PROBE MICROSCOPY (SPM)

A Dissertation

SUBMITTED TO THE GRADUATE FACULTY

in partial fulfillment of the requirements for the

degree of

Doctor of Philosophy

By

Wei-Li Yuan

Norman, Oklahoma

2001

Bell & Howell Information and Learning Company
300 North Zeeb Road
P.O. Box 1346
Ann Arbor, MI 48106-1346

CHARACTERIZATION OF ADMICELLAR POLYMERIZED AND OTHER
THIN FILMS USING SCANNING PROBE MICROSCOPY (SPM)

A Dissertation APPROVED FOR THE
SCHOOL OF CHEMICAL ENGINEERING AND MATERIALS SCIENCE

BY

Bri Grady

Daniel T. Glatzhofer

Robert L. Shambaugh

Edgar A. O'Rear

Acknowledgments

We live in an age of certificate, diploma, medal, and award. It seems everything needs to be proved and certified. However, like a complex number which has the imaginary part and the real part, everything has two aspects, the outward expression and the inward reality.

The Ph.D. work to me is more than outward experiments and dissertation. It is a way to reach the reality of life. In this process I had both good and bad times but they all helped me grow in life. The encouragement, instructions, and support from my advisor Dr. Edgar A. O'Rear were so invaluable and unforgettable to me. I learned a lot from his way of living (and jokes, too). I also want to thank Dr. Robert L. Shambaugh, Dr. Daniel T. Glatzhofer, Dr. Brian P. Grady, and Dr. Melissa M. Rieger for their help in my academic works and being my committee members. I am grateful to Dr. Lloyd L. Lee and Dr. Lance L. Lobban for helping me pursue an academic career. The time I spent with my colleagues from several departments was also enjoyable. I enjoyed exploring scanning probe microscopy with Harry J. Barraza and his friendship. The department staff helped me a lot in many things and I want to thank all of them. Although many names are not listed, I want to let you know each one of you has a part in me and I treasure it and will carry it with me through the life.

My parents Henry and Catherine love me so much and as a son, I have had so little time to be with them and make them happy. My wife Amy and my kids Tiffany and Timothy always make me smile from the heart. I could not wait to see them and give them a big big hug. This dissertation is dedicated to my parents and my family.

Finally, I want to thank the church in Oklahoma City. With Christ as food and drink, I am being recovered in all aspects of my life through eating and drinking of Him in spirit. I pray the church continues to bear the image of God and regain the earth. I also wish the best of the University of Oklahoma and Norman where I had a good taste of America and I will never forget "Oklahoma is OK!"

Contents

List of Tables

List of Figures

Abstract

Characterization techniques and results of polymer and inorganic thin films using Scanning Probe Microscopy (SPM) were presented. In view of principle, equipment and operation of SPM, sample preparation, and surface morphologies of fiber, powder, and thin film were discussed. Techniques of image processing, analysis, and export were described in detail. In view of application, polypyrrole (PPy) films formed on alumina, mica, and graphite by admicellar polymerization showed, using SPM, a film thickness of tens of nm or a few nm under conditions of depleting adsolubilization. Wrinkling of thick PPy films (> 100 nm), mostly prepared in the absence of surfactant, was observed on mica and interpreted as the overcoming of film-substrate adhesion by increased cohesion of the film during its growth. Droplets of an InSb alloy deposited on Si(100) using molecular beam epitaxy (MBE) were found to possess nicks on the surface which were interpreted as the volume change upon solidification. The calculated volume change from AFM images was 2.2% which corresponded to a 13% Sb in the alloy and agreed well with the value (16%) obtained from EDAX analysis. Effects of annealing on CaF_2 thin films deposited on Si(100) were examined by SPM and the results showed that the crystalline CaF_2 flattened and widened after annealing and that undesired polycrystals within the film promoted the formation of amorphous CaF_2.

Chapter 1

Scanning Probe Microscopy

1.1 SPM: Introduction

1.1.1 SPM: Equipment

The test section of the microscope is composed of three parts, simply put, the head, the neck, and the body of the microscope (Fig. 1.1: top row). The scan 'head' comprises four elements: a laser diode (emitter) on the right, a photodiode (receiver) on the left next to a mirror, and a scanning probe (the tip) at the center (reflector). Before scanning, a laser beam path is established which links all the four elements (Fig. 1.2). The beam goes left from the emitter and is reflected downward by a prism located at the top center. The downward beam hits the top side of the probe cantilever when it is reflected again. Because the probe substrate is forwardly inclined (leftward in the diagram) by an angle of 10 °, the laser beam moves up toward a mirror on the upper left to be reflected for the third time toward the photo-detector. During scanning, the tip either vibrates or bends, but does not move about. The local displacement of the tip shifts the beam path and causes the laser spot on the photo-diode to fluctuate. Therefore, any minute change of interaction between the tip and sample will be sensed and recorded by the photo-detector.

The fixed prism, relatively small in size, is designed to deflect the incident beam by 90° based on a total internal reflection without energy loss. In contrast, the mirror is designed to catch the reflected beam with a wide range of possible incident angles from various probes and to keep the movement of the beam received by the photo-detector proportional to that of the scanning tip, which cannot be achieved by replacing the mirror with a large prism.

The 'neck' or the scanner is a piezotube, which supports and moves (scans) the sample. The maximum scan area depends on the size of the piezotube. The 'body' or the microscope base comprises LED panels outside and electronic boards inside. From the body, the scan head is supported by three screws (two at the front and one at the back) for adjusting the separation between the tip and sample. A stepper motor embedded inside the body connects the rear screw for either automatic or manual raising of the head.

In addition, one controller box (with a control monitor) and one computer (with a display monitor) are connected with the microscope for scanning and processing images, respectively (Fig. 1.1: c). A thermal (dye-sublimation) printer for printing photo-quality images (Fig. 1.1: c), an monocular optical microscope (25 ×) for viewing and lowering the tip from the side (Fig. 1.1: e), and a binocular microscope integrated with a video camera (350–800 ×, based on a 900–400 μm view displayed on a 13" tip monitor) for locating the tip and viewing the sample from the top (Fig. 1.1: d) complete the main part of an SPM system.

In order to control the ambient humidity and isolate vibrations and noises, a closed plastic box with desiccant is used to store the scan heads and samples; a double walled, heavy, plastic, and bottomless box is used to cover the microscope body together with desiccant and a hygrometer to reduce noises and humidity; a pneumatic vibration isolation table is used to damp low-frequency vibrations (Fig. 1.1: e). The temperature in the room is automatically controlled and normally set to 78 °F.

1.1.2 SPM: Operations

The scanning probe microscope (SPM) is very similar in principle to a phonograph in which a stylus is physically touching the surface of a record (sample) placed on a turntable (piezotube) for rotation (scanning) and varying electrical signals (laser spot movement) transmitted by the tonearm (cantilever) along the spiral groove (raster tracks) are finally converted to sound (image). The SPM system in our lab is a NanoScope III, Multimode SPM. The words 'scanning probe' abbreviated in 'SPM' depict a tip above or in contact with the sample moves line by line along the surface, resulting in a square array of height data. The word 'multimode' means our SPM system can perform scanning tunneling microscopy (STM), contact mode atomic force microscopy (CMAFM), TappingMode atomic force microscopy (TMAFM), and lateral force microscopy (LFM). All except for STM belong to the category of atomic force microscopy (AFM) in which the interaction forces between the tip and the sample are detected. In STM, a tunneling current between the closely separated tip and a conducting sample is established and measured. Considering all detectable interactions between the tip and sample as generalized 'forces', the surface map will become a generalized 'morphology'. For example, if the chemical interaction between a functionalized tip and a sample is to be detected, chemical force microscopy (CFM) is obtained, and the image is a map of hydrogen bonding or hydrophilicity; if the magnetic force is to be recorded, magnetic force microscopy (MFM) arises; if the temperature gradient is to be measured, scanning thermal microscopy (SThM) is derived. Forces reported sensed by a scanning probe (with different designs) include coulombic, van der Waals, capillary, fluid damping, electrostatic, magnetic, capacitance, temperature, near-field optical, and tunneling 'forces'.

One of the two operation modes can be selected for each working 'force', namely, the constant force and the varying force (constant separation). The mode of constant force keeps the 'force' between tip and sample constant by maintaining a constant deflection of the tip (CMAFM), amplitude of the tip (TMAFM), or current through the tip (STM). To do this, a feedback loop is used by setting proper gains during the scanning. In contrast, the varying force mode set a constant separation between the tip and sample during scanning and record the changes of tip deflection, amplitude, or current. This varying force mode is suitable for smooth or atomic-scale imaging with fewer chances to crash the tip.

1.1.3 Laser Tuning

In order for the SPM to respond sensitively to the scanned sample surface, the emitted laser beam needs to be properly focused on the reflecting probe and the receiving photo-detector. Each time the probe is changed, the laser beam has to be re-focused. There are three parts in the scan head needed to be tuned in order to reach an optimal (close to maximum) output signal received by the photo-diodes: the laser x-y positioner, the mirror, and the diode positioner. Based on experience, useful procedures of focusing the laser beam after changing a new tip will be described in Appendix A on page 164.

1.1.4 Structure of Photo-Detector

After focusing the laser beam on the cantilever, and whenever a laser positioner is fine adjusted, the lateral and vertical photo-diode positioners need to be tuned for the contact mode and TappingMode AFM scan heads, respectively. The reason is explained based on the structure of the photo-detector.

The photo-detector has a set of quadruple photo-diodes (Fig. 1.3). The top two diodes are normally named A and B and the bottom ones, C and D. Assuming the laser beam was focused on the center of the detector at the beginning, $\textit{signal } A + \textit{signal } B = \textit{signal } C + \textit{signal } D$. If the spot moves up, $A+B > C+D$. If the spot moves to the right, $B+D > A+C$. Therefore, $(A+B)-(C+D)$ detects the up and down of the laser spot while $(A+C)-(B+D)$, the left and right. They are shown in the top and bottom LED panels on the microscope body, respectively. $A+B+C+D$ gives the sum signal as shown in the elliptical bar in the bottom LED panel.

In contact mode, changes of $(A+B)-(C+D)$ during scanning refer to the deflection of the tip, giving the line profiles of the scanned surface. Normally, $(A+B)-(C+D)$ is set to a value between -1 and -4 V before starting tip engagement and allowed to increase to a specified value called the setpoint to trigger the scanning as the tip is being lowered and bent. The difference between the initial and setpoint values is proportional to the forces applied by the tip to the sample. For soft materials, a smaller initial value of $(A+B)-(C+D)$ is used while keeping the setpoint normally at 0. When the laser spot is close to the center of the diode assembly, the detector will be the most sensitive. This is the reason to maintain the setpoint at 0 during scanning.

Changes of $(A+C)-(B+D)$ during scanning represent the lateral twisting of the probe, which is useful in detecting the frictional interactions between the tip and sample. For topographical and frictional imaging, $(A+C)-(B+D)$ is typically adjusted to 0 before tip engagement. For TMAFM, the scan head is different with no B and D diodes because the vibrating tip should not be twisted during scanning. However, the initial $A-C$ shown in the bottom LED panel still needs to be set to 0 for higher detector sensitivity.

1.1.5 SPM Calibration

The SPM system needs to be calibrated once per several months. The calibration normally requires a calibration grid with fixed pitch and depth. For a J scanner (125×125 μm^2 capacity), a grid with a 10 μm pitch and a 180 nm depth is used (Fig. 1.4: top). Detailed procedures are described in the manual [1], but several typical images captured during calibration are shown in Fig. 1.4: bottom and Fig. 1.5. Normally, a series of images with distorted features will be captured in real-time mode, and then analyzed interactively in off-line mode.

Note in Fig. 1.4: bottom, the upper left portion is not well imaged because the tilting of the grid causes a larger separation between the tip and sample. Sometimes no features are shown in the whole image so that the image becomes useless. If this happens at the beginning of the calibration process, one can move the tip via the control panel to a new location on the sample. If this happens during calibration, one can choose to abort or 'skip' the image and the computer will capture a new one. If a useless image has been captured, one has to wait until the end of calibration and recapture that particular image.

1.2 SPM: Probes

The components of an SPM probe and the associated force constants will be described as follows. Matters concerning probe cleaning and tip handling are presented in Appendices B and C.

1.2.1 Structure

SPM utilizes a physical probe to track the sample morphology. The probe is normally called a 'tip'. A CMAFM tip consists of three parts: substrate, cantilever, and crystal (Fig. 1.6: a). The triangular part shown in the image is called the cantilever whose elasticity (quantized as the force constant) renders an 'atomic force' to the sample. The base of the cantilever as shown in the lower right of the image is called the substrate of the tip. Probes are manufactured out of a silicon wafer (Fig. 1.7) and are broken off with tweezers. The individual pieces seen in the bottom wafer (TMAFM tips) are the substrates.

The STM tip is like a needle (Fig. 1.6: b) generally made of Platinum-Iridium (Pt/Ir) wire cut with a little twisting to form one or several sharp apexes at the free end. Tunneling electrons are emitted from the apex closest to the sample. An STM tip can also be made by etching a tungsten (W) wire in an electrochemical cell for atomic level imaging. However, oxide may form quickly on the tip, depending on the material, so it can not perform well for long. The 'recipes' can be found in the manual and elsewhere [1–5].

In addition to a triangular cantilever, a single beam 'cantilever' with different lengths can be made as seen extending from the substrate under an optical microscope (Fig. 1.6: c–d). The triangular cantilever is also called a 'V-tip' while the single beam one, an 'I-tip' according to the shape. The extent of deflection or vibration of the cantilever and the material properties determine the forces exerted on the sample. Therefore, the resonant frequency, vertical (bending, deflective) force constant (k_N), and lateral (twisting, torsional) force constant (k_L) are the three most important parameters to be determined if tip-sample interaction is going to be clearly quantized in units of force. The top side of a V-tip is coated by a layer of gold to better reflect the incident laser beam to the photo-detector. Recently, I-tips are also coated by aluminum or other materials to increase the reflection.

Located close to the free end of a cantilever, a small crystal of Si_3N_4 or Si (shown as a dark point) is found attached, extending out in a direction perpendicular to the cantilever's bottom side with a very sharp apex at its end (Fig. 1.6: a, c–d). The crystal or the real 'tip' may be pyramidal, tetrahedral, or conical in shape, depending on the milling process adopted. The radius of curvature of the crystal apex can be as small as 5 nm. Since the contact area of the apex with the sample will be very small, any negligible force between the substrate and tip may still create a large pressure to either break the tip or damage the sample.

SPM tips have been manufactured in various sizes and materials for different purposes. Intuitively, the longer/narrower/thinner the cantilever, the smaller the resonant frequency and the spring constant. The location of the crystal on the cantilever is different from tip to tip and it is especially important to know if an exact position on the sample is desired as seen in scanning the top portion of a fiber surface.

The position of the crystal in the V-tip is usually very close to the free end of the cantilever (Fig. 1.6: a) while that of an I-tip is usually between the free end and the intersection point of the cantilever long axis with the line connecting the two corners beside the free end (Fig. 1.6: c–d). During scanning, the crystal is hidden beneath the cantilever, but its location is indicated on the top side by a reflectively bright spot for a V-tip or the intersection point of an I-tip.

1.2.2 Property: Force Constant

The deflection and vibration of a cantilever can be modeled as a spring-mass system following the Hooke's law or performing simple harmonic motion. More complicated rheological models for describing material behavior using springs (elastic and energy conserving) and dashpots (viscous and energy dissipating) in serial or parallel combinations are frequently taken to simulate the motion or dynamic deformation of the scanning probe or the scanned sample (expressed by differential equations of position with respect to time) in different scan modes [6]. A spring comes with a spring (force) constant which represents the stiffness or elasticity of the spring (the probe in SPM). If the vertical force constant is known, the vertical (normal) force of the tip can be calculated from the relation

$$F_N\ (nN) = k_N\ (N/m) * \Delta z\ (nm) \tag{1.1}$$

where F_N is the vertical force and Δz is the vertical deflection.

If the torsional force constant is known, the frictional force between the sample and tip can be calculated by a similar relation

$$F_L\ (nN) = k_L\ (N/m) * \Delta x\ (nm) \tag{1.2}$$

where F_L is the lateral (frictional) force and Δx is the lateral torsion. Detailed formulae for calculating the force constants based on different probe geometries can be found in Ref. [7,8].

1.3 Sample Preparation

Proper sample preparation is the first key to successful SPM results. Good images always come from good samples. Sample preparation depends strongly on the shape, structure, and features of the samples. For example, powders and fibers require firm fixation on the sample holder to facilitate good imaging. Polymer films formed on solid by admicellar polymerization result from several experimental steps and care needs to be taken not to damage the sample surface during preparation.

1.3.1 Mounting the Sample

After the sample is ready, it can be mounted onto a steel sample holder or puck using glue or polymer clay (Fig. 1.8). It is not easy to remove the glued sample from its holder. If the sample is going to be used somewhere else, polymer clay will serve as a good alternative, offering desired weak adhesion to the sample, long working lifetime, and good plasticity to reduce sample drifting and compensate sample tilting. One can also glue a piece of self sticker ('Post-It') to the steel puck with its pre-glued side facing up. The weak-glue side makes repeated mounting and removing samples very easy. Samples can also be fixed on the holder with a drop of fingernail paint or sometimes even without using any glue.

1.3.2 Mica

Mica is a kind of aluminosilicate and has lamellar structures. Each mica lamella consists of two tetrahedral silica sheets with one octahedral alumina sheet sandwiched in between (Fig. 1.9: a–c). Between the lamellae exist K^+, Li^+, Na^+, and other cations which balance the negative lattice charge.

Mica can be easily cleaved with a razor blade to expose atomically smooth surfaces for deposition of thin films or other materials to be studied by AFM. Mica has become a standard sample for AFM imaging and calibration. Atomic scale images of mica can be obtained by contact mode AFM/LFM in air without much difficulty in a proper environment (Fig. mica-afm). Normally only pairs of silica groups can be resolved. As shown in (Fig. 1.9: a–c), the hexagonal rings of tetrahedra on mica surface render a three-fold pattern if each group is to be resolved. However, only two groups altogether can be resolved, which leads to a six-fold pattern in AFM images (Fig. 1.10). The pattern spacings are shown in (Fig. 1.9: d).

Mica is hydrophilic in nature and the surface is normally negatively charged. The contact angle of water is reported as 7° [9]. In solution, mica is able to exchange cations or cationic molecules at the intercalary sites, leading to a change in surface charge. In ambient environment, mica is covered by thin layer of water condensed from the air. The capillary force between the SPM tip and water layer on the sample may result in loss of image quality. To obtain atomic images of mica, sharp tips are indispensable and different scan angles may be tried in order to resolve the best atomic pattern.

1.3.3 Graphite

Graphite is another important standard sample commonly used in SPM study. Researchers prefer one kind of graphite called the highly oriented pyrolytic graphite (HOPG) which is highly crystalline and pure but very expensive. Since HOPG is also lamellar in structure, adhesive tape can be used to peel the top layers of HOPG to render fresh surfaces for repetitive use. HOPG is slippery to the touch and highly hydrophobic. The contact angle of water is reported as 89 ° [9].

The crystalline structures and the atomic spacings revealed by SPM are shown in Fig. 1.11. HOPG consists of layers of carbons in three-fold or honeycomb-like patterns. Due to its lamellar structure and pi electrons, HOPG is electroconductive two dimensionally and low in shear resistance. The conductivity (S/cm) of graphite in rod or other forms is on the order of 10^3 as reported in the catalogues of several chemical companies. Both STM and CMAFM images of HOPG have been successfully scanned (Fig. 1.12). Similar to mica, individual carbon atoms are not readily resolved by STM or AFM. Normally the overlapped carbons of the first and the second layers are resolved [2,4]. The hexagonal rings (three-fold in pattern) are usually resolved as three spots and thus lead to a six-fold pattern. However, filtered images show nice honeycomb structures. In STM scanning, a conductive path needs to be built using silver epoxy glue connecting the edge of HOPG and the steel puck. According to the manual, when scanning HOPG using STM in constant current (force) mode, the 'Z limit' parameter in the control panel should be reduced to about 55 V for better results [1].

1.3.4 Inorganic Thin Films

Inorganic materials mainly include semiconductors, metals, oxides, salts, and silicates. If processed into films, their crystalline structures on different substrates can be easily studied by SPM in/ex situ under vacuum or ambient conditions.

Surfaces are normally different in structure from their bulk. Surface structures may be determined either by the reconstructed bulk atoms or by adsorbed atoms different from the bulk. Since SPM works on surface morphology at microscopic levels, it is important to understand how to express the orderly patterns of a surface. Ni(100)-$(\sqrt{3} \times \sqrt{3})R30^\circ$-CO is an example of describing the surface structures where nickel is the substrate material; (100) is a Miller index of the Ni surface; $(\sqrt{3} \times \sqrt{3})R30^\circ$ represents the adsorbate (CO) structure with respect to the substrate surface [10].

Thin semiconductor films deposited by molecular beam epitaxy (MBE) exhibit substrate-dependent morphologies. Long parallel ridges [11] are observed on Si(110); triangular protrusions (Fig. 1.13: top left) on Si(111); elongated pyramidal clusters and pits together with polycrystals on Si(100) (Chap. 5). Defects due to post-growth annealing such as amorphous aggregates (Chap. 5) and cracks (Fig. 1.13: top right) can be clearly revealed by SPM. In addition to constant force images, lateral (frictional) force and varying force images are captured for multilayered films (Fig. 1.13: bottom row). On the left, a top layer with an exposed sub-layer is shown in 'height' data (constant force) based on height changes of the surface. On the right, the edges of the top layer is shown in 'deflection' data (varying force mode) based on sharp slope changes of the surface. In the middle, the frictional signals showing the two layers are of different materials, based on changes of sliding resistance to the scanning probe.

Metallic films can be imaged easily using either AFM (Fig. 1.14: top) or STM (Fig. 1.14: bottom) in ambient conditions. The top image is the surface of a nickel foil which shows long grooves and ridges due to the manufacturing process. Normally, hard samples can be imaged without problem using AFM over a wide force range. The bottom image is a layer of compressed nickel powder against a wax film (insulating) and a conduction path must have been built through the grain boundaries for STM to work.

Force Calibration Curve for CMAFM

One important step in running CMAFM is to obtain the force calibration curve for the value of tip sensitivity (Fig. 1.15: top). Tip indentation and lateral force microscopy (LFM) are also based on this operation. The curve records the deflection of the tip during its journey of approaching, touching, and withdrawing from the sample surface. Deflection of the tip can be converted to real force (the normal force) if the force constant of the tip is known.

The tip starts far away from the surface and the force curve can be divided into several parts (Fig. 1.15: top). As the tip approaches the surface from afar (extending of the piezotube), no deflection, thus a flat curve, is observed because of no sensed force between the tip and sample (section 1). When the tip gets close enough to the surface, the tip will be bent downward due to the sensed attraction, and finally jump on the surface with downward deflection as indicated by the small jump-on point at the left end of section 1 before the rising of the curve (point 2). After the contact of the tip with the surface, the lowering of the tip (actually, the raise of the sample in our system) restores the tip back to its non-deflected state and goes on to bend the tip upward due to the repulsion between the tip and the surface (section 3). Some deformation or indentation of the surface may be temporarily or permanently created (depending on the sample material) during the physical contact of the tip.

In the withdrawing process (retracting of the piezotube), the repulsion decreases and the tip changes from upward deflection to a very much downward deflection as indicated by the portion of the retracting curve below section 1 (section 5). This is due to the attraction of the sample and especially the capillary force between the tip and the adsorbed water layer on the surface. The tip will not be released until it reaches a pull-off point where the tip suddenly snaps back to its non-deflected state (point 6), because, at this point, the tip should have moved far away from the sample were it not for strong adhesion. Ideally, fixing the setpoint in section 5 means a small attractive force (non indenting) between the tip and sample. However, the tip may become unstable and very often snap up from the surface. If deformation is negligible, using repulsive force to obtain good images will work normally.

A sample surface is often casually termed hard, soft, elastic, plastic, or sticky. In a typical stress-strain diagram, a hard sample may have a narrow elastic region so an indentation is easy to form. A soft material may have a wide elastic region not to be readily deformed. Stickiness is normally a mixed effect of many kinds of force. If the sample is sticky, the region of attraction may be enlarged abnormally (Fig. 1.15: bottom). The slope (df/dz) of the inclined segment of both the extending and retracting curves is called the sensitivity of the photodetector. The accuracy of the varying force data depends on this value, which can be measured directly on the display monitor using the software. Both df and dz, formed between the no-contact flat line and the setpoint line, are related and represent the amount of force exerted by the tip on the sample. The value of df is obtained first from the voltage change detected by the photo-diodes and shown in the LED panel on the microscope body. Then df is converted into dz through the sensitivity factor. Multiplying dz by the tip force constant (Eq. 1.1) gives a number in real force units

$$F_N\ (nN) = k_N\ (N/m) * \Delta z\ (nm) = k_N\ (N/m) * \Delta f/sensitivity\ (nm). \quad (1.3)$$

Note the 'tip deflection' represented by the vertical axis of the diagram is actually the signals received by the photo-detector and can also be expressed in voltage. However, the real and physical tip deflection is equal to the piezotube movement, represented by the horizontal axis.

Rough Surface

When the surface under scanning is smooth, withdrawing the tip can be done in one or two mouse clicks on the software control panel and the rear screw will be rotated up by the stepper motor and raise the whole tip/scan head assembly. However, if the surface is rougher, raising the tip with the rear screw alone will easily crash the tip on the surrounding higher regions. Similar to tip lowering, when the tip is raised vertically, it is also displaced laterally. In this case, it is better to raise the two front screws altogether manually and then raise the rear one by mouse clicking.

1.3.5 Fiber

A fiber is generally circular in its cross section (Fig. 1.16). Therefore, fibers under the scanning tip can most of the time be rolled due to the lateral movement of the piezotube. Engaging the tip on the side of fiber will bend the tip significantly and damage it when the scanning starts. They can be fixed on the substrate by several methods. A small piece of polymer used in a household 'glue gun' can be put on the steel puck. Melting it with a heater will spread it and provide a non-sticky polymer substrate to the scanning tip after cooling down to the room temperature. Several fibrils can be put on such a half molten substrate and slightly pressed into the polymer matrix by a cold smooth metal plane which will not harm the embedded fibrils and will quench the polymer in no time. In this way the top portions of fibril will be more easily located by the SPM tip and the polymer substrate will not contaminate the tip.

In order to land the tip on top of the fiber, efforts and patience are required in repetitive engaging and withdrawing the tip, moving the sample around with the sample x-y positioners, changing and tuning new tips, and so on. The tip monitor and knowledge of the crystal position on the tip are indispensable in fiber scanning. Both CMAFM and TMAFM work well on fiber.

Offset and Centering the Fiber

When the tip is located in the top portion of the fiber without bumping into the sides, fine tuning of the tip position can be done through using the software real-time function 'offset' to laterally move the highest portion of the surface to the center of the image. At the same time the real-time image should be processed in 'offset' mode (plane fit) instead of 'line' mode (flatten) with which the image will be fully flattened so that the high portion of the fiber cannot be identified and the probe may still be scanning the side portion of the fiber, leading to tip artifacts. Note the first 'offset' is to move the sample around while the second 'offset' retains the tiling of the surface in the real-time image. A detailed explanation of plane fit and flatten functions can be found in Appendix D.

Scan Angle and Perpendicular Scan

In scanning a fiber, the scan angle is better set to be perpendicular to the fiber long axis in order to find the highest portion across the fiber. Increasing the scan angle in the control panel will rotate the real-time SPM image counterclockwise while rotating the fiber shown in the tip monitor clockwise with respect to the tip.

Control of the Stepper Motor

The stepper motor is connected with the rear screw for automatically or manually raising or lowering the tip and the whole scan head. The stepper motor movement can be controlled through the control panel. Each rotation comprises two withdraw clicks by mouse and equals 10 μm. However, each click may not necessarily give a 5 μm rise of the rear screw, but successive two clicks will mostly give 10 μm movement. Whenever the tip is first engaged to the surface from afar, it is better to withdraw the tip by 1 or 2 clicks and adjust $(A + B) - (C + D)$ diode signals to the desired value before reengaging the tip.

The second way to move the tip by stepper motor is set the desired step distance and direction to be done with each mouse click through the 'stepper motor' control panel. The third way is to turn the stepper motor switch on the SPM base manually. The exact traveling distance of the tip using this method is controlled loosely. Stepper motor movement is important in lowering the tip and applying a specified amount of force on the surface in LFM and indentation experiments.

1.3.6 Powder

A powder usually has spherical shape, rough surface, and small size. In order to apply SPM to powders successfully, the powder needs to be fixed on the sample holder as in the fiber case. One popular way to fix a powder is to press a layer of sparingly spread powder into a wax film and glue the film to the steel puck for imaging (Fig. 1.17: top). If the amount of powder is too great, after compression the particles may be deformed and the surface may become flat (Fig. 1.17: bottom). Scanning powder also requires several trials of engaging and withdrawing the tip for landing on one individual particle with a smooth portion of surface facing up.

1.3.7 Polymer Thin Films

Polymer thin films, like PPy and polystyrene, can be deposited on mica or graphite with or without surfactant present. After deposition and drying films can be studied by AFM directly.

Admicellar Polymerization

Admicellar polymerization includes four steps: surfactant adsorption, monomer adsolubilization, initiator/oxidant polymerization, and film rinsing (Fig. 1.18). Polymer thin films are formed in this process on a solid surface in contact with an aqueous phase. Polymers can be insulating or electroconducting. Solid substrates can be powder, fiber, or plate. The polymer-coated solid exhibits different surface properties and can be used in composites to enhance interfacial adhesion or electrical conductivity. Deposition of electroactive polymer thin films on solid may be used in semiconductor devices or electrochemical sensors, opening a new realm of polymer application.

Depleting Condition

Wu et al. found that monomer in the supernatant can move to the interface and contribute to polymer formation [12, 13]. In order to eliminate the effect on thin film growth of monomer in the solution phase during admicellar polymerization, depleting monomer conditions can be applied by using separate monomer solution and oxidant/initiator solution (Fig. 1.19). Such environments are especially suitable for making thin films on flat, nonporous solids with small surface area.

Tapping Mode for Polymer Films

Polymer films are best resolved using TMAFM. Films will usually be deformed in CMAFM. In using TMAFM, the tip is set to be falsely engaged before it physically touches the surface. This is done by setting a value ~ 1.5 for the 'engage setpoint'. After the tip starts scanning 'in the air', the setpoint can be slowly decreased while increasing the force of the tip on the sample until clear or meaningful images are seen. At this point the tip exerts a minimum amount of force on the sample with the least deformation to the sample. This same idea of the slightest touch has been successfully applied to image the vulnerable surfactant aggregates on solid in solution by several research groups [14,15]. Before the appearance of clear images, noisy and obscure images are observed based on the forces sensed by the probe. If an investigator is patient and careful, meaningful interpretations may be made about the low force induced images. Fig. 1.20 shows a few regions with the tip in slight or normal contact with the sample, the former condition giving no obvious surface features though.

After the first false engagement of the tip, one should withdraw the probe by a few mouse clicks and reengage the tip again. This approach will ensure to restart lowering the tip from within a short distant above the sample, help determine the desired forces applied to the sample, and avoid crashing the tip because the tip will also move laterally before landing on the sample.

Cantilever Tune

Cantilever tune is an important step to take before TMAFM can be run. The purpose of cantilever tune is to find out the resonant frequency (f_0) of the cantilever and determine the amplitude or the force to be exerted to the sample. Typical curves in cantilever tune are shown in Fig. 1.21. Each curve is a spectrum of the driven amplitude of the tip vs the driving frequency of the bimorph, a piezoelectric crystal used to vibrate the tip. The largest peak representing the resonant frequency needs to be identified. Normally, the driving amplitude is set to a value which results in 3 to 5 V in the output root-mean-square (rms) amplitude signal of the tip as shown in the top LED panel. The driving amplitude is the amplitude of the piezoelectric bimorph which vibrates the tip while the output amplitude is the amplitude of the driven cantilever. The input and output amplitudes are not the same but the driving frequency of the bimorph can be 'tuned' to be the same as the driven frequency or the resonant frequency of the cantilever, which is the meaning of cantilever 'tune'.

The reason for tuning to a resonant frequency is to obtain the largest driven tip amplitude at a particular driving bimorph amplitude, otherwise the tip will hardly vibrate and the system will become contact mode. If the output amplitude signal is too small, the tip sensitivity (the signal to noise ratio or the Q factor) will be reduced and if the setpoint is also not low enough the imaged surface will seem to be like mountains covered by clouds, so to speak. That is, the tip may not be able to reach the low regions of the surface. If the signal is too large both the tip and the sample may be damaged or worn out quickly by the strong interaction force.

In the frequency spectrum, double peaks will lead to double images, i.e., all the features in the image will be duplicated and separated at small distance. This typically means the tip is broken, contaminated, or misaligned. One can try to realign or slightly change the position of the tip in the tip mount. Cleaning the tip mount groove will also help eliminate the double peaks. If none of the above works, the tip is replaced with a new one.

Feedback Loop Gains

The most important feedback loop gains are the integral and proportional ones. Normally, the integral gain alone will determine the quality of the image. The integral gain for TappingMode ranges from 0.3 to 0.5 and the proportional gain is normally set to 1.0. High gains produce fuzzy or wavy images but low ones, blurred images.

Scan Rate

The scan rate for TMAFM is normally 0.5 to 3.0 Hz, depending on the scan size and roughness of the surface. One μm normally marks the boundary of macroscopic and microscopic worlds. At a small scan size, if the scan rate keeps increasing, images will become noisy and unstable. Even if the scan rate is below 3 Hz, large scan size above 5 μm will also cause 'trailing tails' pointed to the same direction associated with each tall feature on the surface.

In summary, if you do not see the valleys of the surface, increase the force by changing the setpoint or driving amplitude. If you do not see the details of the surface, increase the gain. If you see trailing tails, decrease the rate. If you see repeated features of the same shape but with different size, replace the tip. If you see double images, adjust the tip position in the tip mount.

1.4 Image Artifacts

Tip artifacts are commonly seen and may result in wrong interpretation of the image. The scanning tip may be fractured, broken, blunted, and contaminated. Some other scanning parameters such as scan rate, scan size, feedback gains, and force magnitude may aggravate the tip artifacts or introduce non-tip artifacts. Some example images with artifacts are give as follows.

1.4.1 Double Image

Double image (or double-tip image) is one with so called ghost shadows (Fig. 1.22). It looks like two same images overlapped at a small offset. Normally, it is caused by split tips due to manufacturing defects or damage on scanning. Sometimes a contaminated tip also produces double images because the attached material (usually small particles) serves as a second tip or multiple tips (Fig. 1.23: top). In this case, the tip performance may be restored after cleaning. However, if the tip is broken, replacement is the only way.

1.4.2 Repeated Structures

When a tip is broken due to crashing into the sample or improper handling, a split tip or blunt tip may appear. The former case has been discussed in the previous section. For a silicon tip normally used in TMAFM, the fracture surface will resemble a triangle. Whenever repeated triangles with different sizes appear in the image, the tip is most probably broken (Fig. 1.23: bottom) and replacement with new tip is needed. Sometimes, a sudden loss of resolution also indicates a broken tip. For a silicon nitride tip used in CMAFM, since its hardness is higher than silicon, it normally wears out instead of breaking. However, repeated structures and low resolution are still useful criteria. In addition, even an STM tip can produce repeated structures due to crashing or blunting of the tip.

1.4.3 Dilated Features

The reason for repeated structures being scanned discussed above is that the tip is broken and becomes coarser at the crystal apex than the features to be scanned. Therefore, the tip instead of the sample features is scanned. Commercial calibration samples made of sharp and tall features are frequently used to scan the tip morphology. Because of this, for fine surface features, such as small particles of nanometer size, their images are usually 'dilated' (increase in lateral size) unless a known sharper tip is used. Both the tip blunting and surface roughness contribute to the image dilation.

If the surface features are tall (such as a fiber) or deep (such as a porous surface), the dilation effect makes the fiber wider and the pores shallower. Therefore, the radius of curvature of the crystal apex and the half-cone angle of the crystal determine the dilation artifacts for fine and tall/deep surface features, respectively.

1.4.4 Noisy Image

If the tip is not contaminated by a hard particle, but by some sticky or adhesive material, the image may become full of noise instead of doublets. The kind of image artifacts are mostly seen in soft samples like polymer films. Sometimes the contamination is not permanent. If the tip moves away due to scanning from the sticky point of the surface, the pulled material may snap back from the tip, causing several noisy (bright) lines in the image. Such temporary contamination may be alleviated by adjusting scanning parameters such as the magnitude of forces used or the scan rate. Sometimes the contamination is permanent that the tip picks up some material with it throughout the rest of scanning, resulting in a messy image. In this case, the tip needs cleaning or replacement. Sometimes new samples are needed.

1.4.5 Trailing Tails

For a surface with particles or tall features, sometimes trails pointing to the same direction (left or right, depending on the fast scan direction) beside the features are found. Normally, reducing the scan rate will do the best to eliminate such artifacts.

Increasing the interaction force between the tip and sample (by increasing the tip deflection or amplitude) may help reduce the trailing, too. Sometimes the feedback gains need to be increased.

1.4.6 Fuzzy Features

If the gains are set too high, fuzzy patterns will appear, starting from the sharp edges of the surface. Sometimes the fuzzy line size is about the same order of magnitude as that of the surface features, leading to confusing results. Reducing the feedback gains will eliminate such artifacts.

1.4.7 Blurred Features

If the gains are too low, fine features will be missing and the image will look blurred. Increase the feedback gains until the image becomes fuzzy, then reduce the values to reach the optimum sensitivity of the feedback loop with respect to the scanned sample.

1.4.8 Blank Image

If no image is seen after tip engagement, either the color range used to represent the surface heights (i.e., the z range) is too large, or the tip is still away from the sample surface with no deflection or amplitude change. In the latter case, change the setpoint or lower the tip using the stepper motor to draw the tip closer to the sample surface and gradually show morphology.

1.4.9 Banded Image

Sometimes an image with alternating bright and dark bands (not necessarily straight, vertical, or horizontal) mingled with the surface morphology is observed. This is explained by the interference of reflected laser in comparable intensities from the probe and the sample. To reduce the interference effect or perception, a tip with a better reflective coating or a sample less shining should be used. Adjusting the $x-y$ laser positioners to decrease the spill of laser over the probe onto the sample can effectively eliminate interference bands.

1.4.10 Processed Image

Improper image processing (modification) can introduce substantial artifacts to the image. This topic is discussed in Appendix D.

1.5 Conclusion

After an image is captured and modified properly, it can be analyzed through the off-line operations of the SPM software and converted into a common computer graphic. Details of image analysis and format are described in Appendices E and F. Several important aspects of SPM have been covered so far, including sample preparation, sample scanning, image processing/analysis/export, and image artifacts. There is still one more important topic not discussed, which is the interpretation of SPM images. To correctly explain what is observed in the SPM images, a good understanding of the SPM principles, as well as the physics and chemistry of the samples are needed. However, SPM sometimes brings us new and exciting results that are beyond our expectations, so an open mind is also important in image interpretation. Constant review of SPM images and works published by others certainly enhances the ability to interpret images.

Bibliography

[1] NanoScope Command Reference Manual, Digital Instruments, Santa Barbara, CA, 1997.

[2] R. Wiesendanger, Scanning Probe Microscopy and Spectroscopy: Methods and Applications, Cambridge University Press, Cambridge, Great Britain, 1994.

[3] S.-i. Park, R.C. Barrett, in: J.A. Stroscio, W.J. Kaiser (Eds.) Scanning Tunneling Microscopy (Design Considerations for an STM System), Academic Press, Inc., San Diego, CA, USA, 1993.

[4] S.N. Magonov, M.-H. Whangbo, Surface Analysis with STM and AFM : Experimental and Theoretical Aspects of Image Analysis, VCH, Weinheim, FRG, 1996.

[5] G. Rohrer, in: D.A. Bonnell (Ed.) Scanning Tunneling Microscopy and Spectroscopy: Theory, Techniques, and Applications (The Preparation of Tip and Sample Surfaces for STM Experiments), VCH, New York, New York, USA, 1993.

[6] N.A. Burnham, G. Gremaud, A.J. Kulik, P.-J. Gallo, F. Oulevey, J. Vac. Sci. Technol. 14 (1996) 1308.

[7] D. Sarid, Exploring Scanning Probe Microscopy with Mathematica, John Wiley & Sons, Inc., New York, 1997.

[8] B. Cappella, G. Dietler, Surface Science Reports 34 (1999) 1.

[9] J.-F. Liu, W.A. Ducker, J. Phys. Chem. B 103 (1999) 8558.

[10] G.A. Somorjai, Introduction to Surface Chemistry and Catalysis, John Wiley & Sons, Inc., New York, USA, 1994.

[11] W.K. Liu, X.M. Fang, W.L. Yuan, M.B. Santos, T. Chatterjee, P.J. McCann, E.A. O'Rear, Journal of Crystal Growth 167 (1996) 111.

[12] J. Wu, J.H. Harwell, E.A. O'Rear, Langmuir 3 (1987) 531.

[13] J. Wu, J.H. Harwell, E.A. O'Rear, J. Phys. Chem. 91 (1987) 623.

[14] S. Manne, J.P. Cleveland, H.E. Gaub, G.D. Stucky, P.K. Hansma, Langmuir 10 (1994) 4409.

[15] E.J. Wanless, W.A. Ducker, J. Phys. Chem. 100 (1996) 3207.

[16] D.T. Griffen, Silicate Crystal Chemistry, Oxford University Press, Inc., New York, 1992.

[17] A.W. Adamson, Physical Chemistry of Surfaces, 5th Ed., John Wiley & Sons, Inc., New York, 1990.

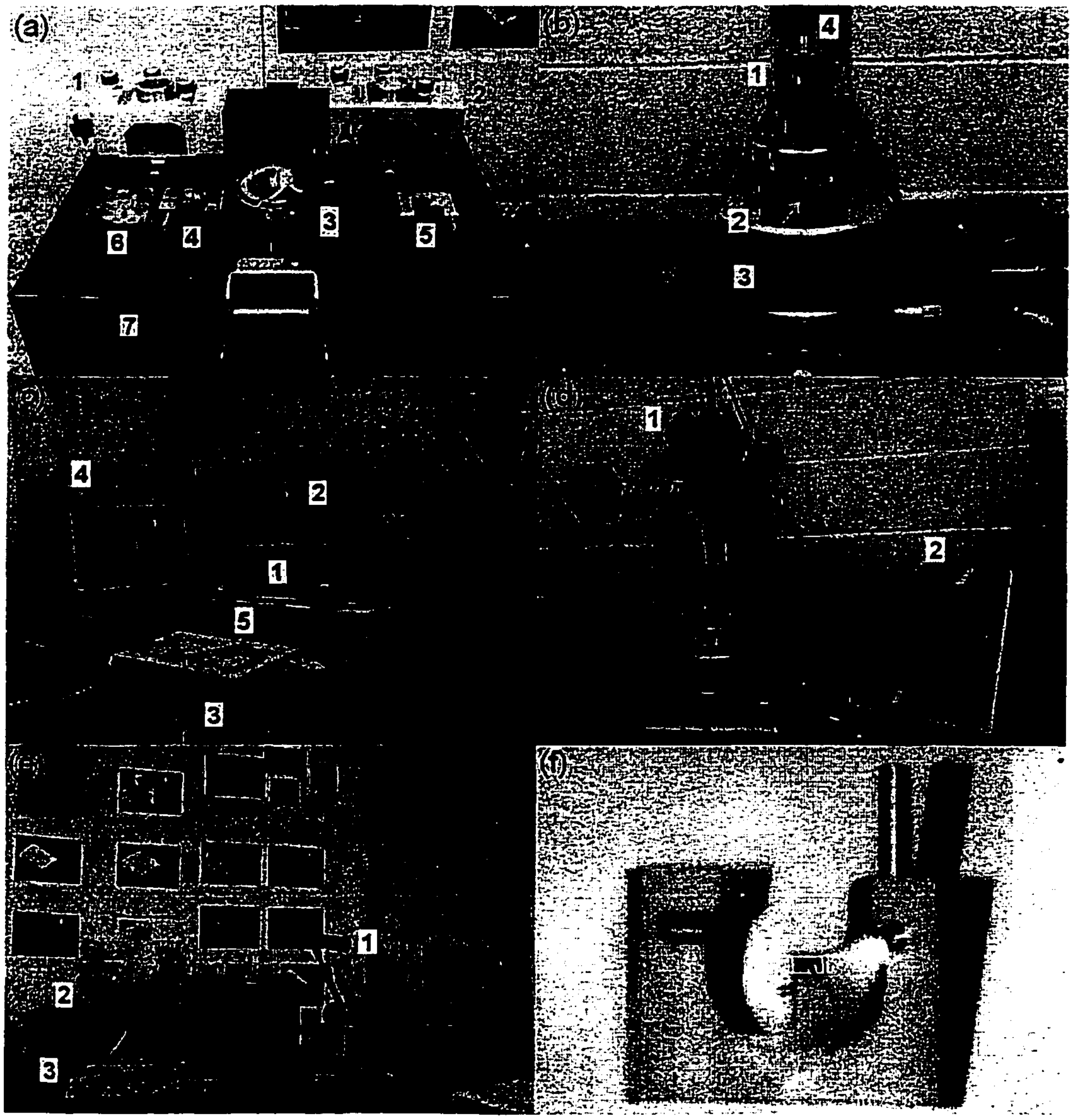

Figure 1.1: (a) 1–3: CMAFM, TMAFM, and STM heads; a4–5: tip mounts; a7: storage box. (b) 1: SPM neck (piezotube); 2: SPM body; white arrow: the rear screw (connected to stepper motor); 3: two LED panels. (c) 1: SPM controller; 2: control monitor; 3: computer (barely seen); 4: display monitor; 5: thermal printer. (d) 1: Binocular microscope; 2: tip monitor. (e) 1: Monocular microscope; 2: humiid/noise isolation box; 3: vibration isolation table. (f) All: tip mount; white rectangle: SPM tip; small bar: tip clip.

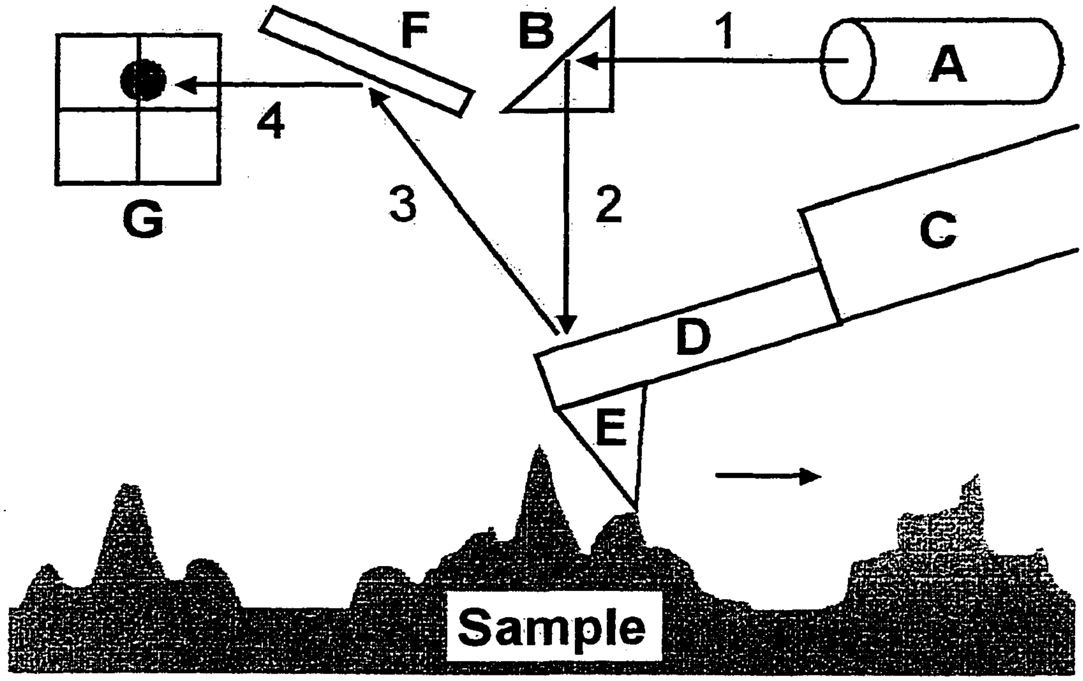

Figure 1.2: AFM head components including A: laser diode (path 1); B: prism (path 2); C: tip substrate; D: tip cantilever (path 3); E: tip crystal; F: mirror (path 4); G: quadruple photo-detector with a focused laser spot.

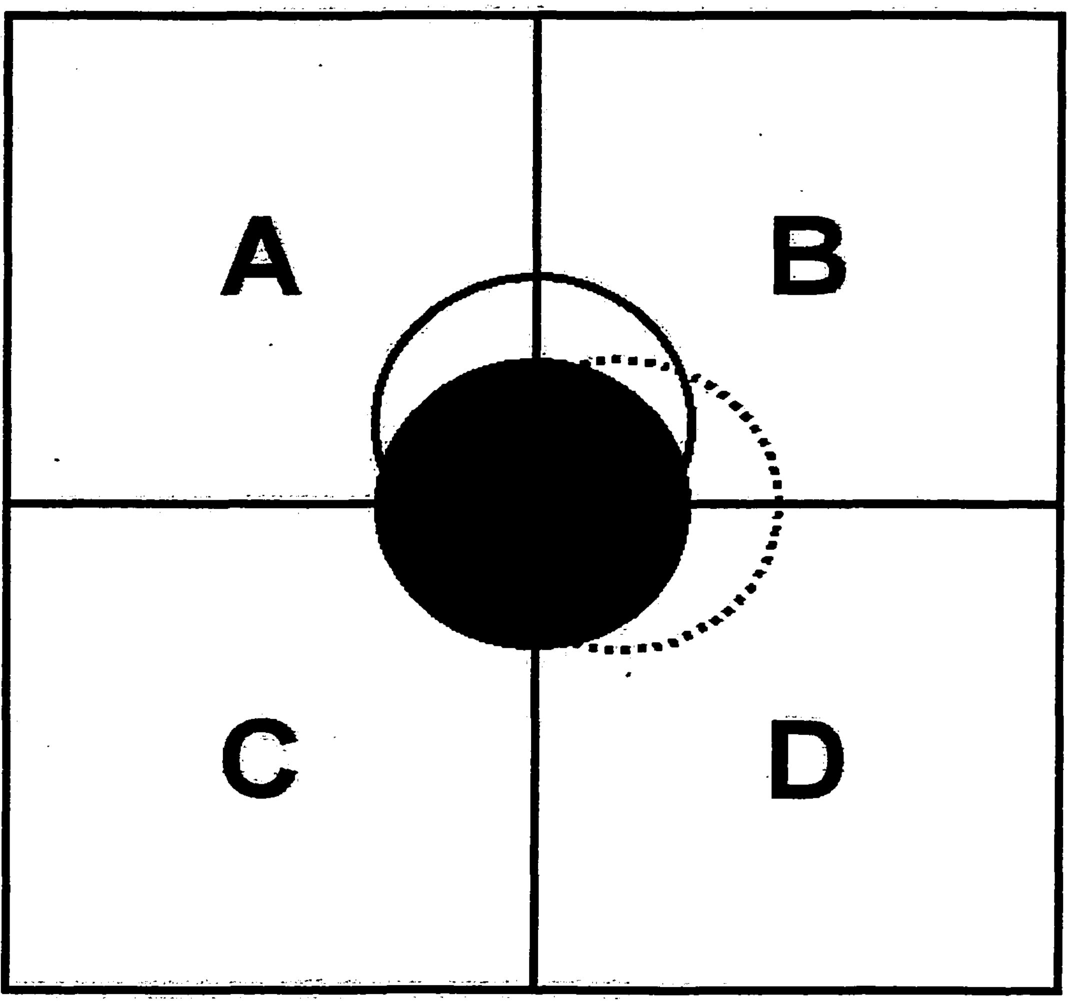

Figure 1.3: The photo-detector comprises four photo diodes. The laser beam is focused as a spot and moving around the diodes. The signal differences between diodes change with the local motion of the scanning tip or the piezotube and map out the surface morphology.

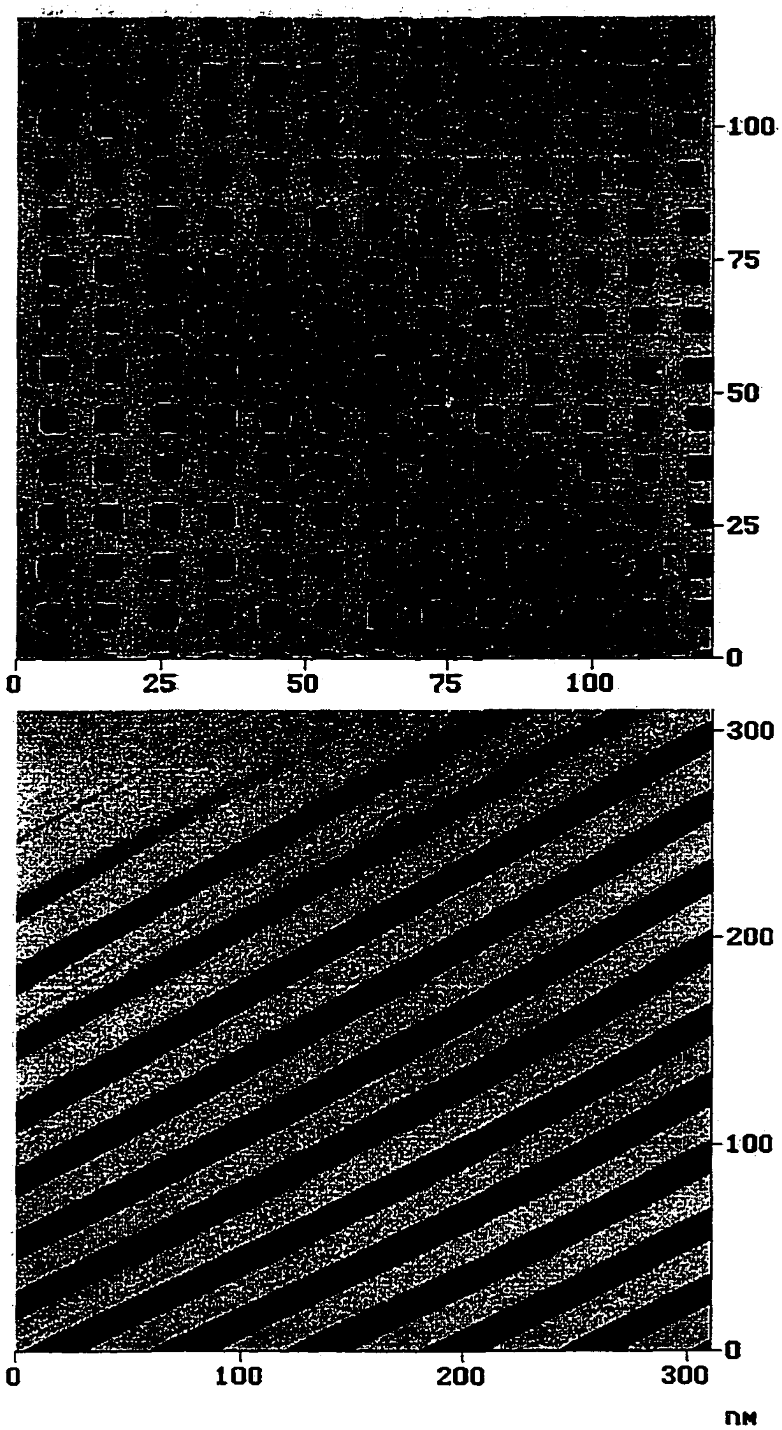

Figure 1.4: Top: a calibration grid for large size SPM J scanner (piezotube). The scan size is 125 × 125 μm^2. Bottom: an image captured automatically during the calibration process.

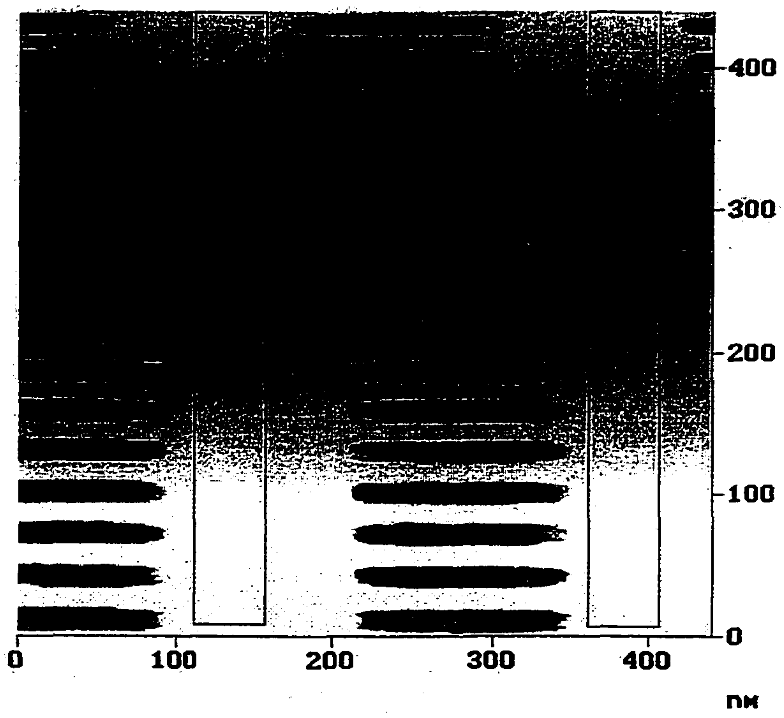

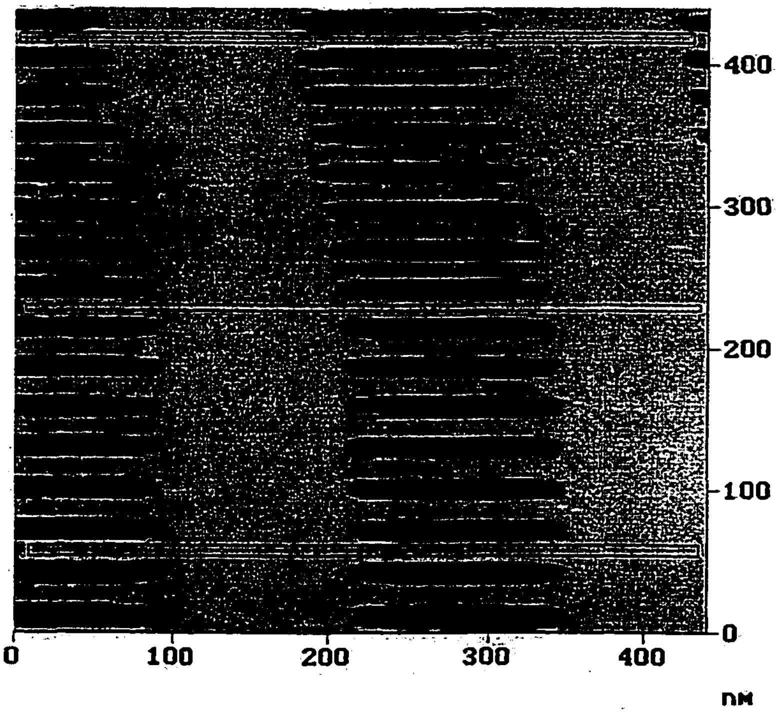

Figure 1.5: Top: an image of the standard grid captured during the calibration process. A horizontal bow in the image is observed. Vertical boxes are drawn to select the regions of reference for a second order plane fit in the y direction. Bottom: The grid with the bow removed and narrow horizontal boxes are selected for a first order plane fit in the x direction. Note the plane fit is not needed in calibration.

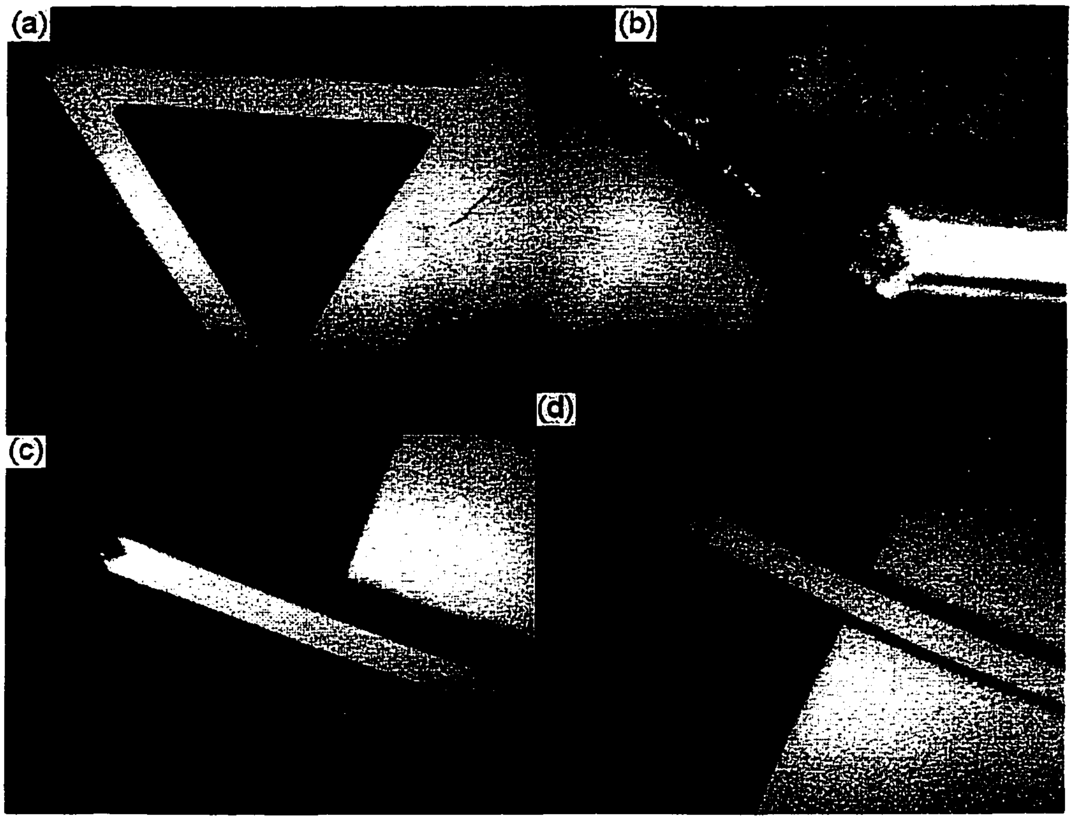

Figure 1.6: (a) Standard silicon nitride probe used in CMAFM. (b) Mechanically cut Pt/Ir STM tip. Note the tip apex is not overall but locally sharp. (c) Standard silicon probe used in TMAFM. (d) Etched silicon probe (sharper) used in TMAFM. Note the size and position of tip crystal are all different for different probes.

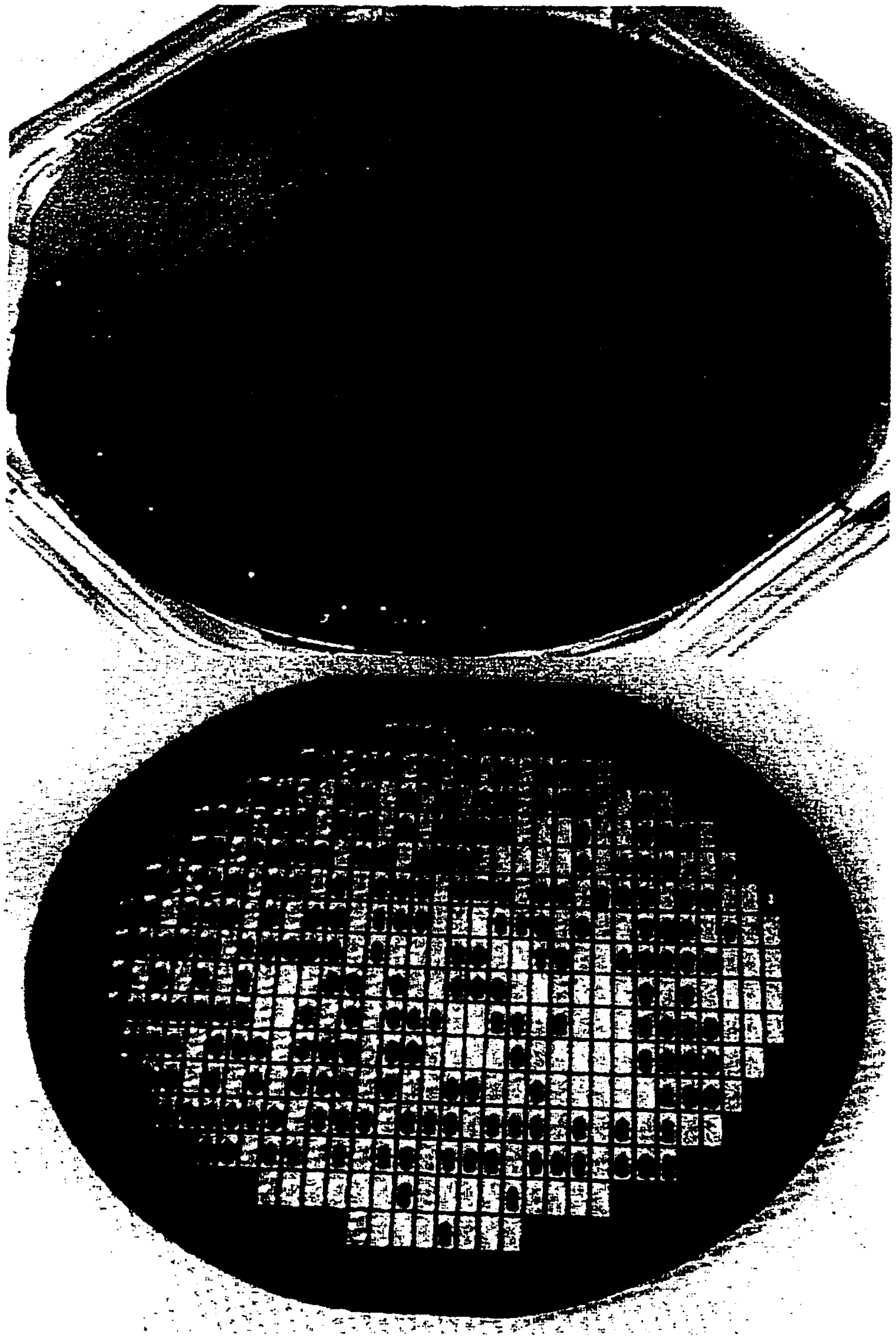

Figure 1.7: Top: CMAFM tip wafer. The tips are normally detached from the wafer in strips and broken apart later for use. Bottom: TMAFM tip wafer. An empty lot means a tip has been taken away.

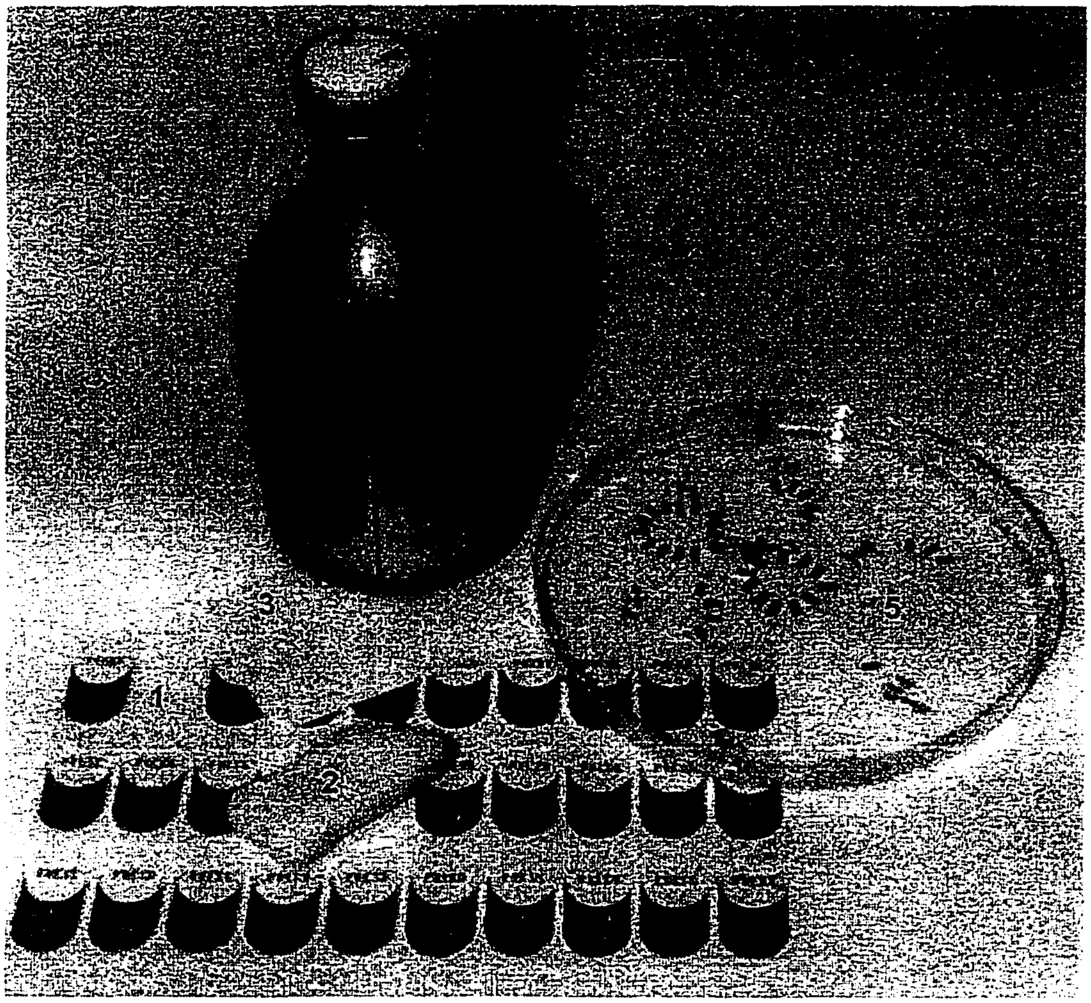

Figure 1.8: 1: Double sided glue sticker; 2: polymer clay; 3: removable sticker; 4: conducting silver glue/paste (also used in scanning electron microscopy, SEM); 5: used tips stored in a plastic dish attached to the glue from item 1.

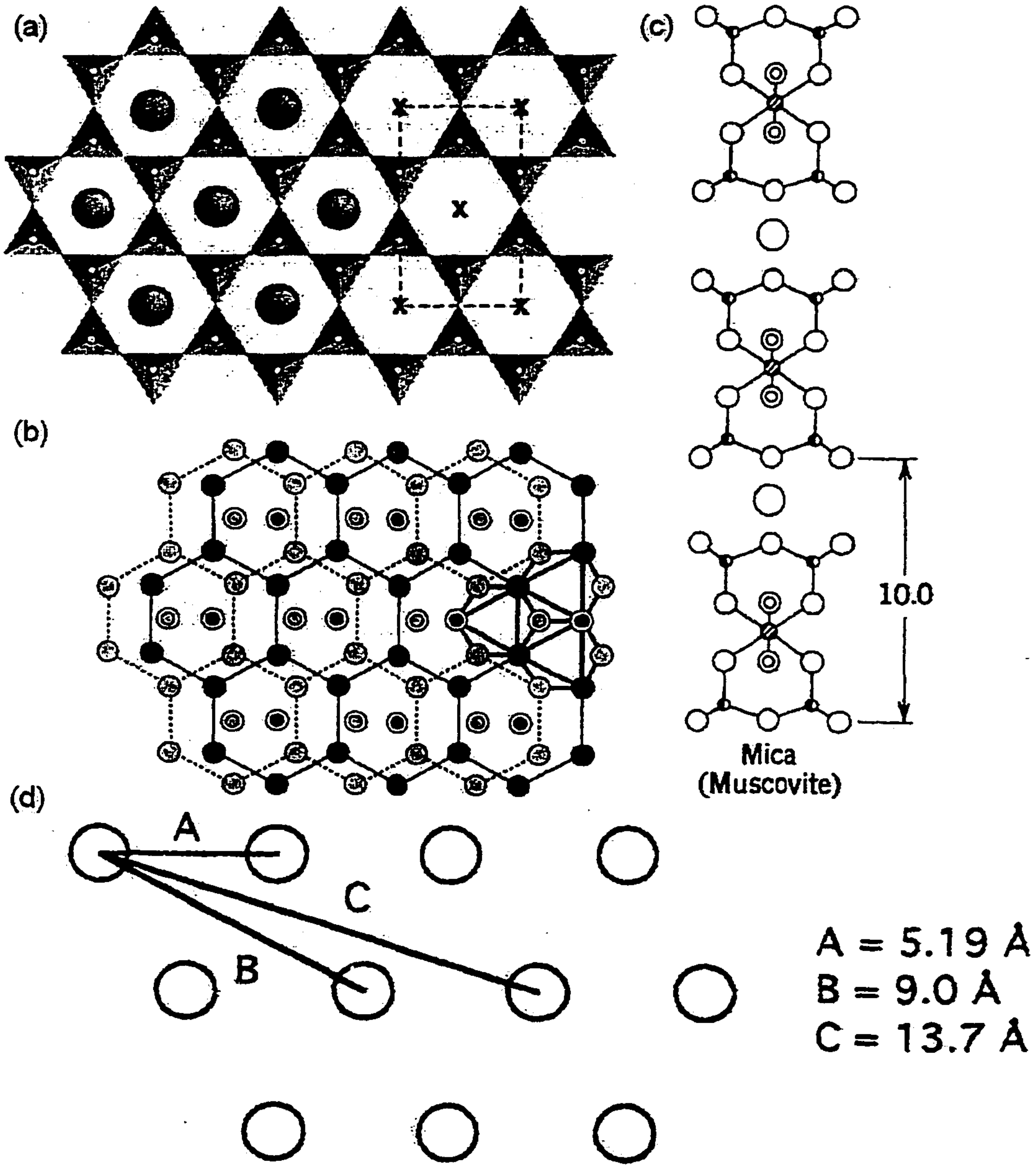

Figure 1.9: (a) Tetrahedral (silica) sheet of mica [16]. The tetrahedra form hexagonal rings centered with OH groups (spheres) from the octahedral sheet. (b) Octahedral (alumina) sheet of mica [16]. Dark circles are higher than the light circles. Six oxygens (circles) form a octahedron with an aluminum atom enclosed (not shown). (c) Side view of three mica layers [17]. Each layer has three sheets (two tetrahedral and one octahedral) and is separated from other layers by potassium ions (large empty circle). Oxygen: small empty circle; silicon: half-filled circle; aluminum: dashed circle; hydroxyl group: double circle. The spacing unit is Å. (d) Lattice parameters of six-fold pattern of mica imaged using SPM [1].

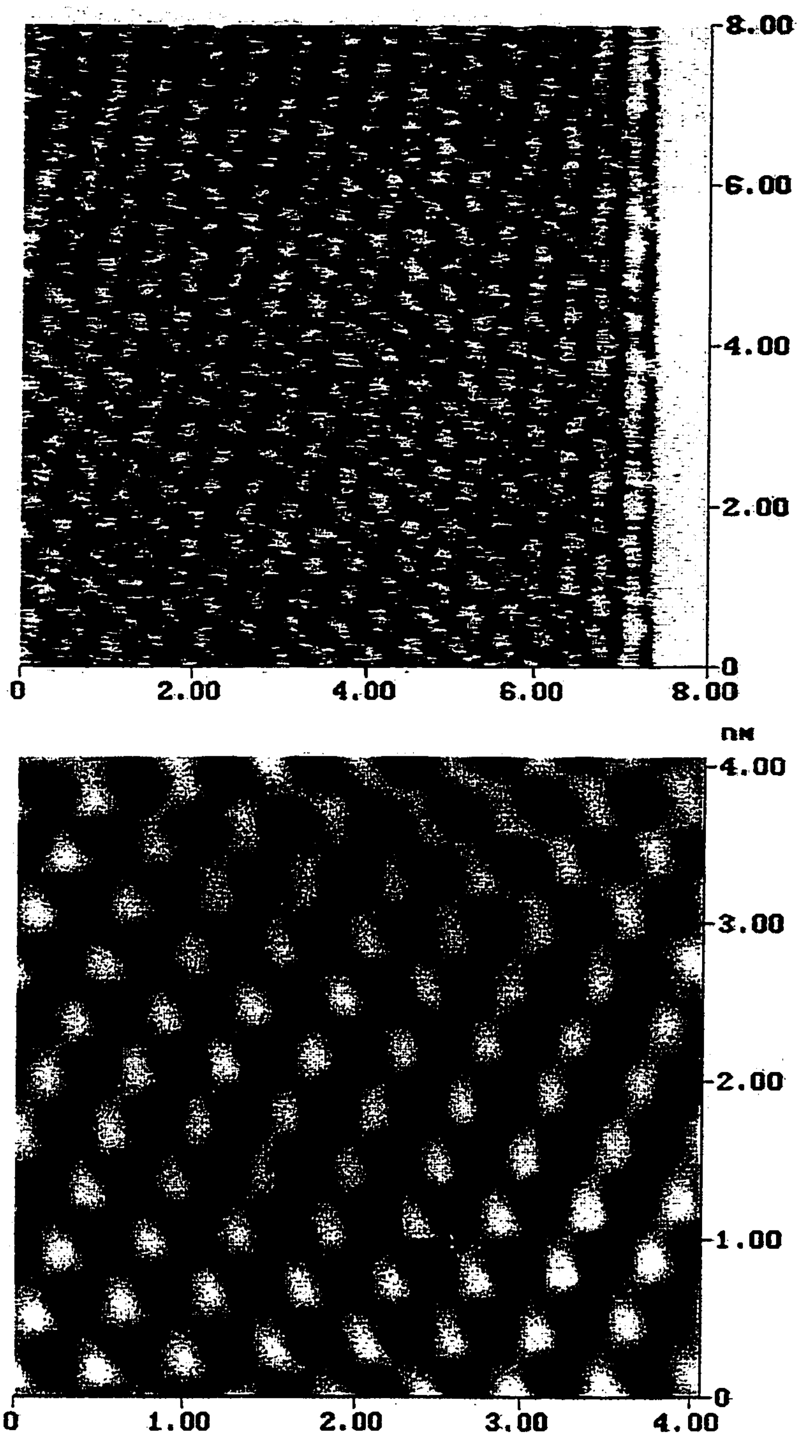

Figure 1.10: Top: AFM image of mica. The scan size is 8 × 8 μm^2. The lattice spacings match those in Fig. 1.9:d. Bottom: filtered AFM image of mica. Six-fold pattern is evident. Each bright spot represents two silica tetrahedra.

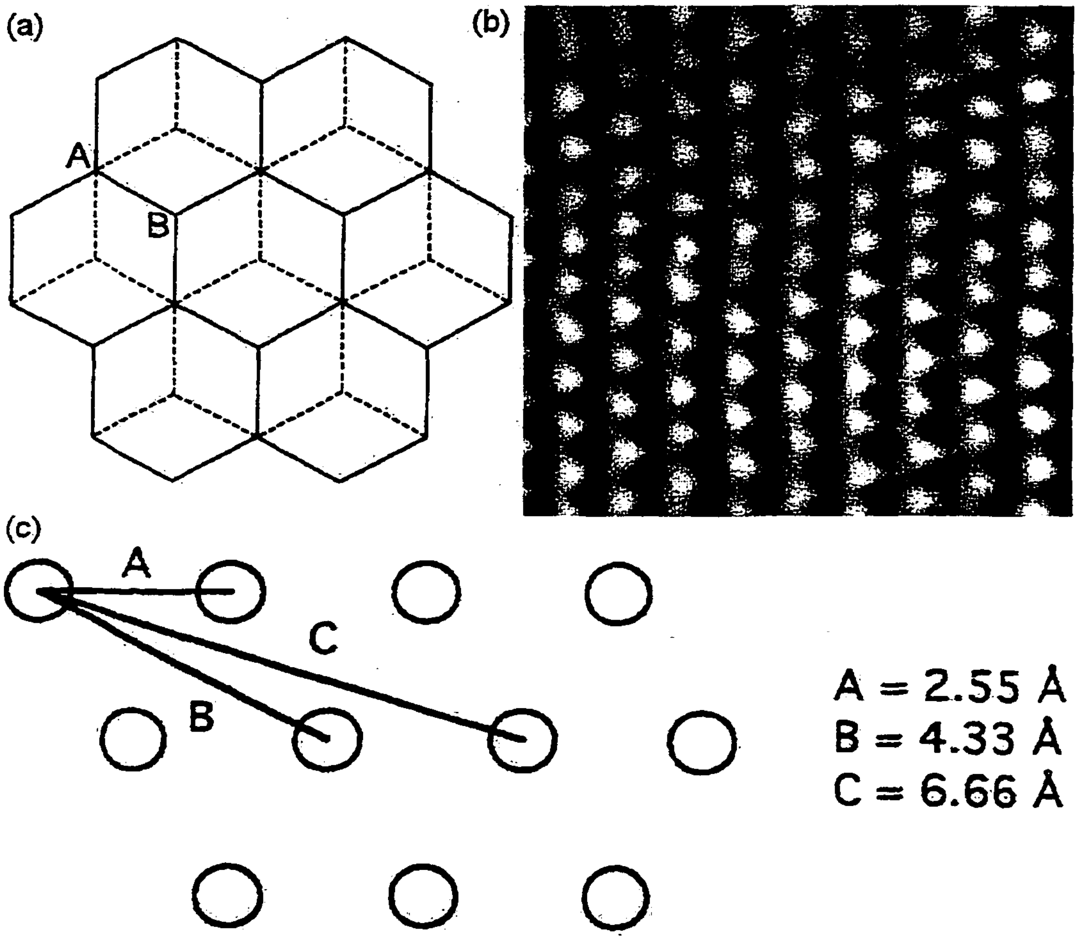

Figure 1.11: (a) Honey-comb or three-fold pattern of graphite. The carbon at site A has a neighboring carbon beneath while that at site B has none. (b) Six-fold pattern of graphite surface imaged using AFM (filtered). Each bright spot represents two carbons or the A site carbon. (c) Lattice parameters of graphite six-fold pattern.

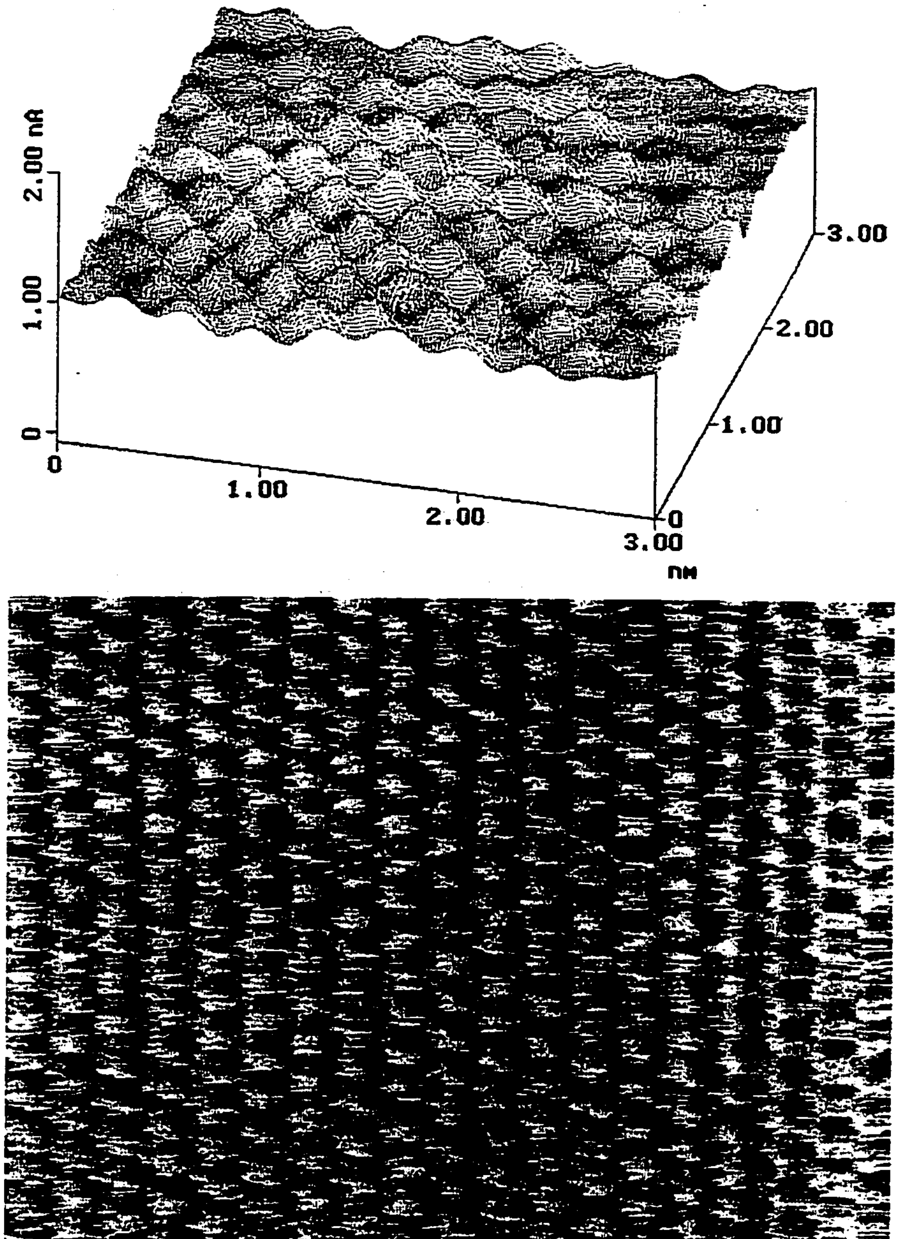

Figure 1.12: Top: STM image of graphite shown is a perspective view. The scan size is 3 × 3 nm^2. Six-fold pattern is observed. Bottom: AFM image of graphite. The scan size is 4 × 4 nm^2. Both STM and AFM images show six-fold patterns.

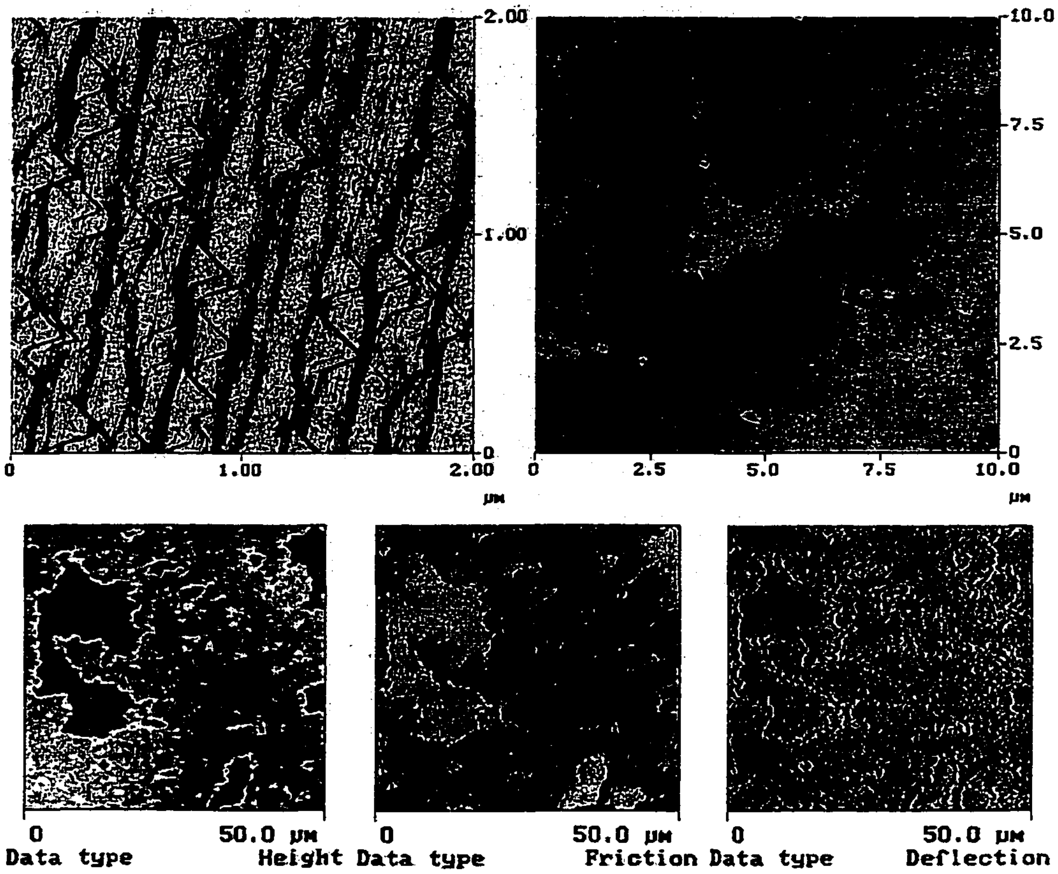

Figure 1.13: Top left: CaF_2 film on Si(111). Top right: In situ annealed CaF_2 film on Si(100) Bottom row: constant force, frictional force, and varying force images of a two-layer semiconductor film. Samples courtesy of the MBE laboratory of the University of Oklahoma.

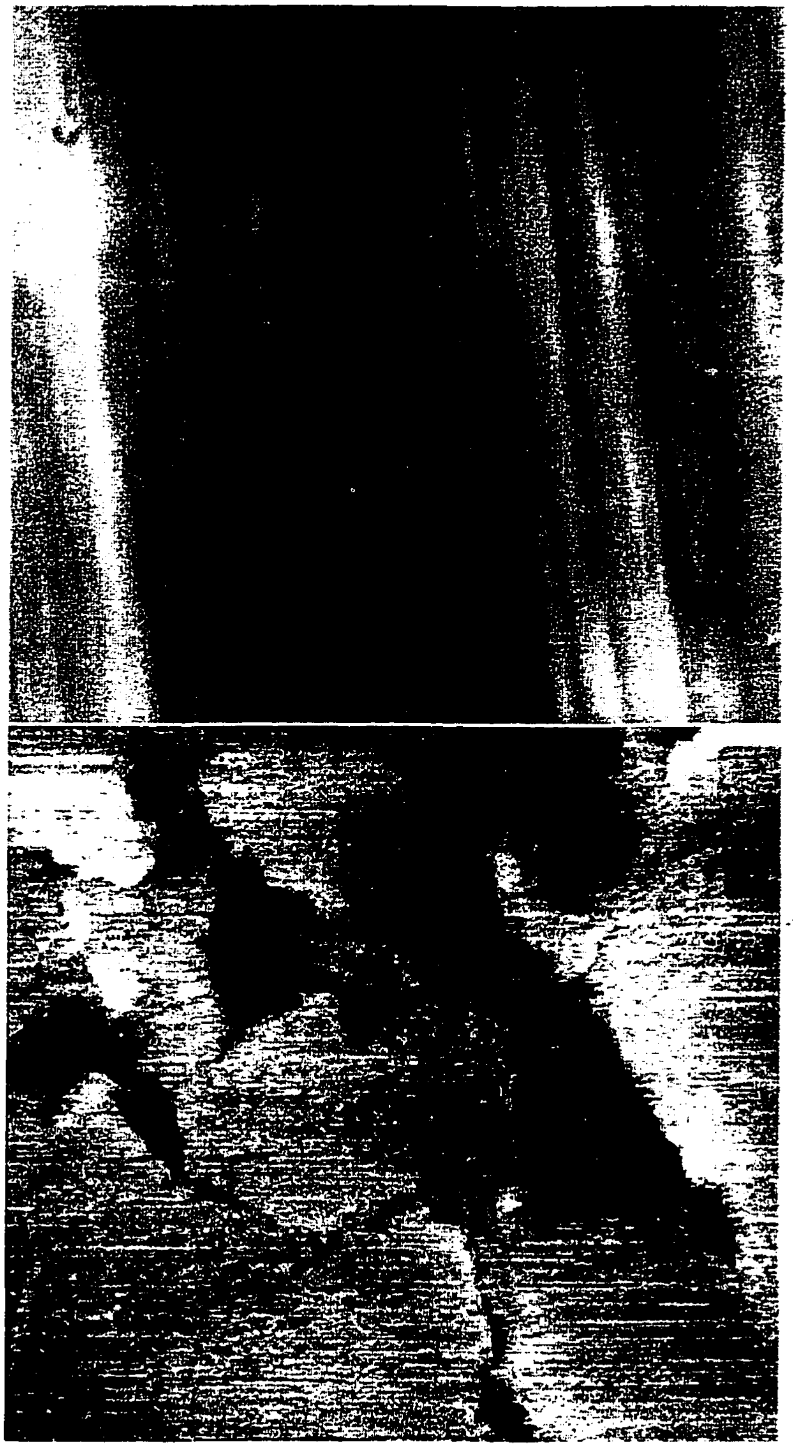

Figure 1.14: Top: CMAFM image of nickel foil. Grooves and ridges due to the manufacturing process are observed. The scan size is 10 × 10 μm^2. Bottom: STM image of a compact layer of nickel flakes. The scan size is 1.7 × 1.7 μm^2. Metallic films can be images using both AFM and STM.

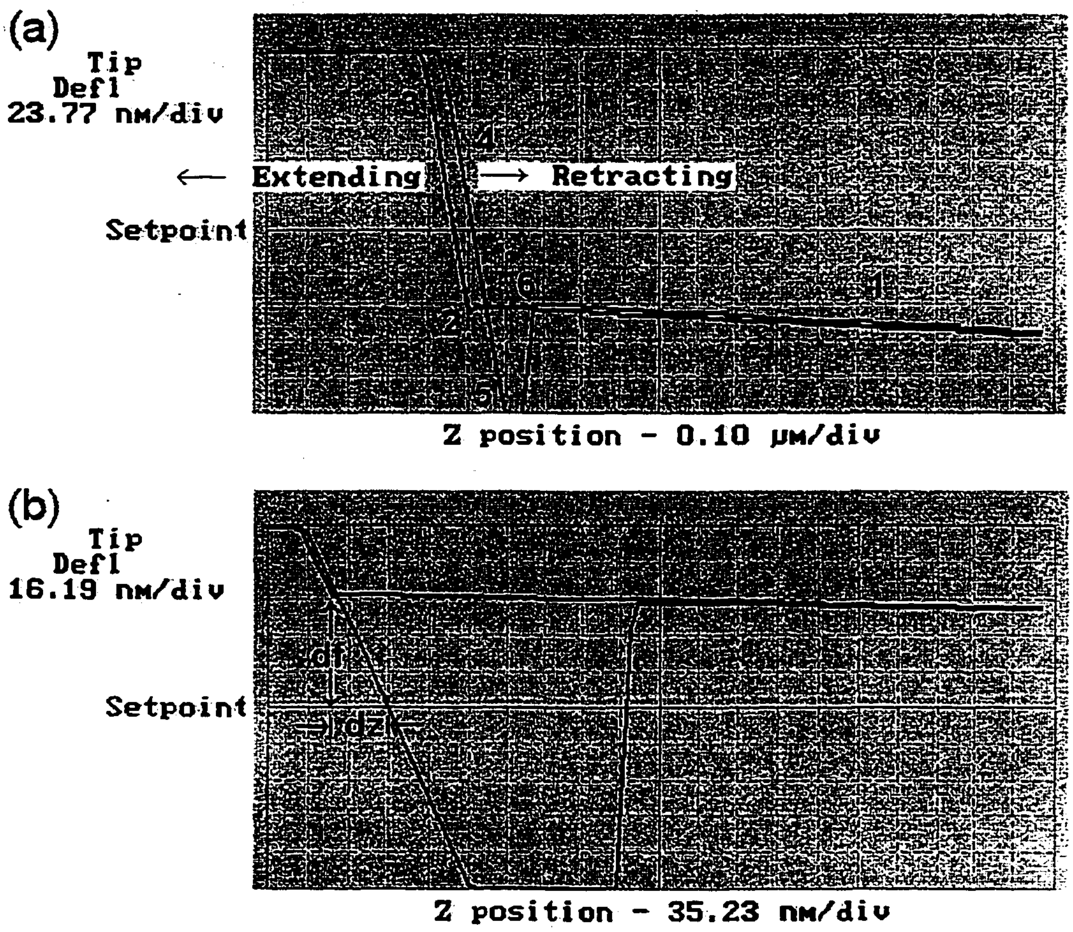

Figure 1.15: Tip-sample forces plotted against the sample movement, approaching and withdrawing from the tip.

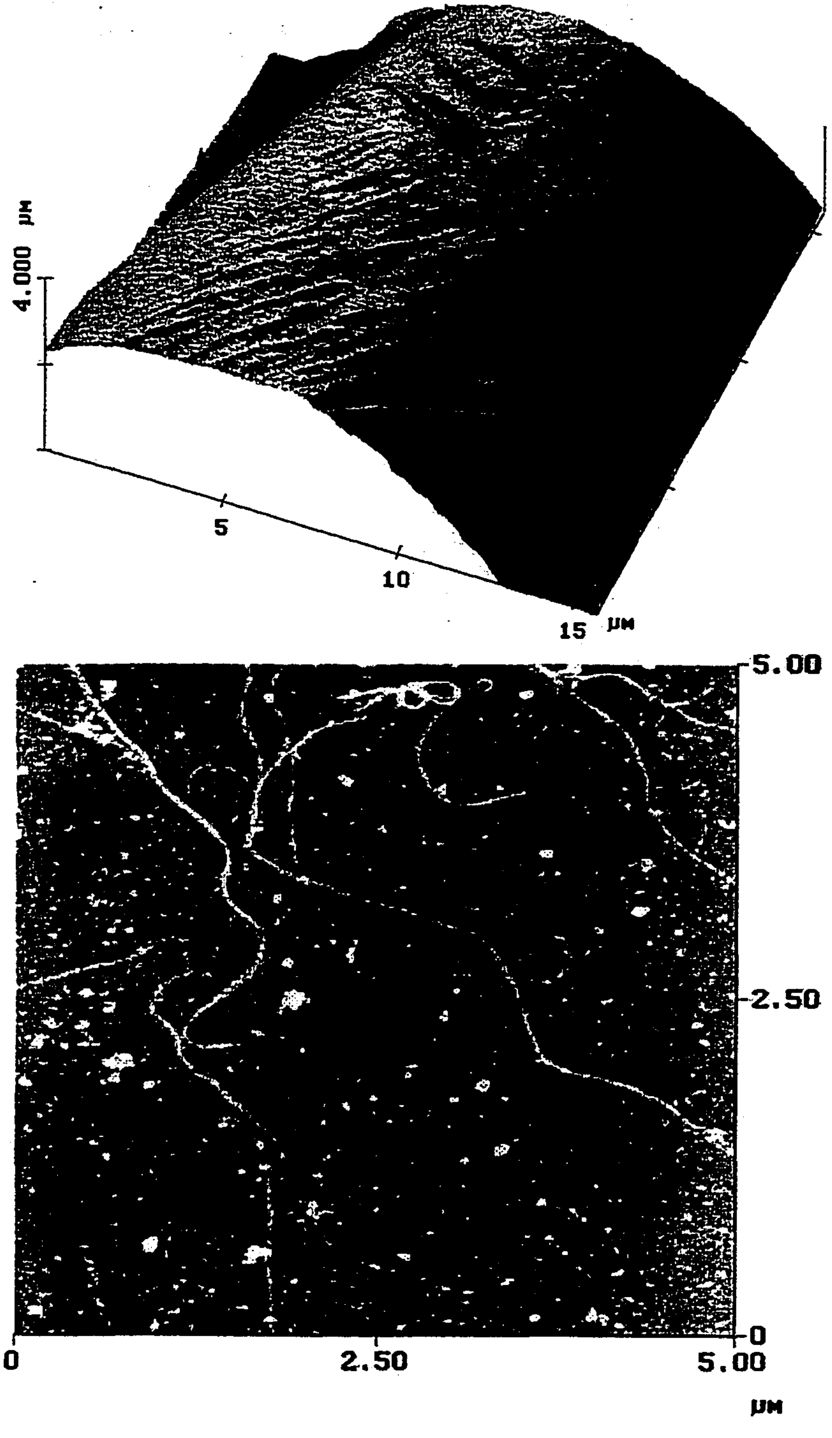

Figure 1.16: Top: AFM image of a cotton fiber. The lower right portion of the image is blank because the height range has exceeded the vertical capacity of the piezotube. Bottom: AFM image of a commercial nanotube spread on silicon wafer. Since the nanotube in the image will be dilated laterally due to tip artifact, the diameter of the nanotube can be found by measuring its height instead.

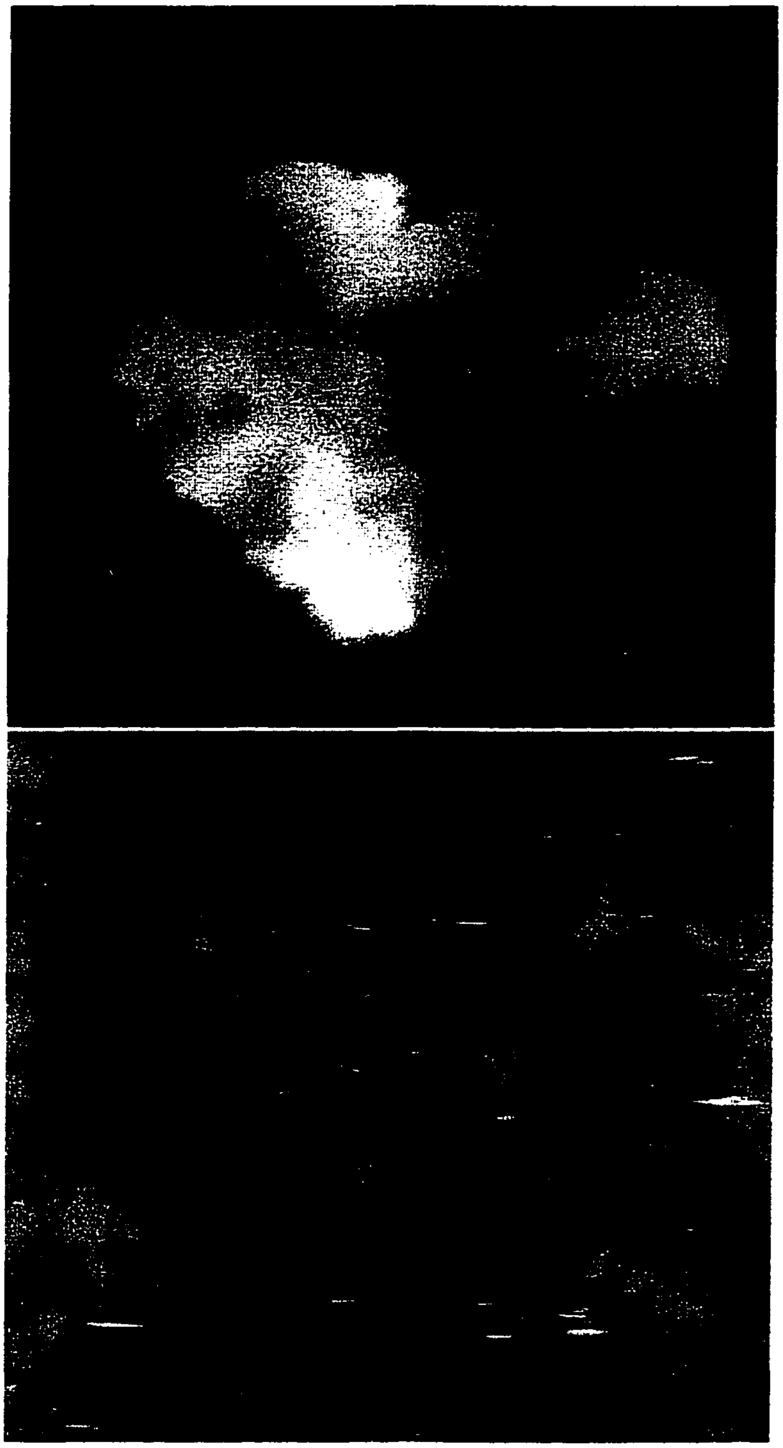

Figure 1.17: Top: AFM image of a single nickel flake fixed on a wax film. The surface morphology of the wax film is also clearly resolved. The scan size is 50 × 50 μm^2. Bottom: a layer of densely spread silica powder. The surface of the particles was found flattened due to compression. Slight compression and loose spreading are needed not to damage the powder.

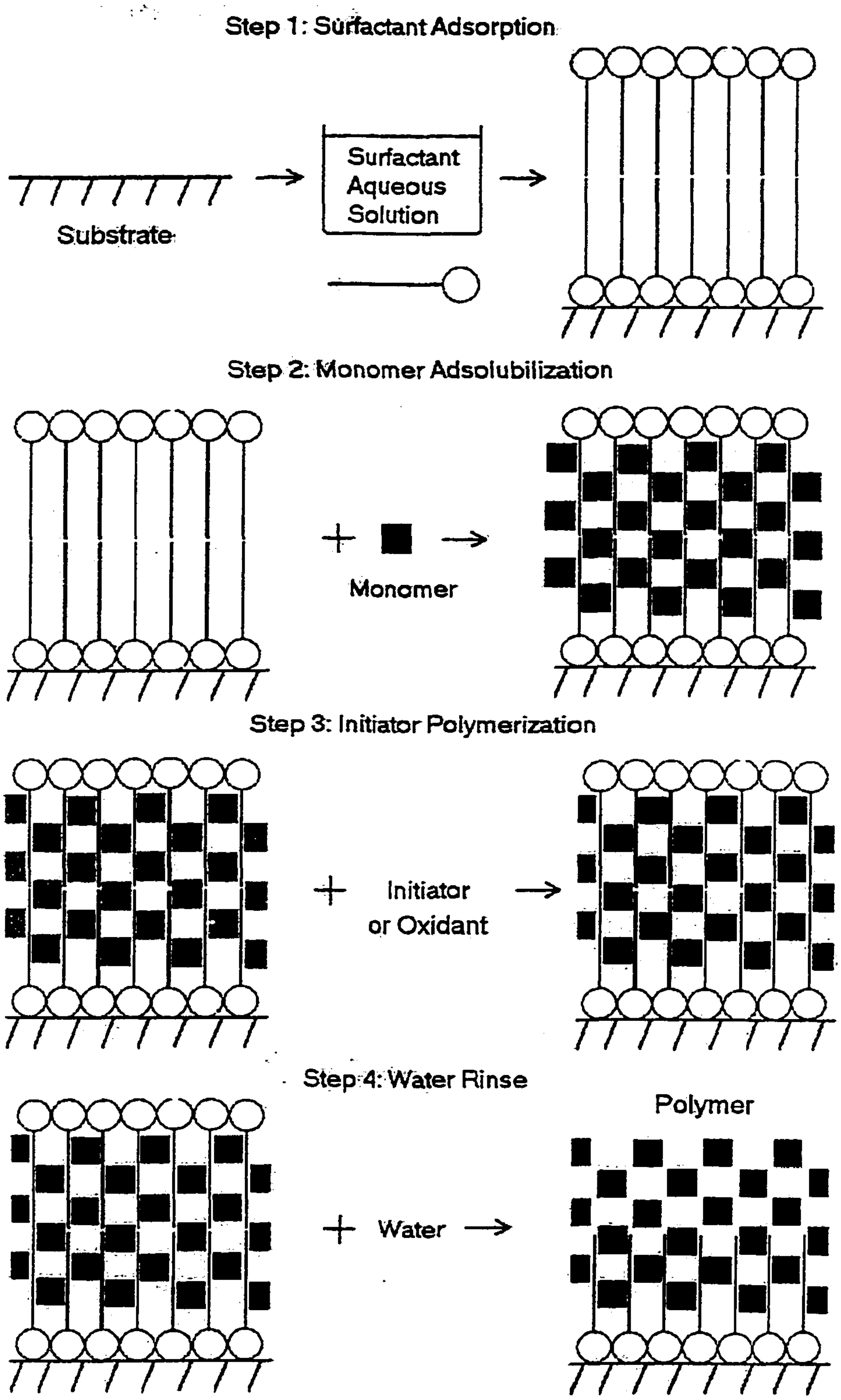

Figure 1.18: Procedures of admicellar polymerization using one-solution approach.

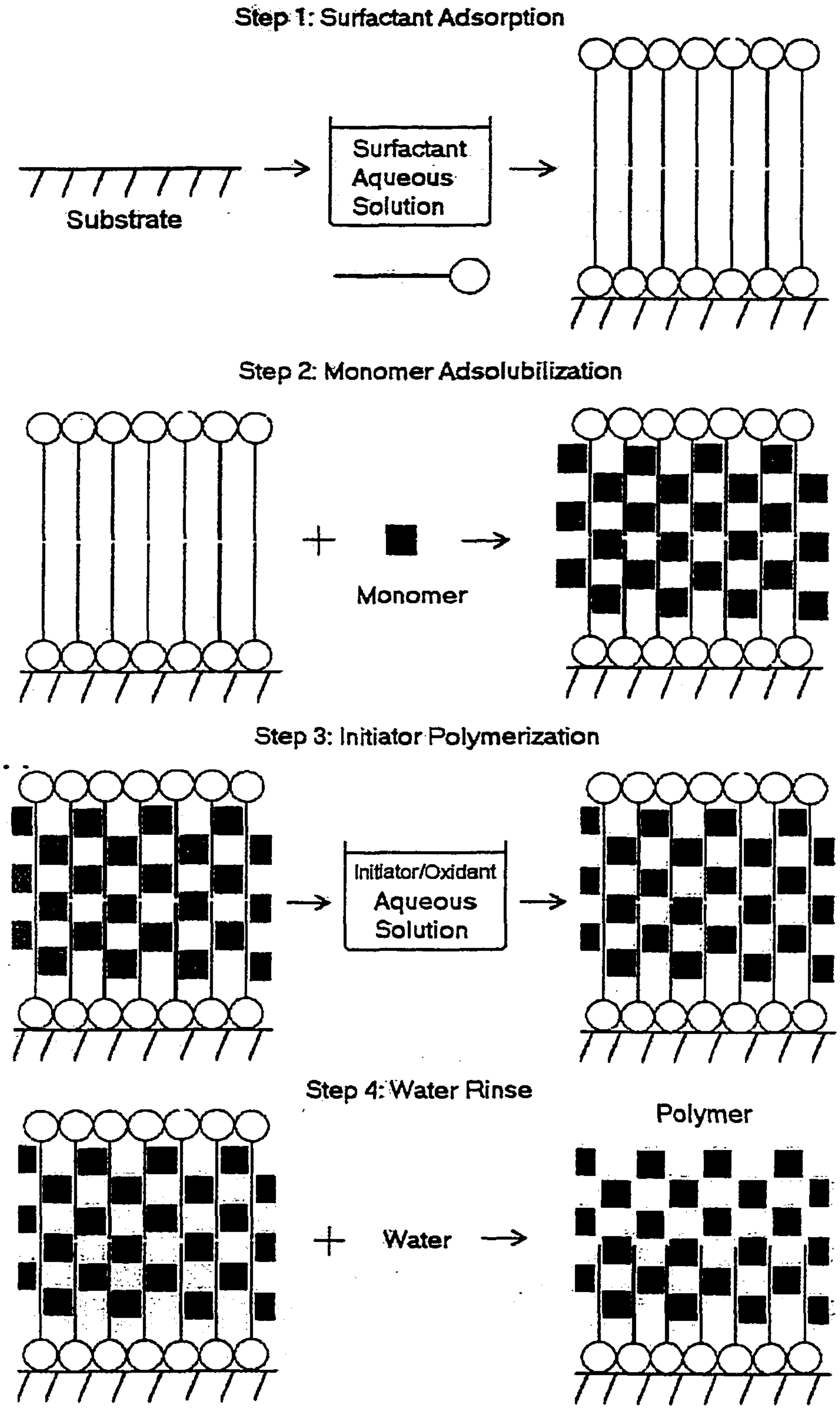

Figure 1.19: Procedures of admicellar polymerization using two-solution approach.

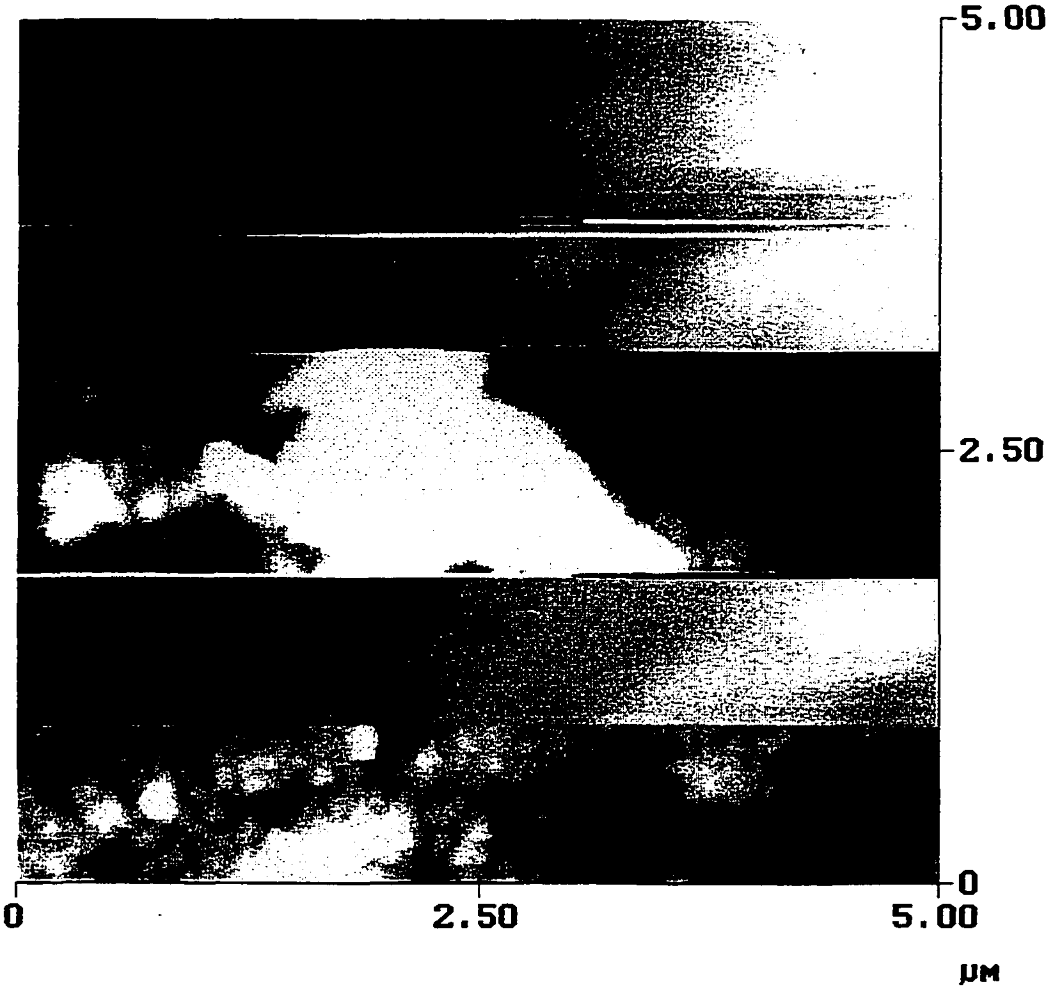

Figure 1.20: False engagement of SPM probes in TMAFM. In the top portion only a minimal force is sensed by the tip. At this stage the tip may not touch the surface physically. As the tip is brought closer to the surface, stronger attractive force is sensed and finally a clear image is shown. The noisy lines are due to manual decrease of the setpoint, corresponding to a increase in tip-sample force. As the setpoint is increased again, the sample moves down away from the tip and the image loses resolution. Note in CMAFM, the force is increased by increasing the setpoint.

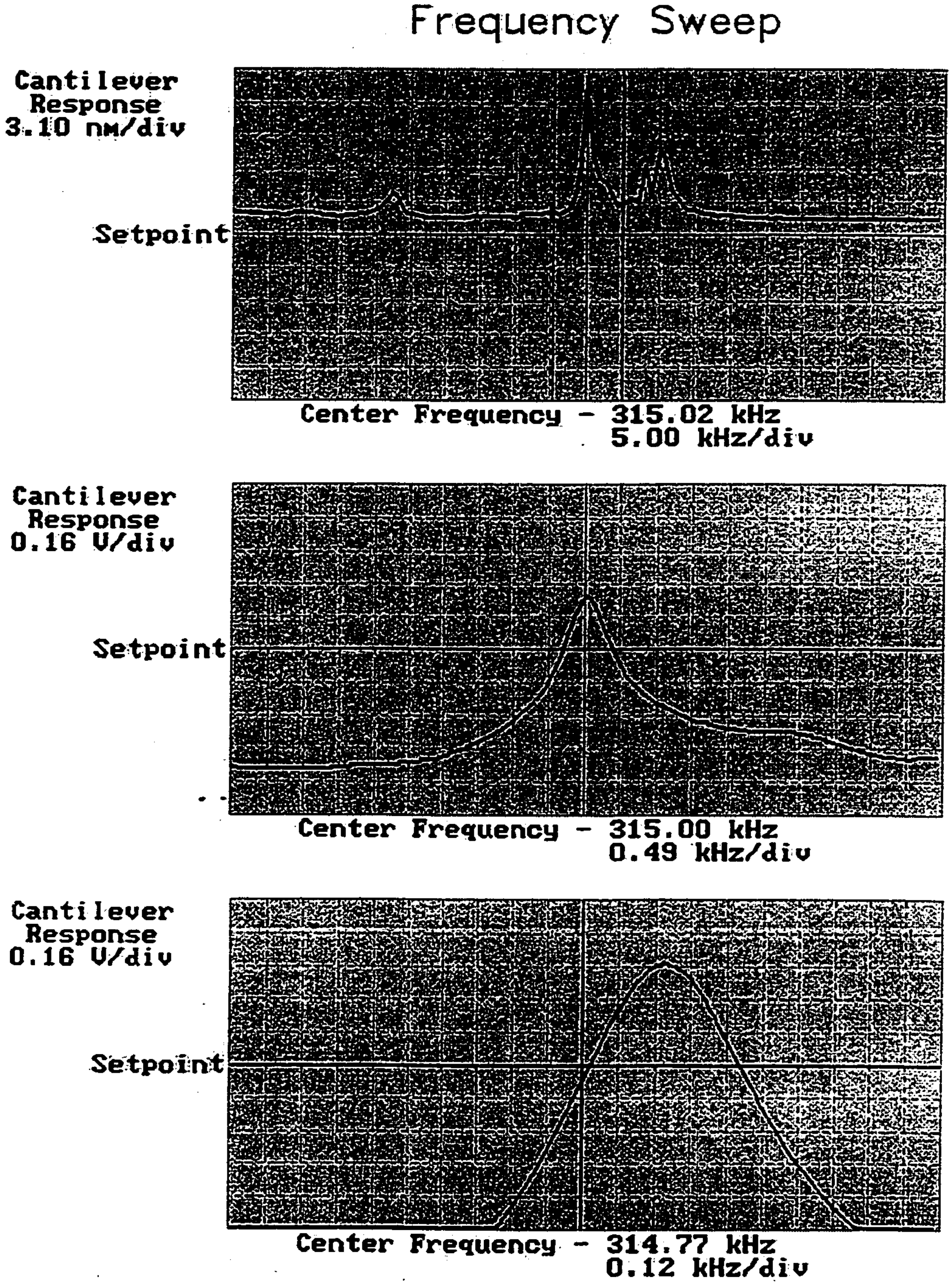

Figure 1.21: Consecutively magnified images of tuned frequency and amplitude responses of the tip cantilever for TMAFM. Top: several amplitude peaks appear at different frequencies. The maximum peak is selected and corresponds to the resonant frequency of the cantilever. Middle: enlarged resonant peak. Bottom: the top portion of the resonant peak. Good results are obtained with the center frequency set slightly lower than the peak frequency [1].

Figure 1.22: Double image: artifact due to a split tip. Doubly or multiply duplicated features are observed in an horizontal orientation.

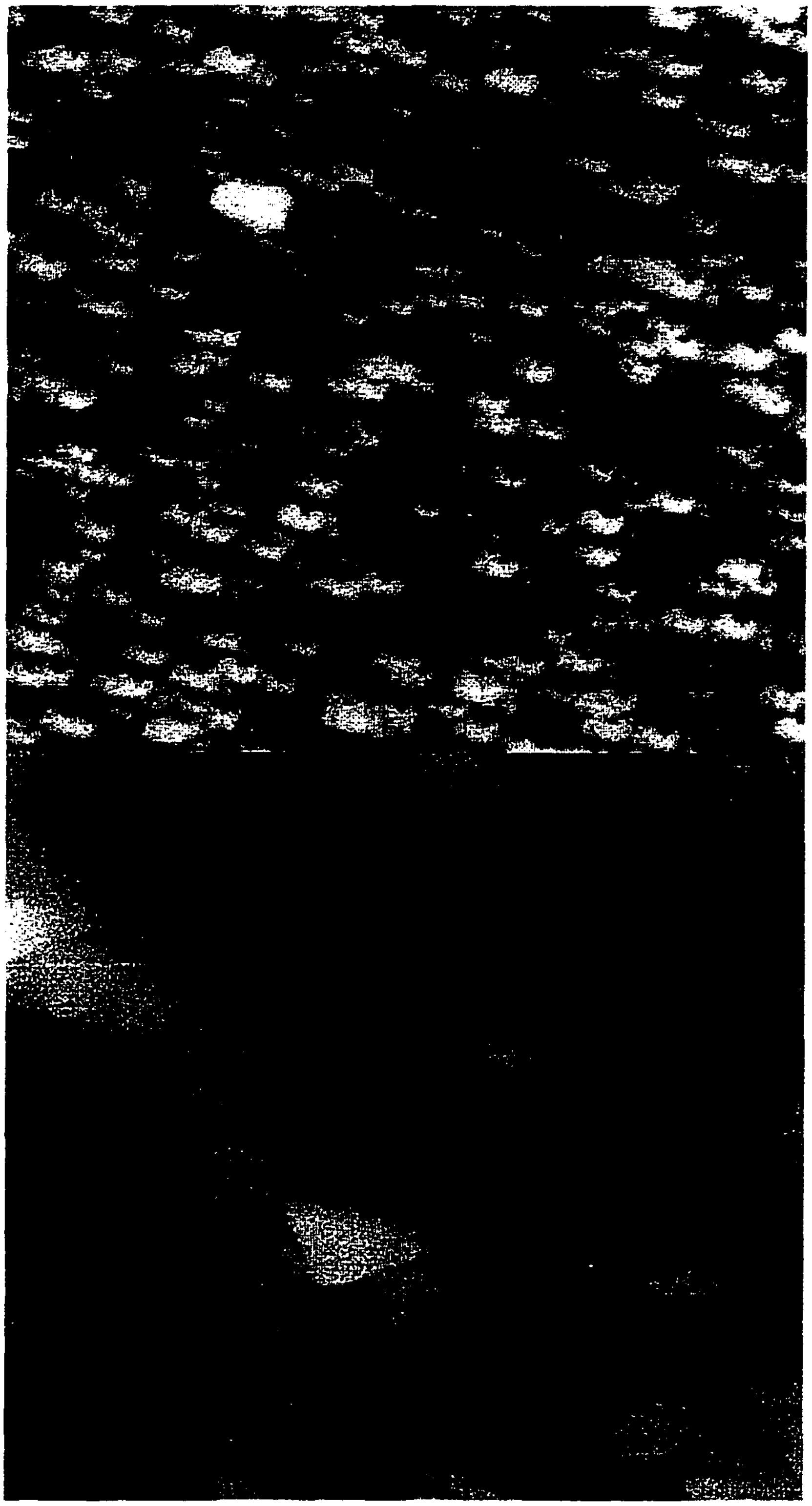

Figure 1.23: Top: repeatedly imaged tip that was contaminated by polymeric material. Bottom: repeatedly imaged tip that was broken. The fracture surface of the tip is a triangle.

Chapter 2

Polypyrrole Thin Films*

Chemical deposition of electrically conducting polypyrrole (PPy) thin films on mica and alumina was carried out in aqueous solutions with and without surfactant. Examination of film morphology and thickness by atomic force microscopy (AFM) indicated a strong dependence of structure on method of preparation. Films made in the absence of surfactant were thicker than 150 nm with wrinkles present, indicating the overcoming of film-substrate adhesion by internal film cohesion. Oxidative polymerization with surfactant allowed reproducible synthesis of very thin films (50 nm thickness) with improved adhesion and suppressed formation of wrinkles. Experimental results are discussed within the context of a Stranski-Krastanov model of film growth. Film thicknesses and surface fractal dimensions were derived from AFM. Fractal analysis of PPy films on alumina helped discern their presence on the microscopically rough substrate and quantitatively expressed the changes in sample color by surface roughness.

Keywords: Polypyrrole; Conducting polymer; Atomic force microscopy

2.1 Introduction

In recent years, polypyrrole (PPy) and other electrically conducting organic thin films have been widely studied for their potential application in corrosion pro-

---

*W.-L. Yuan, E.A. O'Rear, G. Cho, G.P. Funkhouser, D.T. Glatzhofer, Thin Polypyrrole Films Formed on Mica and Alumina with and without Surfactant Present: Characterization by Scanning Probe and Optical Microscopy, Thin Solid Films, 385:1-2 (2001) 96-108 tection, biosensors, battery electrodes, solid state devices, and even patterned circuits. Many techniques for making thin films of conducting polymers have been proposed. However, improvements in film quality such as reduced thickness, fewer defects, and better mechanical behavior and electrical conductivity are still in demand.

Currently, available methods for making polymer thin films from monomer include electrochemical synthesis (in the case of semiconducting polymers) [1–8], chemical oxidative polymerization [9–12], admicellar polymerization [13–17], and layer-by-layer deposition [18, 19]. Morphological and electrochemical investigations of PPy films *in situ* or *ex situ* by atomic force microscopy (AFM) and scanning tunneling microscopy (STM) have also been reported recently [20–30]. Generally, most of these films have a thickness greater than 1.0 μm and a conductivity ranging from 10^{-2} up to 10^{2} S/cm [12, 31–33]. The electrochemical method can produce very good thick films on conducting substrates in a short time while chemical oxidation holds more promise for building good ultrathin films. For the former, the principles of surfactant chemistry have been used to localize pyrrole near the electrode surface and thus facilitate polymerization. Two approaches in the use of surfactants for electropolymerization utilized incorporation of the pyrrole moiety into anionic and cationic surfactant molecules [1, 4, 8] or surface solubilization of hydrophobic alkylated pyrroles [3]. Earlier studies have shown that surfactant can influence film morphology in electropolymerization.

Chemical polymerization, in contrast, has several advantages over traditional electrochemical deposition. It works on both conducting and insulating substrates, including powders. Chemical polymerization in the aqueous phase is simple and more environmentally benign. Properties of films deposited by this approach can be controlled by parameters such as pH, electrolyte, and substrate.

Recently, admicellar polymerization was employed to deposit a PPy thin film on insulating materials, alumina powder and plates, by using amphiphiles (sodium dodecyl sulfate, SDS, or hexanoic acid, HA) to form a 2D medium for the monomer to adsolubilize at the solid-liquid interface [34, 35]. The highly concentrated pyrrole monomer, due to interaction between pyrrole and the bilayer, led to lateral growth of PPy. Alumina particles coated with PPy (13 wt%) in the presence of HA were reported to give higher contact conductivity (4.7×10^{-2} S/cm) than that of pure PPy powder (1.5×10^{-2} S/cm) [35]. This result demonstrated the utility of this technique for building highly conducting PPy ultrathin films with good morphological qualities. PPy thin films deposited on alumina plates with and without surfactant present under different conditions showed visible color differences between the treated substrates, varying from white to gray to black. In order to compare the surface structures of the coated and bare alumina plates on the microscopic scale, scanning probe microscopy (SPM) was used in the present study.

To examine the conductivity and thickness of PPy films further, we chose mica discs as the substrate and performed admicellar polymerization to apply PPy films. Mica discs have several advantages over alumina powder and plates such as atomic smoothness of the surface, low cost, low conductivity, easy cleaning procedures, and a negatively charged framework. Related work on mica showed that use of HA templates yielded PPy film thicknesses greater than 150 nm [36]. Wrinkles and good thin film conductivities were observed.

In this paper we present the characterization of PPy films chemically deposited on alumina plates and mica discs by AFM, STM, and optical microscopy. Atomic force microscopy (AFM) played a uniquely useful role in determining the PPy film thicknesses and measuring the surface fractal and roughness properties. The film thicknesses obtained using AFM were used to calculate the conductivities of PPy thin films on mica using the four-probe method [36]. In addition, we examined the conditions under which wrinkling of the PPy films occurred, the mechanism of which is the subject of debate.

2.2 Principles and Experiments

2.2.1 Theoretical Background

In this study we focus on the use of admicellar polymerization (AP) to produce thin PPy films on mica discs and alumina plates. AP has been used in our group for more than 10 years. The process incorporates several steps and takes place in an aqueous solution. The first step is to form a bilayer on the substrate by adsorption of surfactant. In the second step, the added monomer is adsolubilized into the "hydrophobic" or "oily" phase (the inner part) of the bilayer which leads to a region with highly concentrated monomer. By adding oxidant or free radical initiator in the third step, polymerization will proceed to give a thin polymer film. After rinsing and drying, the exposed polymer changes the hydrophilicity of the substrate. In this work we used both cationic and anionic surfactants to configure bilayers on alumina and mica.

2.2.2 Materials

Pyrrole (98%, Aldrich) was filtered through basic alumina (Sigma). Sodium dodecyl sulfate (SDS, 98%, Aldrich) was recrystallized from 95% ethanol; cetyltrimethyl ammonium bromide (CTAB, Aldrich) was used as received. Ammonium persulfate (APS, Mallinckrodt), iron trichloride hexahydrate (ITC, Fisher Scientific), and iron dichloride tetrahydrate (IDC) were used without further purification. Sodium chloride (NaCl, Baker) was used as received. Double deionized water was used in all systems. Mica discs (Muscovite, V-4 grade, 1.5 cm in diameter, Asheville-Schoonmaker Mica) were used after cleaving off the top layer using a razor blade. Alumina plates (Hitachi) were cleaned with acetone before use.

2.2.3 Sample Analysis by AFM and STM

AFM and STM were performed with a NanoScope III, Multimode Scanning Probe Microscope from Digital Instruments, operated in "height" mode under ambient conditions. Standard silicon nitride and Pt-Ir tips were used except when scanning wrinkles, in which case etched silicon probes (ESP) with average half-cone angle about 18° were used. All the tips were purchased from Digital Instruments. Surface cross-section analysis was used to determine the thickness across the step of the film edge. STM analysis in this work was aimed at demonstrating the electrical conductivity of the PPy films to compare their STM-derived morphologies with those obtained using AFM. Fractal and roughness analyses were carried out using commercial software supplied with the SPM and Mathematica programs written by the author after considering analyses in the literature [28,37–41]. The surface fractal dimensions (FD) were calculated for the alumina samples using the relationship [42,43]

$$Surface\ Area = Cell\ Size^{-(FD-2)}. \tag{2.1}$$

Cell size is the length used to divide the whole image into an array of cells. In each cell, the four corners define two triangles in 3D space by connecting one of the two pairs of diagonal corners. The surface area of the cell is then calculated as the sum of those two triangular areas. By iteratively using smaller and smaller cell size, we obtain higher and higher total surface area which approaches the true surface area. The power law relationship then yields the fractal dimension from a logarithmic plot of surface area vs. cell size. Repeated structures on the surface such as granules are revealed by the fractal dimension. Since PPy deposited on alumina plates shows granular structures, it is possible to use fractal-dimension analysis to characterize the surface morphology of the coatings.

We also calculated the excess surface area (R_s) of each image according to the definition expressed in Eq. 2.2

$$Excess\ Surface\ Area = \frac{Surface\ Area - Image\ Area}{Image\ Area} \times 100\% \qquad (2.2)$$

where the excess surface area represents the existence of 3D structures on the surface [44]. Higher excess surface area generally implies higher density of discrete tall or fine features on the surface.

2.2.4 Thin Film Deposition Procedures

In this work we prepared two groups of samples based on the substrates used; mica, which is atomically smooth, and alumina plate, which is comparatively rough. On alumina we deposited PPy thin films using SDS as the surfactant and APS as the oxidant, while we used SDS or CTAB as the surfactant and APS or ITC as the oxidant for PPy deposition on mica (Table 2.1). The change in oxidant with surfactant is necessary to maintain chemical compatibility and avoid precipitate formation. We also used IDC/O_2 as a mild oxidant to contrast with ITC. Films deposited under otherwise identical conditions but in the absence of surfactant were prepared for comparison.

All the films were formed at room temperature on freshly peeled mica discs or cleaned alumina plates. Each substrate was placed in a 4-dram vial with 5 ml of solution containing sufficient reagents as specified above (and in Table 2.1) to result in the following concentrations: 20 mM pyrrole, 0.6 mM CTAB, 15 mM SDS, 1.5 M salt (NaCl), and 20 mM APS, ITC, or IDC. pH was adjusted to be between 2 and 4 using aqueous HCl as needed. Samples with SDS contained salt to increase the adsolubilization of monomer [34]. Substrates were immersed for 1 h before the oxidant was added as a concentrated solution. After 4 h polymerization, the substrates were rinsed with deionized water and dried in a desiccator for 1 d. A portion of the film from mica samples was carefully removed from the substrate by gentle scraping with a razor blade while it was still wet, leaving a sharp film edge for thickness measurement. Dried samples were glued to steel pucks for AFM study and a conduction path between the film and the puck was created by silver glue for STM study.

2.3 Results and Discussion

2.3.1 Film Thickness

Film thickness can be directly measured using AFM across the edge of the film on mica. Before scanning, AFM can be calibrated in the vertical direction by a grid sample with fixed depth. Since our AFM is constantly run over a variety of height ranges, the depolarization of the piezotube with time should be small. Thicknesses for Mica-APS samples range from 150–170 nm. In contrast, Mica-APS-SDS-Salt and Mica-ITC-CTAB samples are about 33 and 56 nm thick, respectively, and are reproducible. A typical picture of cross-section analysis for thickness measurement is shown in Fig. 2.1. Hence, PPy samples deposited in the presence of surfactant give much thinner films than those deposited without. All the films are perceptible to the naked eye, although the surfactant-formed films are sufficiently thin to be transparent and not easy to distinguish from the bare mica. Since a mica disc bears very little surface area for adsorption and adsolubilization, the initial pyrrole concentration is more than sufficient to reach saturation in the bilayer or on bare mica, which means a large excess of monomer will be polymerized in the supernatant. Some roughening of the film comes from the precipitation of PPy clusters formed in solution. The precipitate is loosely attached to the film and can be rinsed away. This observation is consistent with a confining effect of the bilayer on the film formation and thus possibly affects the polymer structure. Thickness is not controllable in the absence of surfactant.

Although polymerization with surfactant present gives thinner films, the thicknesses are still much greater than that expected for surfactant bilayers alone. This means more monomer diffuses into the bilayer during polymerization as previously reported by Wu *et al.* for AP [45]. Generally, AP is done at a surfactant concentration slightly lower than its critical micelle concentration (CMC) to avoid micellization. If micelles are formed, they will compete for monomer with admicelles and the nominal free monomer concentration in solution will become lower, which may lead to insufficient monomer density for polymer nucleation in the admicelle as reported by Funkhouser *et al.* [34]. By adding salt, as in the Alumina-APS-SDS-Salt and Mica-APS-SDS-Salt samples, for which the SDS concentration (15 mM) is about twice the CMC ($\sim$ 8.5 mM in pure water [46]), the adsolubilization of monomer into admicelles was found to increase and film formation was possible.

However, the parallel emulsion polymerization in solution is not desired in thin film deposition because monomer will be wasted. In contrast, Mica-ITC-CTAB samples, prepared below the CMC ($\sim$ 0.95 mM in pure water [15,46,47] while 0.6 mM in $NaClO_4$ or KBr electrolyte [48]) with no salt added, result in thin films as expected for normal AP. On one hand, the longer tails of CTAB, which can accommodate more monomer, lead to larger thicknesses. On the other hand, the strong oxidant used in the Alumina-APS-SDS-Salt system may lead to oxidation of SDS and formation of by-product species that undermine film growth.

2.3.2 Film Morphology

PPy films on mica from SDS-salt solutions look like a network of well-connected polymer spheres with voids in between (Fig. 2.2). We can easily observe the mica substrate (dark areas) through the holes from the top-view image as well as cross sectional profiles of the film (not shown). The film is basically a layer of discrete PPy particles that appear to have nucleated at many sites and merged. Although the mica surface is not fully covered by PPy at this thickness, the film is still globally continuous since it shows good electrical conductivity (9.3×10^{-2} S/cm) on an insulating substrate. We can also see in Fig. 2.1 delaminated or folded patches of the film which means the film is mechanically integrated and flexible. In addition, fine PPy clusters and individual PPy particles can be seen scattered over the film. These particles derive from polymerization in the bulk. Films formed with CTAB present give similar results but with fewer see-through holes due to its larger thickness. Both surfactant-mediated films are macroscopically smooth and uniform in local structures. In comparison, electropolymerized thin PPy films using SDS as electrolyte (dopant) are also reported to give a nearly constant excess surface area (also called the roughness factor) over a wide range of thicknesses [49], indicating well-controlled surface morphology due to the presence of surfactant.

Mica samples prepared in the absence of surfactant exhibit a compact layer of PPy nodules with almost no pinholes. In addition to PPy particles precipitated from the solution, we observe the emergence of wrinkles inside the thick film (Fig. 2.3). The wrinkles come in a variety of densities and sizes even on the same sample and can be singly or multi-branched. The wrinkle height is usually a few microns and the diameter of the circular region spanned by one triply branched unit can go from order 10 μm to 100 μm. Wrinkles can combine to form a web or network and a secondary structure yielding "wrinkled wrinkles" is also observed (Fig. 2.4). Generally, the wrinkled film is globally rough but the local constituent granules are similar in size to those made in the presence of surfactant. However, the more compact and thicker film prevents us from observing the underlying substrate using AFM.

The wrinkles observed using STM are consistent with those in AFM images (Fig. 2.5, top). Since mica is electrically insulating, the STM image implies good conductivities of both wrinkly and planar regions of the film. Flat regions of the film comprise granular structures (Fig. 2.5, bottom) while fibrous structures on the ridges revealed by STM have been reported previously [36]. For the case of an alumina plate substrate, an STM image of PPy prepared in the absence of surfactant was also obtained showing a rough texture. Due to its roughness, determination of the PPy thin film conductivity on the alumina plate was not practical. The inability to determine thickness and uncertainty whether the roughness is inherent to the film or induced by the substrate led us to prepare samples on mica.

In electropolymerization one can see that wrinkling takes place only at the early stage of deposition so that wrinkles only appear on the electrode-facing side but not the solution-facing side and that the height of the wrinkles is smaller than the film thickness [33]. When the film approaches tens or hundreds of microns in thickness, the wrinkles are buried within the film and the surface morphology conforms to the typical cauliflower structures. In our case, the film is relatively thin so that we can see wrinkles from the top.

2.3.3 Surface Analysis

The surface morphologies of bare and PPy-coated alumina plates are shown in Fig. 2.6. Differences in the AFM images are subtle, prompting fractal analysis. At large image size, the alumina plate exhibits plateaus and valleys (left column). An Alumina-APS sample (upper left) shows clear granular structures covering up the flat regions, compared with the other two samples. The film looks thick and black to the naked eye. The bare alumina plate (bottom row) has the original white color and smoother plateau regions. Although an Alumina-APS-SDS-Salt sample (middle left), like the bare plate, gives similar flat regions along with some big holes, the sample color is gray. Granular structures of PPy appear in the magnified image (middle right). As we see at the smaller scale, all the samples show granular structures and it becomes difficult to tell PPy from alumina particles (right column). Even though visual checking of the sample color can easily tell whether there is PPy on the substrate, efficient image analysis needs to be done to quantitatively characterize the film morphology with AFM.

Measuring the surface fractal dimensions of bare and PPy-coated alumina plates can help discern the existence of the film. In Fig. 2.7 we see that on alumina the FD of Alumina-APS-SDS-Salt surface falls between those of Alumina-APS and bare alumina surfaces. Each point in the plot represents an average based on several samples and locations. A natural surface is statistically a self-affine fractal and the FD is used to detect the repeating structures on iteratively smaller scales. For mathematical or deterministic fractals, FD is independent of image size. However, for real fractals, if the repeating structures are lost or changed in some scale ranges, a doubly logarithmic plot of surface area vs. cell size will give several line segments with different slopes representing regions of different fractal behaviors. As for PPy film, repeating granular structures over a wide scale range are observed, so FD should be a suitable way to characterize the surface. Because the shade or darkness of the film on white alumina presumably increases with the film thickness, the consistency of the trend in FD between different alumina samples with that in shade implies a similar trend in film thickness, which is shown by the trend in thickness measured on the mica samples prepared under corresponding conditions. The surface FD, a measurement of surface roughness, therefore serves as an index of the film thickness, the amount of coated PPy, the degree of surface roughening, or the gray scale for the alumina samples. Bare alumina plate is the least fractal in nature among the alumina samples due to compression and sintering from the manufacturing process. A dependence of FD on image size is caused by the global structure of the bare alumina plate. At larger image size, inherent valleys and peaks on the surface of the alumina plate contribute to FD. In our case, the suitable image size for measuring FD is between 1 and 5 μm which encompasses most granule sizes of PPy and excludes the effects of valleys and small alumina particles.

Excess surface area (R_s) holds a similar trend to FD (Fig. 2.8). Discrete features and fractal structures will both contribute to this value. The thickest film has the greatest R_s and the bare plate has much smaller R_s than both the PPy-coated films. This shows that PPy granules determine the R_s. The largest difference in R_s between the coated and bare samples occurs at 5 μm, which indicates the incorporation of large and randomly scattered PPy aggregates. For all the samples, R_s increases with image size as a result of the inherent surface structures of the alumina plates. Statistical surface parameters such as the root-mean-square and mean roughnesses mainly give us the average height variation of the surface. They convey little information about the periodicity and density of surface features and about the local and fine structures of the surface. As shown above, FD and R_s are clearly useful in analyzing a microscopically rough surface obtained using AFM.

2.3.4 Fractal Growth of the Film

APS is a much stronger oxidant than ITC, while IDC is a reductant. Oxidation of pyrrole with IDC may result from reaction with the small amount of ITC formed by atmospheric oxygen at low pH. By using IDC one is able to slow the reaction rate and the formation of PPy on substrate, which may give us insight to the film growth mechanism. In the sample Mica-IDC, many fractal objects are observed (Fig. 2.9, top). The fractal "fingers" vary in size and density from place to place and are similar to those observed in electrochemical deposition of PPy and poly(3-dodecylthiophene) which extend from the anode towards the cathode [50, 51]. Some small fractals are triply branched but the large ones are more dendritic and never observed in ITC or APS oxidized samples. In addition, numerous PPy nuclei formed at a later stage around the fractals indicate that surface nucleation serves as the film growth mechanism in a non-surfactant solution. It is well known that fractal structures can be modeled by diffusion-limited aggregation (DLA) [52, 53]. The 2D fractal structures observed by us indicate that aggregation occurs mainly between adsorbed, mobile monomers and oligomers. The whole process of fractal formation thus includes adsorption, surface diffusion, nucleation, and aggregation of active molecules. The slow oxidation rate of pyrrole by IDC/O_2 in solution reduces the flux of activated PPy oligomer towards mica, which hinders the formation of 3D fractals. The mobility of adsorbed PPy particles then determines the fractal formation. The moving moieties meet with one another on the surface and form fixed nuclei. As the nucleus density increases with time, the possibility of forming new large fractals will be greatly reduced and compact clusters will take over. A similar transition is observed in the sample Mica-IDC-CTAB (Fig. 2.9, bottom) which shows a second structure of compact anomalous aggregates, indicating a decreased mean free path of mobile monomer or oligomer due to their higher concentrations close to the surface and to the confining effects of the CTAB bilayer. Smaller fractals with higher distribution density are observed. Therefore, the admicelle is found to facilitate more nucleation sites and aid in avoiding fractal aggregation of PPy. In samples made with strong oxidant, fractal structures are not observed because the effect of surface diffusion is greatly surpassed by that of nucleation due to fast oxidation, coupling, and deposition of monomer.

2.3.5 Film Growth Mode

There are several routes involved in typical pyrrole polymerization and deposition [5,23,54]. For electrochemical approach, monomer goes to the anodic electrode at a positive potential and releases one electron. The cationic radical goes back to the solution and couples with other radical monomer or oligomer. As to chemical· polymerization, monomer is oxidized in solution by added oxidant. The oligomer can either nucleate on the electrode or substrate and start growing films or form a polymer cloud (or so called soluble PPy) in the solution. In addition to direct radical formation, monomer oxidation can be catalyzed by metal oxides formed on the electrode, by protons at low pH, or by discharged electrolyte ions at a high electrical potential. Therefore, the deposits of film or island can be a combined result of nucleus growth, oligomer deposition, and PPy moiety attachment from various oxidation routes.

To simplify our discussion, however, we consider the consequential morphological changes of PPy deposited at different growth conditions. An examination of phenomenological film growth modes can help us understand the presence of wrinkles and film morphology in general. There are three basic models for describing the growth of a material deposited on a solid surface [55, 56]. These models, though developed for atomic and ionic materials, may offer insight into polymer film growth by analogy. The first is called the island or Volmer–Weber (VW) growth mode by which the deposit forms separate islands on the substrate. This is a 3D growth mechanism and the deposit has a much higher cohesion force than the adhesion force of the interface. In other words, the deposit does not "wet" the substrate. The second is called layer-by-layer or Frank–van der Merwe (FM) growth mode. In this mode, the deposit starts forming complete monolayers, one at a time, from the substrate. This happens when the cohesion force is much smaller than the deposit-substrate adhesion force. The growth mode in this case is purely 2D. When both the cohesion and adhesion forces are comparable, we get a third model which is called the layer-plus-island or Stranski-Krastanov (SK) growth mode. The deposit will form a monolayer or multilayer on the substrate first. Then islands nucleate and grow upon it. The reason the film growth changes from 2D to 3D is that the upper layers undergo some kind of "surface relaxation" process in order to reduce the strains caused by the lattice mismatch between the deposit and the substrate. If tiny 3D islands with high distribution density form first according to the VW mode, they may extend to merge with one another and form a "thick monolayer". Based on the completed layer, one may get a "pseudo" FM or SK growth mode.

Generally, PPy tends to form an "initially connected layer" (ICL) on the substrate first, as shown by the anisotropic growth of PPy deposit. Before the well-connected first layer forms, PPy oligomer nucleates on the substrate in numerous places, which is also demonstrated by the fractal structures formed at low reaction rates in the presence of IDC/O_2. When the interaction between the substrate and PPy is strong, the nucleation rate is fast, site density is high, and the nuclei grow quickly in the lateral directions. The distance between nuclei is relatively small so when they grow into each other, a thin ICL forms. When the interaction between the substrate and PPy is weak, the nucleation rate is slow and the site density is low. Nuclei will grow both laterally and vertically as islands. The islands keep growing until they meet one another and form a thick ICL. Therefore, the ICL comes from multiple nucleation sites with either isotropic or anisotropic growth rates on the substrate. At some point, the thickening film starts shrinking and wrinkles result. Such a contraction (see below) represents the release of stress from the substrate. The local film surface still appears as granules. Of the three models, we find that the pseudo SK model seems to best fit the results because of the transition from wetting to non-wetting.

When surfactant is added, however, a "thin monolayer" will form and quickly become connected due to highly concentrated and homogeneously distributed pyrrole inside the bilayer. This monolayer keeps growing, if a continuous supply of monomer is available, and finally starts shrinking. Therefore, surfactant-mediated PPy thin films can be said to follow the real SK model.

According to our observations, there are two types of PPy film deposited on mica at low pyrrole concentrations (e.g. 20 mM), no matter whether a surfactant is used. One is a non-wrinkled film with a thickness below 100 nm and the other, a thicker wrinkled film. In brief, both the electrochemical and chemical systems show that wrinkling happens primarily at the film-substrate interface and is related to the film growth mode at the early stage of deposition.

2.3.6 Film Wrinkling

While wrinkles in PPy thin films have been reported previously [10, 18, 20, 33, 36, 57–59], the reason for their formation remains an issue. Most of the work has been done on electropolymerized PPy films. We aim to integrate earlier works with our own observations from the perspective of chemical oxidation.

Shape Changes in PPy

In addition to post-deposition morphological change [25], deformation of unattached PPy films due to adsorption of foreign materials like water and organic solvent has been reported recently [60,61]. Such adsorption of polar molecules can cause a polymer strip to "bend". It is interesting that the bending direction can be reversed by substitution of alcohol for water. However, the bending process is a post-deposition phenomenon which does not alter the existing surface morphology of the polymer. But it does show that PPy has special structural and functional groups to interact with the adsorbate, which may cause wrinkling during polymerization. Similarly, redox-induced bending of PPy/Mylar bilayer strips reported by Shimoda and Smela [2] shows that the PPy side contracts due to internal stress before performing doping/dedoping to the film, indicating the stress buildup during PPy film deposition.

Wrinkling vs. Film Adhesion

There are several important observations about the film wrinkles. Firstly, the wrinkles are hollow ridges as proved by removing the film from mica with adhesive tape and using AFM to scan the substrate-facing side of the film (Fig. 2.10) [57,59]. Hollow ridges imply the film separates from the substrate after the ICL has been formed. Separation from the substrate indicates that sufficient stress has been supplied to the film to overcome the work of adhesion and break bonding to the substrate. When the film grows to a certain thickness, wrinkles occur and these wrinkles seem to grow with time and thickness. The delamination of the film proceeds with the extension and branching of ridges and finally results in a network (Fig. 2.4). Shapiro *et al.* report that wrinkling does not seem to depend on the film thickness [33]. Their conclusions were drawn from electrochemically grown PPy films of a much larger film thickness range, 10–80 μm, over which the film is thicker than the wrinkle height. In this study, we find that the film is much thinner (30–180 nm) than the wrinkle height (1–5 μm) and that the thicker the film, the greater the wrinkling. Therefore, in the early stage of film growth, wrinkling does depend on the film thickness.

Control of Wrinkling

As mentioned above, separation of the film from the substrate requires overcoming a work of adhesion. The larger the work of adhesion, the more difficult it is to form wrinkles in the film. Therefore, by increasing adhesion between the film and substrate, one is able to avoid or suppress the formation of wrinkles. During polymerization of pyrrole, there are five factors that may affect the adhesion to the substrate and can be used to control the formation of wrinkles. Substrate, surfactant, monomer, oxidant, and water are each examined in separate sections below.

Substrate Both the physical and chemical nature of the substrate will affect the adhesion of PPy thin film. Firstly, substrate roughness reduces formation of wrinkles. We have observed that a microscopically rough surface such as an alumina plate can give wrinkle-free coatings independent of whether a surfactant is used or not. Therefore, substrate roughness can help suppress the wrinkles. According to Shapiro *et al.* the porous nature of the substrate promotes the growth of fiber-like structures which leads to the wrinkled morphology of PPy thin film [20, 33]. That is, rough substrate may provide preferential nucleation sites for faster PPy growth and branching during electrodeposition. In contrast, our results, based on chemical oxidation, show that even on an atomically smooth mica surface, hollow wrinkles can still occur all over the sample and seem to be independent of the underlying mica steps and defects.

Moreover, we find that wrinkling cannot be suppressed in PPy thin films deposited in the absence of surfactant on rough nickel foil. This indicates the chemical nature of the substrate can also affect the formation of wrinkles. In contrast, hydrophobic substrates such as polystyrene (PS), polyethylene (PE) and graphite (HOPG) are found to suppress wrinkling of PPy films. This is due to stronger polymer-substrate adhesion. Pigois-Landureau *et al.* report that the adhesion of PPy is stronger to clean noble metals than to glass or ITO substrates; the adhesion is also stronger for doped (charged) PPy than for the dedoped neutral PPy [18]. The concept of interfacial adhesion here also supports the report of Shapiro *et al.* that PPy deposited on Pt and other metal anodes results in no wrinkling. Hence, we summarize that surfaces with low hydrophilicity such as plastics, noble metals, and some steels generally give fewer wrinkles than mica, glass, minerals, and metal oxides.

Chu *et al.* report crystalline fibers formed in a chemically polymerized, free-standing film of PPy formed at the air-liquid interface [10]. By comparing their observations with ours, we would suggest that the (branched) fibers are actually wrinkles. Therefore, at the air-liquid interface, the wrinkling of the film in the absence of a solid substrate indicates low adhesion between the film and supporting water phase. The reported film thickness ranges from 10–80 nm, showing again that without strong adhesion wrinkles even occurs in very thin films.

Surfactant In most cases, we found that by using surfactant admicelles as a template we can get a thin and well-connected film free of wrinkles. Films deposited on solids without using surfactant are generally thicker and full of wrinkles, indicating that surfactant improves the film-substrate adhesion. In this case, the head group offers favorable interaction with the substrate and the tail with the polymer. In general, PPy films polymerized in the presence of CTAB are thin, free of wrinkles, and as thick as those polymerized in SDS-salt solutions, which means at a fixed pyrrole concentration and with sufficient oxidant, film thickness does not strongly depend on the type of surfactant.

During AP, diffusion into admicelles controls the availability of the monomer for polymerization on the surface and thus the rate of film growth. For the same reaction time, admicelle-modulated films are found to be thinner than those grown by random deposition. In addition to enhancing the adhesion force between PPy film and substrate, the surfactant is able to help control the film thickness and quality. Therefore, by using surfactant, adhesion is increased but cohesion is decreased.

Monomer At low initial monomer concentrations, films cannot grow infinitely in thickness due to the limited amount of pyrrole. But at a relatively high initial concentration of pyrrole (e.g. 100 mM), films can grow thicker. Wrinkles covered with a layer of PPy clusters are observed even in the surfactant-mediated films because the internal cohesion has overcome the interfacial adhesion. When the initial pyrrole concentration goes higher, a very thick film can be deposited as a result of both film growth and cluster precipitation from the solution. Cauliflower structures are observed on the dried film without rinse. Wrinkles are in this way buried inside the film.

Therefore, a continuous supply of monomer will ultimately result in a film thick enough to cause wrinkle formation. It is necessary to keep a low monomer concentration if one is to avoid wrinkles during thin film deposition.

Oxidant With a low concentration of oxidant, the reaction rate will be decreased at the solid-liquid interface. Even in the absence of surfactant, the film remains thin and is free of wrinkles. With a slow film growth rate, the reaction may stop, due to exhaustion of oxidant, before a critical thickness is reached. Therefore, it is also important to select appropriate oxidant concentration to avoid wrinkles.

Water It is generally assumed that evaporation of water from the film will cause wrinkling but we find by optical microscopy that wrinkles have already formed when the film is still wet, which is consistent with others' reports [10, 33]. For thin films prepared from surfactant solutions at low initial pyrrole concentrations, wrinkling does not appear either *in situ* or when the films are dried. Therefore, water loss is not playing a dominant role in wrinkle formation.

In summary, to build a PPy film without wrinkles, one should use rough or hydrophobic substrates, apply surfactant, and keep oxidant and monomer concentrations low.

Mechanisms for Wrinkling

Basically, wrinkling is a delamination process, occurring due to contraction, expansion, and dewetting of the film. In contraction the film shrinks either globally or locally because of lateral tensile forces and wrinkles are created by induced vertical forces. Expansion results from external substances being incorporated into the film upon or after polymerization. When the film expands due to addition of mass and thus increases in volume, sinking points or lines of lateral compressive forces emerge and are pushed up toward the unconstrained dimension, the solution phase. By dewetting the film separates from the substrate by direct vertical forces. All the three sub-processes have one common prerequisite that a film or film patches must have formed before wrinkling. If there is no well-connected film or patches in contact with each other, wrinkling would not be possible.

There are several possible mechanisms for each sub-process. Contraction can be induced by ambient heat, volume changes upon cooling and crystallization, internal stress relaxation during film thickening, inter- or intramolecular hydrogen bonding due to overoxidation, and dedoping of the film. Expansion can be invoked by doping and lateral growth of the film. If doping is responsible for wrinkling, then hindered diffusion or exchange of small ions through the film may explain the tendency for wrinkling not to occur in the presence of surfactant. Dewetting can be caused by deprotonation of PPy, electrostatic repulsion between the film and substrate, osmotic forces across the film, and mechanical forces associated with the diffusional flows of reactants and PPy particles. No matter which mechanism(s) is occurring, once the film pulls away from the substrate, wrinkles are created.

Film Contraction upon Thickening

Based on our observations, thickening of the film is accompanied by a change in surface morphology. As mentioned above, wrinkles emerge at the early stage of polymerization when the film thickness is still on the nanometric scale. After stresses are relieved by wrinkling, the subsequently thickened film becomes less or non-stressed and no more wrinkles form. This implies that stress is induced mainly by interaction between the film and substrate. During polymerization, nuclei form first from which molecules grow laterally due to more energetically favorable sites at edges instead of protruding into solution. As nuclei touch one another, stress is created by cohesion among connected nodules. As the stressed network continues to grow in thickness and compactness, cohesion increases and finally exceeds interfacial adhesion. The film shrinks at randomly distributed contracting points. The tensile force between one pair of contracting points will cause a wrinkle branch to form. The resultant effect of all the tensions produces a network of wrinkles. Therefore film contraction upon thickening is proposed as the mechanism for wrinkle formation in PPy films.

2.4 Conclusions

In this study we used admicellar polymerization to deposit PPy on alumina and mica and characterized the films using AFM, STM, and optical microscopy. The films from surfactant solutions are smooth, well-connected, and as thin as 30–60 nm, while those from non-surfactant solutions are thicker than 150 nm and full of wrinkles. Fractal analysis is proved useful to make quantitative characterizations of rough films on rough substrates. Fractal structures were found on mica when the reaction rate was very slow and were suppressed in the presence of admicelles.

A (Pseudo) Stranski-Krastanov model is used to describe PPy film growth with surface morphology changing from smooth to wrinkly. Surfactant, rough and hydrophobic substrates, and low monomer and oxidant concentrations are found to help suppress wrinkle formation. Thickening-induced film contraction is proposed to promote wrinkling.

2.5 Acknowledgment

The author would like to acknowledge the financial support from the National Science Foundation (OST-9550478 and CTS-9521985) and the industrial support of the Institute for Applied Surfactant Research. Funding for the SPM system was provided by the Oklahoma Center for the Advancement of Science and Technology.

Bibliography

[1] I. Berlot, P. Labbé, J.-C. Moutet, Langmuir 16 (2000) 5814.

[2] S. Shimoda, E. Smela, Electrochim. Acta 44 (1998) 219.

[3] G.E. Barr, C.N. Sayre, D.M. Connor, D.M. Collard, Langmuir 12 (1996) 1395.

[4] D.M. Collard, M.S. Stoakes, Chem. Mater. 6 (1994) 850.

[5] C.C. Hsueh, A. Brajter-Toth, Anal. Chem. 66 (1994) 2458.

[6] R.C.D. Peres, V.F. Juliano, M.-A. de Paoli, S. Panero, B. Scrosati, Electrochim. Acta 38 (1993) 869.

[7] M. Nishizawa, Y. Miwa, T. Matsue, I. Uchida, J. Electroanal. Chem. 371 (1994) 273.

[8] D.M. Collard, M.A. Fox, J. Am. Chem. Soc. 113 (1991) 9414.

[9] X. Hong, J.C. Tyson, J.S. Middlecoff, D.M. Collard, Macromolecules 32 (1999) 4232.

[10] X. Chu, V. Chan, L.D. Schmidt, W.H. Smyrl, J. Appl. Phys. 77 (1995) 6658.

[11] X. Chen, J. Devaux, J. Issi, D. Billaud, Polym. Eng. Sci. 35 (1995) 642.

[12] Y. Shen, M. Wan, J. Polym. Sci.: Part A: Polym. Chem. 37 (1999) 1443.

[13] J. Wu, J.H. Harwell, E.A. O'Rear, Langmuir 3 (1987) 531.

[14] J. Wu, J.H. Harwell, E.A. O'Rear, S.D. Christian, AIChE Journal 34 (1988) 1511.

[15] J.H. O'Haver, J.H. Harwell, E.A. O'Rear, Langmuir 10 (1994) 2588.

[16] C.L. Lai, J.H. Harwell, E.A. O'Rear, Langmuir 11 (1995) 905.

[17] B.P. Grady, E.A. O'Rear, L.S. Penn, A. Pedicini, Polym. Comp. 19 (1998) 579.

[18] E. Pigois-Landureau, Y.F. Nicolau, M. Delamar, Synth. Met. 72 (1995) 111.

[19] Y.F. Nicolau, S. Davied, F. Genoud, M. Nechtschein, J.P. Travers, Synth. Met. 41–43 (1991) 1491.

[20] M.J. Miles, W.T. Smith, J.S. Shapiro, Polymer 41 (2000) 3349.

[21] M.F. Suárez, R.G. Compton, J. Electroanal. Chem. 462 (1999) 211.

[22] E.M. Girotto, M.A. de Paoli, Adv. Mater. 10 (1998) 790.

[23] X.W. Cai, J.S. Cao, Z.X. Xie, Y. Xie, Z.Q. Tian, B.W. Mao, Langmuir 14 (1998) 2508.

[24] J. Li, E. Wang, M. Green, P.E. West, Synth. Met. 74 (1995) 127.

[25] J. Li, E. Wang, Synth. Met. 66 (1994) 67.

[26] M.C. Montemayor, L. Vazquez, E. Fatás, J. Appl. Phys. 75 (1994) 1849.

[27] K. Sasano, K. Nakamura, K. Kaneto, Jpn. J. Appl. Phys. Part 2 32 (1993) L863.

[28] G. Merle, A.C. Grillet, J. Allemand, D. Lesueur, Polymer Testing 18 (1999) 217.

[29] M.P. Everson, J.H. Helms, Synth. Met. 40 (1991) 97.

[30] E. Chaînet, M. Billon, J. Electroanal. Chem. 451 (1998) 273.

[31] J.R. Reynolds, C.K. Baker, C.A. Jolly, P.A. Poropatic, J.P. Ruiz, in: J.M. Margolis (Ed.) Conductive Polymers and Plastics, Chapman and Hall, New York, NY, 1989.

[32] S. Machida, S. Miyata, Synth. Met. 31 (1989) 311.

[33] J.S. Shapiro, W.T. Smith, Polymer 38 (1997) 5505.

[34] G.P. Funkhouser, M.P. Arévalo, D.T. Glatzhofer, E.A. O'Rear, Langmuir 11 (1995) 1443.

[35] G. Cho, D.T. Glatzhofer, B.M. Fung, W.-L. Yuan, E.A. O'Rear, Langmuir 16 (2000) 4424.

[36] G. Cho, Bull. Chem. Soc. Jpn. 70 (1997) 2309.

[37] T. Silk, Q. Hong, J. Tamm, R.G. Compton, Synth. Met. 93 (1998) 65.

[38] J.D. Kiely, D.A. Bonnell, J. Vac. Sci. Technol. B 15 (1997) 1483.

[39] J.M. Williams, J.T.P. Beebe, J. Phys. Chem. 97 (1993) 6249.

[40] J.M. Williams, J.T.P. Beebe, J. Phys. Chem. 97 (1993) 6255.

[41] N. Almqvist, Surf. Sci. 355 (1996) 221.

[42] J.C. Russ, The Image Processing Handbook, 3rd Ed., CRC Press, LLC, Boca Raton, Florida, 1999.

[43] L.T. Fan, D. Neogi, M. Yashima, Elementary Introduction to Spatial and Temporal Fractals, Springer-Verlag, Berlin, 1991.

[44] NanoScope Command Reference Manual, Digital Instruments, 1997.

[45] J. Wu, J.H. Harwell, E.A. O'Rear, J. Phys. Chem. 91 (1987) 623.

[46] M.J. Rosen, Surfactants and Interfacial Phenomena, 2nd Ed., John Wiley & Sons, New York, 1989.

[47] M.W. Rutland, J.L. Parker, Langmuir 10 (1994) 1110.

[48] A.B. Mandal, B.U. Nair, J. Phys. Chem. 95 (1991) 9008.

[49] T. Silk, Q. Hong, J. Tamm, R.G. Compton, Synth. Met. 93 (1998) 59.

[50] A. Harrison, Fractals in Chemistry, Oxford University Press, Oxford, Great Britain, 1995.

[51] M. Fujii, K. Arii, K. Yoshino, J. Phys.: Condens. Matter 2 (1990) 6109.

[52] T.A. Witten, L.M. Sander, Phys. Rev. Lett. 47 (1981) 1400.

[53] T.A. Witten, L.M. Sander, Phys. Rev. B 27 (1983) 5686.

[54] J. Rodríguez, H.-J. Grande, T.F. Otero, in: H.S. Nalwa (Ed.) Handbook of Organic Conductive Molecules and Polymers, John Wiley & Sons, New York, 1997.

[55] R.J. Stokes, D.F. Evans, Fundamentals of Interfacial Engineering, Wiley-VCH, Inc., New York, 1997.

[56] G. Staikov, in: A.A. Gewirth, H. Siegenthaler (Eds.) Nanoscale Probes of the Solid/Liquid Interface, Kluwer Academic Publishers, Dordrecht, the Netherlands, 1995.

[57] K. Idla, A. Talo, H.E.-M. Niemi, O. Forsén, S. Yläsaari, Surf. Interface Anal. 25 (1997) 837.

[58] S.J. Sutton, A.S. Vaughan, J. Mater. Sci. 28 (1993) 4962.

[59] B.R. Saunders, K.S. Murray, R.J. Fleming, R. Cervini, N.S. Allen, in: H.S. Nalwa (Ed.) Handbook of Organic Conductive Molecules and Polymers, John Wiley & Sons, New York, 1997.

[60] H. Okuzaki, T. Kunugi, J. Polym. Sci.: Part B: Polym. Phys. 34 (1996) 1747.

[61] H. Okuzaki, T. Kunugi, J. Polym. Sci.: Part B: Polym. Phys. 36 (1998) 1591.

Alumina Plate	**Mica Disc**
Alumina-APS-SDS-Salt	Mica-APS-SDS-Salt
Alumina-APS	Mica-APS
	Mica-ITC-CTAB
	Mica-IDC-CTAB
	Mica-IDC
Bare alumina plate	Bare mica disc

Table 2.1: Summary of samples prepared (SDS—sodium dodecyl sulfate; CTAB—cetyltrimethyl ammonium bromide; APS—ammonium persulfate; ITC—iron trichloride hexahydrate; IDC—iron dichloride tetrahydrate)

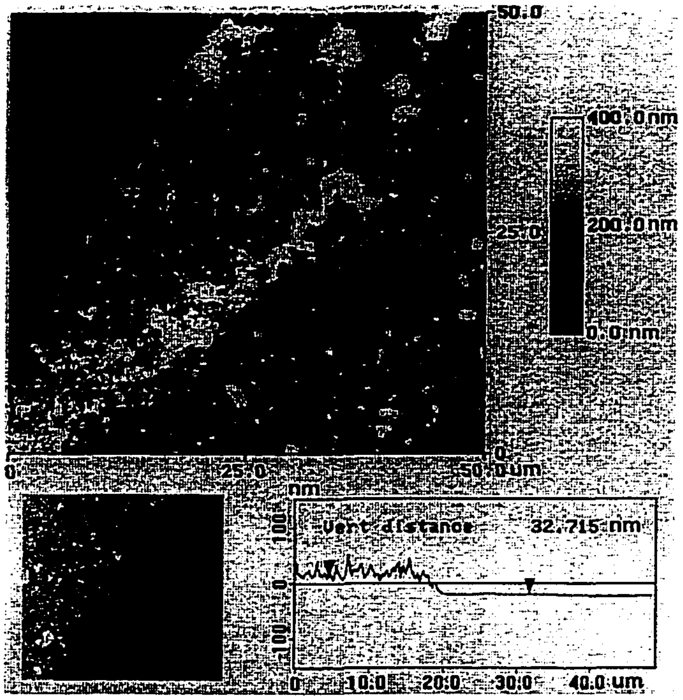

Figure 2.1: Top: Topographical view of Mica-APS-SDS-Salt scanned by the AFM. The folded film indicates good connectivity and flexibility of the film. The scan size is 50 μm × 50 μm. Bottom: Thickness measured across the film edge of Mica-APS-SDS-Salt scanned by the AFM. The value is about 33 nm.

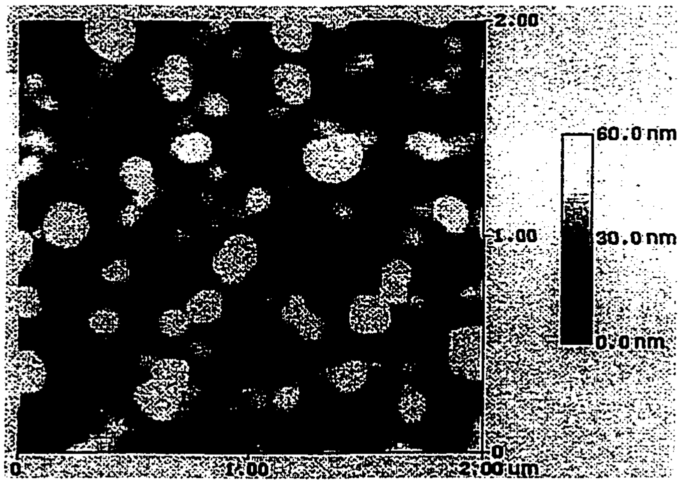

Figure 2.2: Topographical view of Mica-APS-SDS-Salt scanned by the AFM. The film is composed of well connected PPy granules. The scan size is 2 μm × 2 μm.

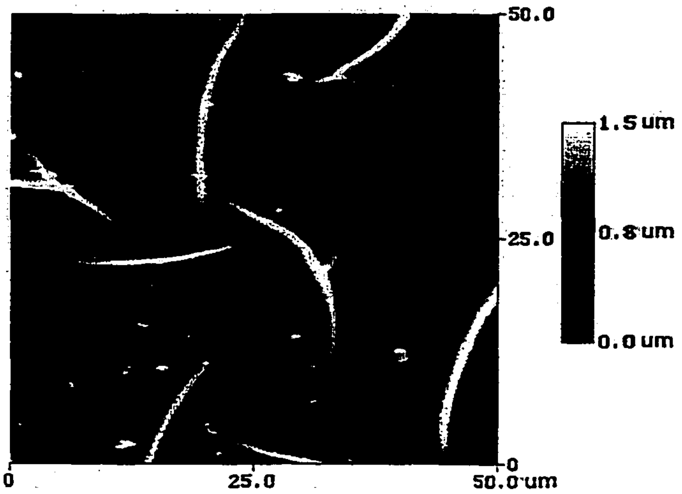

Figure 2.3: Topographical view of Mica-APS scanned by the AFM. Wrinkles of the film are clearly seen. The scan size is 50 μm × 50 μm.

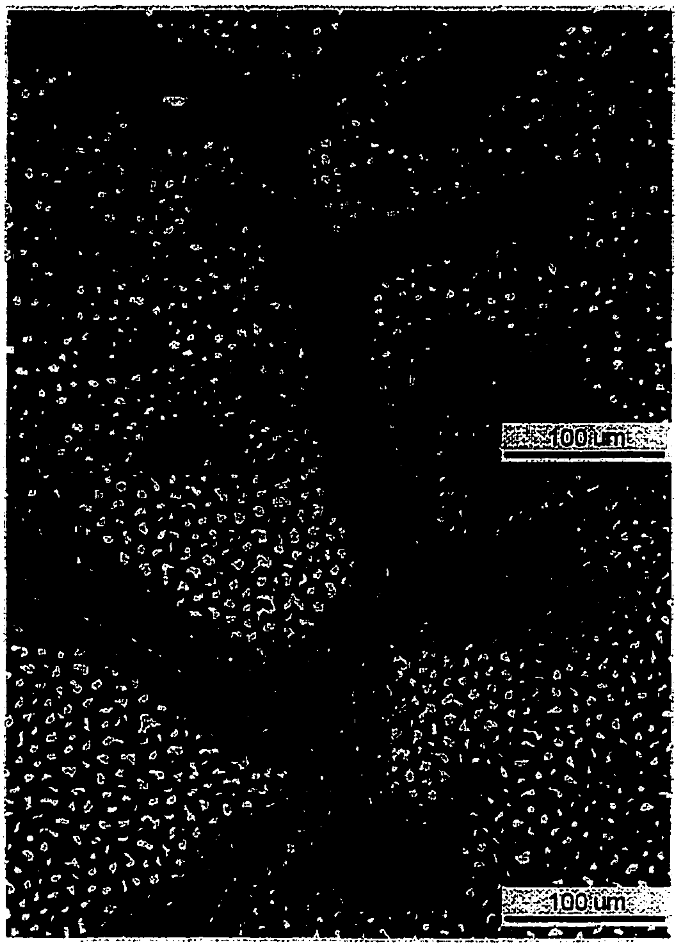

Figure 2.4: Optical micrograph of wrinkle structures of Mica-APS. Upper half is the top view of a wrinkled film while lower half is the mica-facing side (the back) of the film. We can see a small-wrinkle network (black cell walls) spanning the whole image. Huge wrinkles emerge from the network as a result of secondary wrinkling of the film. The upper half highlights the huge wrinkles while the lower half, small wrinkles. Huge wrinkles are composed of small wrinkles. The width of the image is 400 μm.

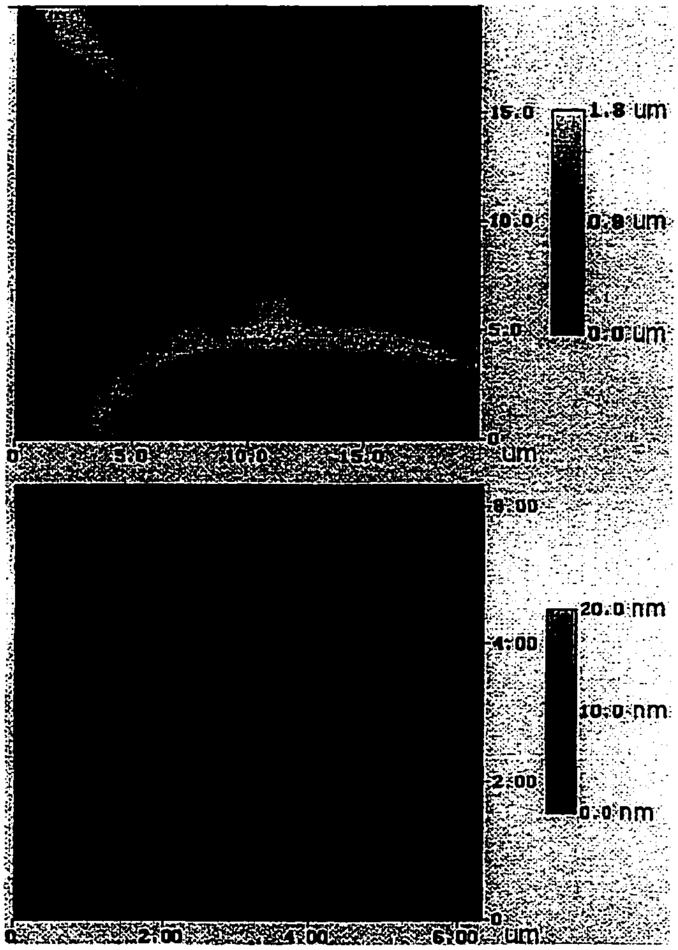

Figure 2.5: Topographical view of PPy film on mica using STM. Wrinkles of the film are similar to those observed using AFM (top, Bias = 3.6 V, Current = 3.0 nA). Flat regions of the film are composed of granules and a few pinholes (bottom, Bias = 1.0 V, Current = 1.0 nA). The scan sizes are 20 μm × 20 μm (top) and 6.4 μm × 6.4 μm (bottom).

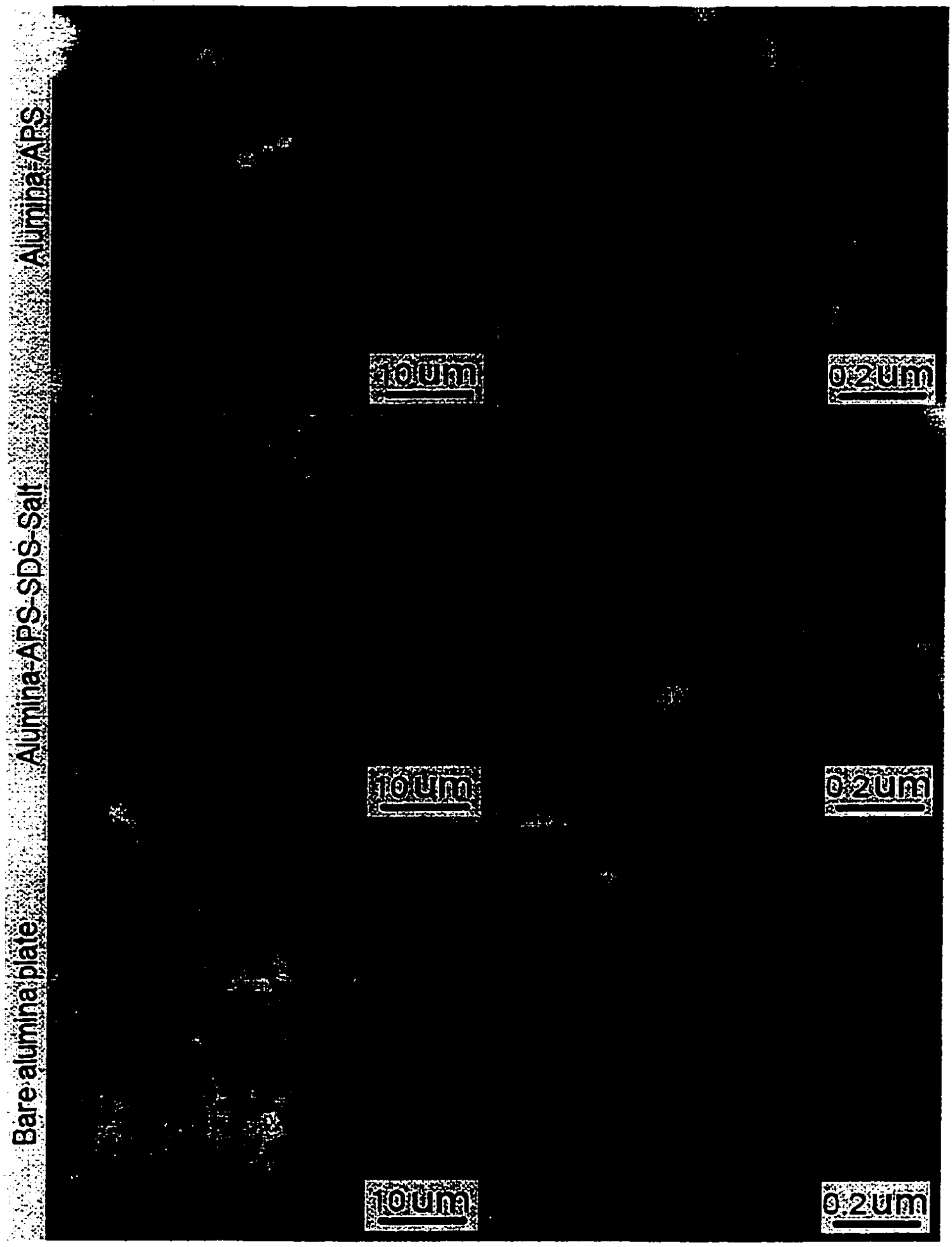

Figure 2.6: AFM images of Alumina-APS (top row), Alumina-APS-SDS-Salt (middle row), and bare alumina plate (bottom row). The image size on the left is 50 μm × 50 μm and that on the right is about 1 μm × 1 μm. In the left column, on one hand, Alumina-APS (top left) is rougher than the bare alumina surface (bottom left), which indicates the existence of PPy. On the other hand, Alumina-APS-SDS-Salt (middle left) looks as smooth and clean as the bare plate (bottom left). In the right column, both PPy-coated samples seem to give more and larger granular structures than the bare alumina plate, which is not always the case. However, fractal analysis can better contrast quantitatively those samples that all show granular features in small sized images.

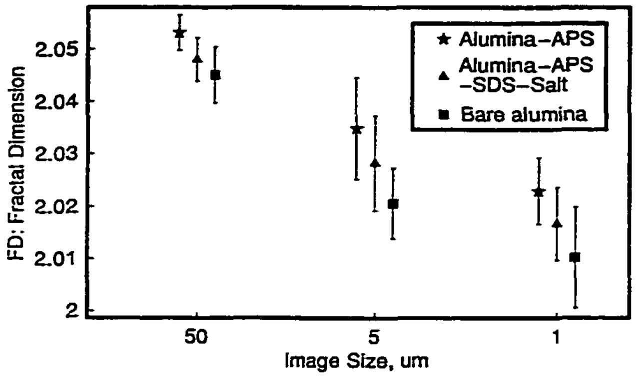

Figure 2.7: Fractal dimensions (FD) calculated for Alumina-APS, Alumina-APS-SDS-Salt, and bare alumina plate at different image sizes. Points for each image size set have been offset to facilitate error bar comparison. FD increases with the image size due to non-plateau regions of the plate. The bare alumina plate has the lowest fractal dimension which means the surface is relatively clean, smooth, and free of polymer granules compared with the other samples.

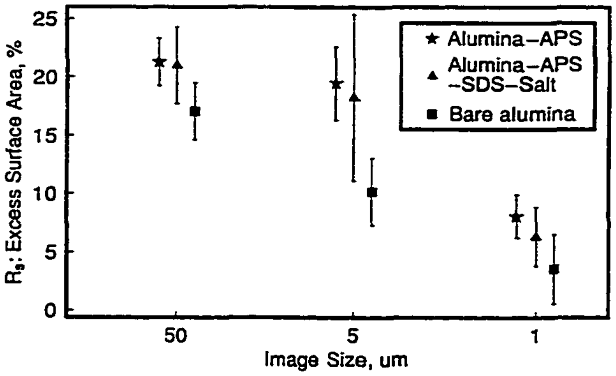

Figure 2.8: for Alumina-APS, Alumina-APS-SDS-Salt, and bare alumina plate at different image sizes. Image size increases with R_s. For the bare alumina plate, R_s decreases linearly with image size. Above 5 μm, R_s does not increase much for both Alumina-APS and Alumina-APS-SDS-Salt samples.

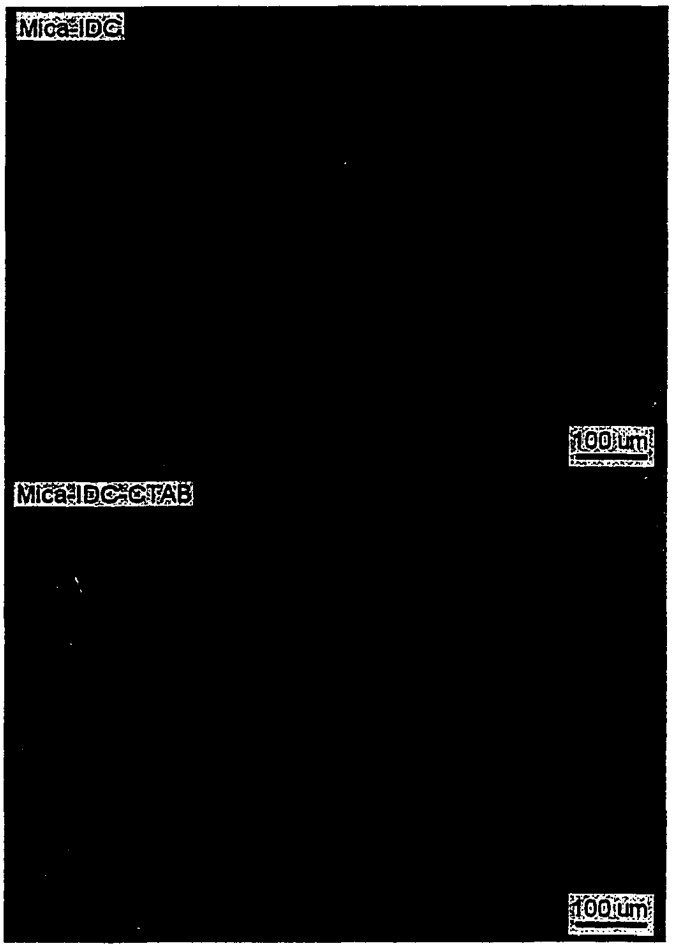

Figure 2.9: Optical micrographs of Mica-IDC (top) and Mica-IDC-CTAB (bottom). The horizontal length of the images are 900 μm. Mica-IDC consists of dendritic structures and dots while Mica-IDC-CTAB consists of smaller dendrites and anomalous dense patches.

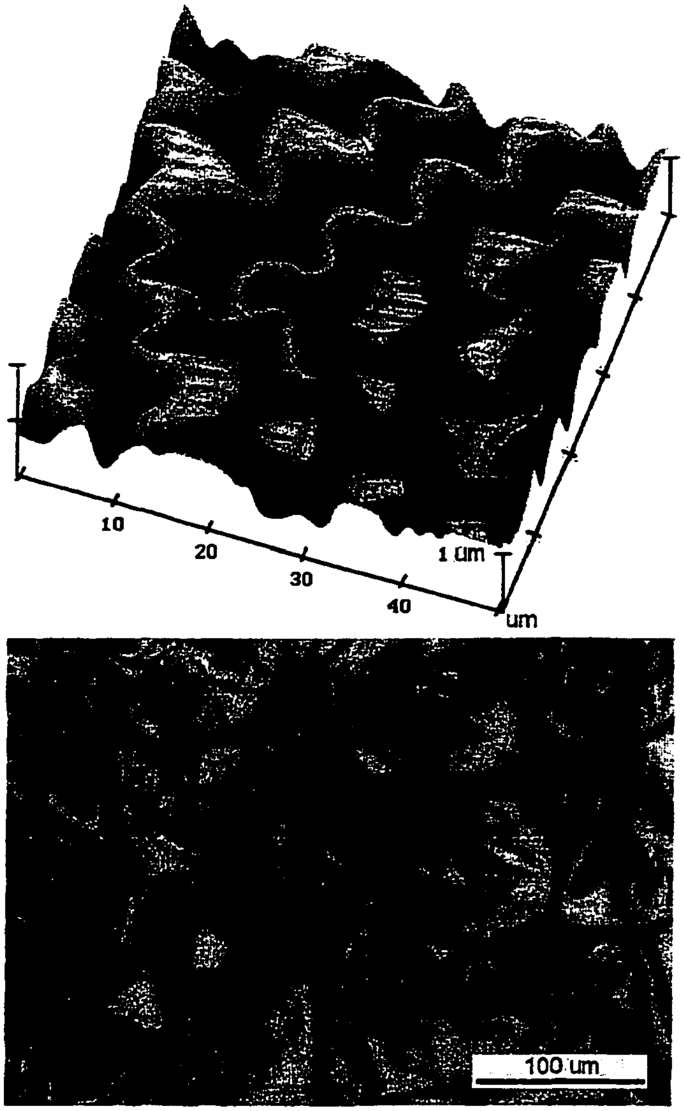

Figure 2.10: The 3D (top) and topographical (bottom) images of substrate-facing side of Mica-APS using AFM and optical microscopy, respectively. The back sides of wrinkled film are clearly seen and both images give similar morphologies. The AFM scan size is 50 μm × 50 μm. The horizontal length of the optical micrograph is 400 μm.

Chapter 3

Polypyrrole Ultrathin Films*

Admicellar polymerizations (AP) were conducted in aqueous solutions to form electrically conducting polypyrrole (PPy) ultrathin films on mica and graphite. Separate solutions were used for monomer adsolubilization and polymerization; so that at the start of the reaction, the only monomer in solution was localized at the solid-liquid interface. Film morphology and thickness were examined using contact mode and TappingMode atomic force microscopy and compared to our previous results where oxidant was added to the adsorbing solution. PPy films formed on graphite from water or surfactant solutions were mainly composed of inter-linked islands and nodules (small islands) at high density. On the other hand, PPy deposited on mica in water alone formed randomly scattered islands without any continuous film formation, while PPy from surfactant solutions were the same type of films with islands and nodules. The thickness of the well-connected films could be made less than 5 nm depending on reaction conditions and initial monomer concentration in the adsorbing solutions. The thicknesses are approximately an order of magnitude thinner than in previous work due to the change in the amount of monomer available for polymerization. Because the amount of monomer available for polymerization in this study is on the same order of magnitude as the amount of available monomer for admicellar polymerizations on high surface area particulates, this study probably better represents film thicknesses that occur in particulate systems as well.

---

*W.-L. Yuan, E.A. O'Rear, B.P. Grady, D.T. Glatzhofer, Nanometer-Thick Polypyrrole Films Formed by Admicellar Polymerization under Conditions of Depleting Adsolubilization, to be submitted for publication

3.1 Introduction

Polymer thin films are widely used in industry. Applying a polymer thin film to a solid can alter the physical and chemical properties of the surface. Electroactive polymeric films have been studied vigorously in the last two decades because of their wide application in composite materials and electronic devices. In general, electroconductive polymers and semiconductors have been used to fabricate organic thin film transistors and light emitting diodes. Most semiconductor devices consist of a stack of films. When the size of these solid-state devices is reduced, each component film must be made thinner. In order to keep each layer functioning properly and cooperating intimately with its neighboring layers, better understanding of film properties and interactions between layers on the nanometer scale is imperative. Since organic materials have advantages over inorganic ones such as ease of handling, low cost, and environmental compatibility, researchers are exploring organic substitutes for commercial electronic devices.

Among the numerous conductive polymers, polypyrrole (PPy) and its derivatives have received foremost attention because of its unique redox properties and good chemical and environmental stability. Thin PPy films can be modified to incorporate special functional groups such as ions, ligands, enzymes, and proteins to make (bio-) sensors or substrates for cell culture [1–4]. PPy has been used as an electrode material for rechargeable batteries and patterned into thin film resistors and organic circuits [5–7]. One limitation of PPy to optical devices is the opaqueness of thicker films.

Polymer thin films at solid surfaces often exhibit distinct properties from the bulk material because they are restricted in the basal direction and influenced by the substrate. A polymer thin film on a solid substrate can be made from either a polymer or monomer solution. In spin-casting, a polymer film forms from a drop of polymer solution that is placed onto a fast rotating plate. 'Layer-by-layer deposition' is another example of film formation using a polymer solution; dissolved polymers are deposited via multiple alternate immersions of the substrate into two different polymer solutions [8,9]. This technique does not involve chemical reaction and has been applied to ionic polyelectrolytes and nonionic polymers in aqueous and nonaqueous solutions, respectively. Film thicknesses around 50 nm have been reported and determined either by small angle X-ray scattering (SAXS) or by surface plasmon measurement (SP). Interaction between adsorbed layers is based on the charged or polarized side groups along the polymer chain. The 'layer-by-layer deposition' is also called the dipping technique. Neither technique is entirely suitable for PPy because the polymer does not dissolve in most solvents.

To synthesize electroactive thin films on a solid support from a solution containing monomer, two popular approaches are available: electrochemical [10–14] and chemical [15–18] oxidation. In electrochemical synthesis, monomer is polymerized and deposited on an electrode by a supplied charge, and the range of thickness spans from nanometers to microns. The resultant film morphology typically resembles cauliflower. To improve the lateral growth of PPy, the electrode has been rendered hydrophobic and thus the preferential adsorption of pyrrole or its oligomers is promoted [19–23]. Compared with electrosynthesis, chemical polymerization of thin films has advantages in large-scale production and cost economy. Thin films can be built from pyrrole through alternate immersions of the substrate into monomer and oxidant solutions; this process is also called 'layer-by-layer' deposition [24–27]. Film thickness achieved in this way ranges from several to hundreds of nanometers, as determined by X-ray photoelectron spectroscopy (XPS). In the present study, PPy thin films were chemically synthesized from a solution containing monomer using admicellar polymerization (AP). This technique utilizes a surfactant templates in bilayers or other conformations that self-assemble at the solid surface in an aqueous solution to attract monomer at the interface, leading to a 2D thin film upon polymerization. AP includes four steps: adsorption of surfactant onto the solid surface to form admicelles, adsolubilization of monomer from the solution into admicelles, polymerization inside the admicelles by an oxidizing agent, and exposure of the films by washing away excess surfactant [28–31].

Measuring film thickness when PPy is deposited on metallic particles or rough substrates is difficult; however recent reports showed that the thickness of thin PPy films deposited on mica can be directly measured by atomic force microscopy (AFM) across the film edge [32, 33]. Chemically deposited films on mica in a surfactant-free aqueous solution gave a thickness of 150 nm or more while those using AP gave a film 50 nm thick; in both cases the films were continuous. A very large amount of pyrrole in solution was not adsorbed at the surface at the start of polymerization, so that a significant amount of polymerization occurred in the bulk solution. Further, diffusion of monomer to the surface during polymerization probably caused thickening of the film. This study did show, however, that the surfactant template restricted the growth of the film on the substrate in the vertical direction.

In using admicellar polymerization, an opportunity exists to make the films even thinner than usual for high surface-area powder samples [28, 34]. With flat surfaces, the amount of monomer in solution relative to the amount solubilized in the adsorbed surfactant layer is extremely large. One way to reduce diffusion from the bulk would be to limit the concentration of pyrrole in the adsorbing solution; however this method also substantially reduces the initial polymerization rate because the concentration of monomer in the admicelles is much lower. Increasing the solid/liquid ratio, the normal solution to this diffusion problem, is practically impossible to apply in this case because of the limited surface area of a flat surface. A unique way to limit the amount of pyrrole in the reacting solution is to saturate the admicelles, then quickly remove the solid from the adsolubilizing solution and polymerize in a second solution. This procedure assumes that the surfactant and monomer do not quickly desorb, an assumption that is true in practice. Further, because pyrrole will polymerize in the bulk solution without any solid present (even though the concentration of the surfactant is below the

CMC), separating the two solutions means that oligomer or polymer formed in solution cannot deposit on the surface. Results using this approach are reported here.

3.2 Experimental

3.2.1 Materials

Pyrrole (Aldrich, 98%) was purified by passing it through an activated alumina column multiple times before use. Sodium dodecyl sulfate (SDS, Aldrich, 98%) and cetyltrimethyl ammonium bromide (CTAB, Aldrich) were used as received. SDS and CTAB served as surfactant templates and made two distinct aqueous systems. A third aqueous system contained pure water only. The oxidant for SDS and water systems, sodium persulfate (SPS, Sigma), and the oxidant for CTAB systems, iron trichloride hexahydrate (ITC, $FeCl_3 \cdot 6H_2O$, Fisher Scientific), were used without further purification. CTAB cannot be used with SPS nor SDS with ITC due to formation of precipitate. The precipitation of surfactant with oxidant might degrade the admicelle template, degrade the oxidant's capability, and affect the film structure. Pure ethanol (EtOH, Aaper Alcohol and Chemical) was used to dilute pyrrole and help increase pyrrole's solubility in aqueous systems. Deionized water was used throughout for rinsing and preparing solutions. Ammonium hydroxide (NH_4OH, Mallinckrodt) and hydrogen peroxide (H_2O_2, EM Science), mixed 50/50 vol%, were used to etch PPy from the substrate.

Two atomically smooth substrates were employed. Muscovite mica (Asheville-Schoonmaker Mica Co., grade 4) was hydrophilic in nature and graphite (HOPG, Digital Instruments, grade ZYH), hydrophobic. Before preparing the sample, graphite was peeled with adhesive tape a few times to expose a clean and flat surface (Fig. 3.1: 1). Mica discs were cleaved by a razor blade to expose a fresh surface (Fig. 3.1: 2). The average roughness was on the order of angstroms so any deposited film can be easily detected by SPM.

Mica is a common aluminosilicate of which the general formula is $KAl_2(AlSi_3O_{10})(OH)_2$ [35, 36]. The isomorphic substitution of Al for Si in $Si_2O_5^{2-}$ groups makes the mica basal plane negatively charged (1 charge/0.48 nm^2) [37,38]. Therefore, in an aqueous solution the mica surface is usually not electrically neutral. Mica consists of lamellar sheets which correspond to a 2:1 or T-O-T (tetrahedron-octahedron-tetrahedron) configuration with K^+ or other cations in between sandwiched layers to balance the negative lattice. It is K^+ that makes mica easy to cleave and easily exchange ions with H^+, Na^+, or cationic surfactant. Each sandwich layer of mica is composed of four anion sheets (mainly -O- and -OH) and three cation ones (mainly Al^{3+}, Si^{4+}). The atomic images obtained by AFM usually give a hexagonal structure (i.e., six-fold) instead of a trigonal one (i.e., three-fold) [39,40]. This occurs because only pairs of tetragonal groups in the T-layer can be resolved, as checked by the lattice parameters of mica. Similarly, atomic images of graphite by AFM also give a hexagonal structure because only overlapped carbons in the top and the next trigonal layers are scanned.

In this work, TappingMode atomic force microscopy (TMAFM) was used to characterize the film morphology and measure film thickness (Digital Instruments, NanoScope III, Multimode SPM). TMAFM has an advantage over contact mode AFM in that the tip exerts a very small amount of vertical force on the sample during scanning but is strong enough to resist the capillary force and other attractive forces from the sample surface. TMAFM also reduces the dragging force of the tip on the sample so as to minimize deformation of the surface structures. Unlike many other techniques, AFM is able to give us a direct measurement of film thickness if a film edge is encountered [33]. Although film thickness measurements may still be affected by the factors listed above, by choosing lamellar substrates one may obtain a highly clean surface with a small roughness to reduce background errors. Moreover, the superior sensitivity of SPM to minute height variations (accurate to 0.1 Å) allows the determination of the film thickness without any modeling.

3.2.2 Thin Film Preparation

To investigate the effect of initial monomer concentration on film thickness, four concentrations of pyrrole were used: 200 mM, 50 mM, 12.5 mM, and 3.13 mM. An appropriate amount of pyrrole was dissolved in 5 ml of ethanol before mixing with surfactant solutions. Ethanol was added to fully dissolve pyrrole in the solution and speed mass transfer of pyrrole to the surface. The effect of ethanol on the polymerizations is not known; however, Yeskie showed that short chain alcohols do not adsolubilize in aqueous systems [30, 41]. To study the effect of surfactant on film morphology, both cationic (CTAB) and anionic (SDS) surfactants were used. CTAB was prepared at a final concentration of 0.7 mM and SDS at 5 mM, both substantially below the respective critical micelle concentration (CMC = 0.95 mM and 8.2 mM in pure water respectively). The pH values for all the systems ranged from 4.9–6.7. 18 samples were prepared in 9 petri dishes in this first step of surfactant adsorption; each dish contained one mica and one graphite sample. Three additional dishes were control samples, two dishes contained surfactant but no pyrrole while the third contained pyrrole at 200 mM but no surfactant. A total of 24 samples were prepared. Surfactant and pyrrole were allowed to aggregate and stabilize on the substrate for one hour. In the meantime, another 9 dishes containing water, surfactant, and oxidant were prepared for the three SDS-SPS, H_2O-SPS, and CTAB-ITC reaction systems. The oxidant concentration was 100 mM to ensure fast oxidation and polymerization. Surfactant at the same concentration was present in the second set of dishes to eliminate changes in the amount of adsorbed surfactant due to a change in bulk surfactant concentration. No ethanol was added to this second set of dishes in order to deter the diffusion of adsolubilized pyrrole out of the admicelles. After placing the samples in the oxidizing solutions for four hours, each sample was withdrawn from solution. In order to remove any unwanted material from the sample, samples were rinsed and then soaked in double deionized water for one hour. Finally the samples were dried at 60 °C for two hours. The 18 samples prepared were denoted as

HR200, HM200, CR200, CM200, SR200, SM200, CR050, CM050, SR050, SM050, CR012, CM012, SR012, SM012, CR003, CM003, SR003, and SM003, where H, C, S represent H_2O, CTAB, and SDS; R, M represent graphite and mica; and 200, 050, 012, 003 represent initial pyrrole concentrations, respectively. The complete symbol list is presented in Table 3.1.

3.2.3 Etching and Wettability Investigation

Each sample was dipped halfway into a freshly prepared solution of NH_4OH/H_2O_2 for 2 minutes to remove some of the PPy thin film from the substrate. After dipping, no change in either the graphite or mica surface was evident in an optical microscope image (800 ×). The samples were then rinsed with deionized water and the wettability of surfaces studied qualitatively by visual examination. An inclined hydrophobic surface would repel water, leaving a dry surface at all times. On the other hand, inclined mica surfaces will retain a layer of water prior to evaporation. From these visual experiments the hydrophobicity of some bare substrates are PTFE (poly(tetrafluoroethylene)) > HOPG > PS (Polystyrene) > Mica.

3.2.4 AFM Characterization of the Film

After checking film wettability, TMAFM was used to scan surface morphology and evaluate film continuity. Roughness analyses were applied to the SPM images to help determine the quality of the films.

Film thickness can be measured by SPM directly when the film edge over the substrate is encountered. If not, pinholes or scratches of the film may make its determination possible, although one must be careful that the bottom is, in fact, the underlying substrate. For thicker films, one can use adhesive tape to remove part of the film from the substrate and thus created a film edge, although if the substrate can be peeled off from the bulk more readily than the film from the surface (i.e., adhesion > cohesion), this measurement will be inaccurate.

For roughness analysis, the root-mean-square roughness (Rq) and the fractal dimension (FD) of the PPy ultrathin films were measured. Rq was defined as the square root of the sum of the squared deviation of data with respect to the mean of data, showing the global roughness of the surface. The fractal dimension is measured by taking the slope of the major straight line in a log-log plot of the measured areas of an imaged surface versus the areas of a cell, an area unit of the surface projection [32, 42–44]. The surface is thus divided into patches based on the cells. For a given surface, a larger cell corresponds to larger but fewer patches, which results in a smaller total surface area due to lost surface details. Normally, the measured surface area will depend on the cell size much more for a rough surface, leading to a larger negative slope and a larger FD.

3.3 Results and Discussion

3.3.1 Wettability of PPy Coated Samples

Substrate wettabilities are listed in Table 3.2. PPy made in our lab in a single adsorbing and reacting solution was found relatively 'hydrophilic' compared with PTFE or even with mica. Accordingly, PPy films prepared at the highest concentrations in SR200, CR200, and HR200 all changed graphite's wettability from hydrophobic into hydrophilic. Here 'hydrophilic' indicates the ability of the sample surface to spread a layer of water without forming droplets. The average film thickness was less when the initial pyrrole concentration was reduced below 200 mM. The thinner films were not totally continuous, so that wettability was still strongly affected by the substrate's hydrophobicity. As a result, low concentration samples remain hydrophobic. In contrast, since mica was originally hydrophilic, there was no simple way to tell if the surface property had changed.

3.3.2 Wettability of Etched Samples

Wettabilities after etching are listed in Table 3.3. Mica samples turned from hydrophilic to hydrophobic after etching. Since the etching solution was found to temporarily turn the bare mica surface hydrophobic, the observed strong hydrophobicity of all the mica samples after etching indicated a substantial portion of the film on mica had been etched away. In contrast, PPy films on HOPG (SR200 and HR200) still remained hydrophilic because the etching time of 2 minutes was too short to remove the relatively thick or dense films. Under an optical microscope, the etched part of the film in HR200 was still colored, but in a lighter shade of brown. The partial etching of the film was also confirmed on another sample by TMAFM (to be shown below). Similar to the mica samples, thinner films formed on HOPG prepared at lower concentrations had sufficient PPy removed to make the surfaces hydrophobic.

3.3.3 Surfactant Adsorption

In order to show that the observed films were not surfactant molecules, a few mica samples containing surfactant only were prepared and examined using SPM. For this study, CTAB and SDS solutions were prepared from the same solutions prepared for thin film deposition, i.e., no micelles were present in solution. Dried surfactant aggregates were prepared on mica in two ways. In the first method a drop of surfactant solution was placed onto mica and the solution was dried in air. In the second method mica was removed from the surfactant solution after admicelle formation.

In the drop method, multiple bilayers were present in CTAB with a repeating layer thickness of $\sim$ 3.2 (3.0–3.5) nm matching the bilayer thickness of CTAB (3.4 nm) [45, 46] (Fig. 3.2: 1). The tops of such multiple bilayers were scanned and pinholes were distributed over the surface (not shown). By section and bearing analyses on SPM images, the depth of the pinholes were found to reach as low as 1.8 nm, i.e. the molecular length of CTAB. The pinholes also suggested poorer aggregation of the admicelle top layer. From the second method, one single bilayer of CTAB was revealed by SPM with pinholes similar to those seen in multilayer samples and a few protruding granules (Fig. 3.2: 2). The section and bearing analyses also showed an average depth of 1.8 nm, which indicated the top layer of the adsorbed single bilayer. It seemed from the image that the single bilayer could span over a large area of the substrate. Of course, the images reproduced here may not be those in the liquid state since the configurations of surfactant may be very different after drying.

The drop method used with SDS produced multiple monolayers with a thickness around 0.5 nm (Fig. 3.2: 3). Crystalline structures were not observed in the regions scanned. The bottom layer in contact with the substrate can be seen through the pinholes of the top layer and is also pinhole-rich. On the other hand, an SDS single monolayer on mica from the second method showed separate patches, which implies poorer adsorption of SDS on mica than CTAB (Fig. 3.2: 4). Section and bearing analyses showed that each layer is at most a monolayer with step heights smaller than the molecular length of SDS, which indicates, due to small rigidness, that SDS layers might be obliquely or horizontally stacked in dry state. The morphologies of CTAB and SDS aggregates shown in SPM images do not in any way resemble those of PPy films. Moreover, after rinsing with water, the bilayers and monolayers were not present. Unlike PPy films that had strong adhesion to the substrate and remained there even after vigorous rinsing and soaking, the surfactant aggregates were water soluble and washable and could not form a tethered self-assembled layer.

3.3.4 Film Morphology

To organize our study of thin film morphology, the samples were divided into two groups based on the substrates used, mica and HOPG. We start our discussion with the samples made at the highest initial concentration of pyrrole. Then we compare the morphologies of those samples made at lower pyrrole concentrations.

HR200: Thick and Thin Films on HOPG with no Surfactant

HR200 was found to have different thicknesses prepared under the same nominal conditions; one, HR200 (thin), is a thin netted film (Fig. 3.3: 1) whose etched surface is also shown (Fig. 3.3: 2) and the other, HR200 (thick), is a thick film with PPy islands densely distributed over it (Fig. 3.3: 3). The formation of both thick and thin films implies poor control of the amount of pyrrole adsorbed on HOPG in the absence of surfactant, which most probably happens during the translation of samples between solutions. Any perturbation to the sample on pulling out and immersion will affect the adsorbed pyrrole. HR200 (thick) is perceptible to the naked eye if compared with clean HOPG. Further, the etched region reveals a different color contrast to the eye and a discernable boundary under an optical microscope. However, HR200 (thin) cannot be distinguished even using optical microscopy. In fact, we did not know film was present until SPM results were available. The thick film indicates that pyrrole was uniformly and directly adsorbed onto to the substrate in a surfactant-free solution due to the strong hydrophobic interaction between HOPG and monomer. When the sample is taken out of the monomer solution and immersed again in the oxidant solution, fast polymerization results in a film with many islands. The substrate became hydrophilic owing to the -(NH)- or -(NH^+)- groups of the film or the dopant oxidant ions. Islands may come from favored reaction sites at which polymerization initiates and seem to spread over the substrate evenly. Islands are about 180 nm in diameter, 30 nm in height, and thus 0.30 in aspect ratio (AR, height/radius, Table 3.4). The aspect ratio is quite high with respect to the aspect ratios found with the surfactant-assisted polymerizations, which suggests that the surfactant is better able to prevent monomer aggregation during adsorption and polymerization. The average film thickness is 80 nm, measured directly across the film edges and pinholes of a HR200 (thick) sample that was partially immersed in the oxidant solution during polymerization as shown in Fig. 3.3: 4. In contrast, HR200 (thin) has a thickness of 3.9 nm, based on a few 'flat-bottom' pinholes found in the film, representing exposed substrate (Table 3.4). After etching for 2 minutes the film was disrupted into patches but with no obvious change in thickness (Fig. 3.3: 2). The AR of islands comprising the network increased, however, from 0.10 to 0.13, indicating lateral etching breaks the linkage of the originally web-like film. The quick exposure of the substrate upon etching for a short period further confirms that the flat-bottom pinholes are at or very close to the substrate, validating the measurement of film thickness. In addition, etched HR200 (thin) has lower values in Rq and FD (based on 2 μm images) than the non-etched one due to exposed substrate and smoothed film (Table 3.4).

Thin Films on HOPG with Surfactant

CR200 and SR200 also show a layer of inter-linked nodules (Fig. 3.4: 1, 2 and Fig. 3.4: 3, 4, respectively). Nodules are features that are islands that are almost, but not quite, flat. The nodules in both samples are of similar size but the islands are larger and more prevalent in CR200. The average thickness of the film for CR200 and SR200 are 2.6 and 2.0 nm respectively; the 'island' ARs are 0.11 and 0.07 respectively and finally the 'nodule' ARs are 0.04 and 0.03 respectively (Table 3.4). As the micrographs suggest and the AR measurements confirm, the morphology of HR200 (thin) is more similar to that of CR200 than that of SR200. Ionic surfactants such as CTAB and SDS have been shown to adsorb to HOPG with the tails contacting the surface, forming half-cylindrical structures [47–52]. Because of this observation, polymerization of pyrrole on HOPG in the presence of surfactant cannot be strictly termed admicellar polymerization because only monolayers form on the surface. The location of the monomer is a substantial question: is the monomer at the interface between the surfactant tails and the graphite surface, or is the monomer localized at the surfactant head groups? This question will be addressed further when discussing the results of the mica study.

PPy films made on HOPG in the presence of CTAB and SDS at different concentrations below 200 mM are full of discrete islands (Fig. 3.5: 1–3 and Fig. 3.5:

4–6, respectively). Seemingly, there is a roughly bimodal distribution of sizes; very large islands are found with much smaller islands. Again, the number of the very large islands is greater in the CTAB case. In addition, from the scratches made during the deposition process or by SPM tips, ultrathin PPy films were found around the islands and nodules (Fig. 3.6: 1), judging from different gray shades of the scratches and their neighborhood. Therefore, a layer of PPy coated the apparently exposed substrate around the islands and nodules. A schematic picture of the PPy film with islands and nodules formed on a substrate is shown in Fig. 3.7.

Films with islands and nodules seem to conform to the Stranski-Krastanov (SK) or island-layer film growth mode [53, 54], although the mechanisms involved are different. The SK model is commonly applied to solid-on-solid type deposition. In our case the deposition step is greatly suppressed with the monomer 'pre-adsorbed' as an oily layer to react with the oxidant from the solution. Polymerization starts at the pyrrole-solution interface and the fronts of the polymerized phase move toward both the solution and the pyrrole-substrate interface as oxidant diffuses into the pyrrole/surfactant aggregates. In contrast, the film which follows the SK model nucleates and grows up from the substrate with monomer and oligomer being added to the film top.

HM200: Discontinuous Film on Mica with no Surfactant

HM200 shows merely discrete PPy islands due to the strong hydrophilicity of mica (Fig. 3.8). Since there was no surfactant in the system of HM200, pyrrole did not 'wet' the substrate well. The discrete islands suggest the formation of pyrrole droplets away from one another when the mica substrate was pulled out of solution, in fact the polymerization may have occurred in the solution and then the polymer was deposited on the surface due to precipitation. Regardless, no film but islands were formed after quick polymerization. The average height of discrete islands is 5.9 nm (Table 3.4) while some islands reach up to 12 nm in height. The high aspect ratio of the islands (0.34) indicates that PPy growth on mica in non-surfactant solution is still preferential to the surface since for perfect radial growth, the aspect ratio would be 1.

Thin Films on Mica with Surfactant

CM samples and SM200 also show an island layer with a nodular film in Fig. 3.9 and Fig. 3.10: 1, respectively. Although SM samples at lower pyrrole concentrations do not show clear images (not shown) because of tip contamination and degradation during SPM scanning, good images of films on mica prepared at 20 mM pyrrole (SM020) in the presence of SDS have been obtained (Fig. 3.10: 2–3). These two images are from different samples and hence reflect somewhat on the reproducibility of this procedure. Preliminary work shows that SM020 conducts electricity under low humidity conditions. If films are electrically conducting, then the PPy films have good connectivity since bare mica will not conduct after being dried. In addition, films scratched by AFM tips reveal a square region either with smoothed islands (TMAFM, Fig. 3.6: 2) or with PPy lumps pushed aside and residues left inside (contact mode AFM, Fig. 3.6: 3). The average thicknesses for CM200 and SM200 are 2.9 and 1.3 nm, respectively (Table 3.4). The island ARs are 0.05 and 0.07 respectively, which are lower than that of HM200 (0.34), indicating better lateral growth of PPy. The nodule ARs are both 0.02.

The films in Fig. 3.9: 2, 4 and Fig. 3.10: 2, 3 appear much different than those in Fig. 3.9: 1, 3 and Fig. 3.10: 1. The latter micrographs somewhat resemble those on HOPG, however the former are completely unlike anything seen in HOPG. The nodules are smaller, the number density of the nodules is much higher, and the number density of islands also is much smaller. We believe the most likely possibility is that the number of initiation points is smaller in the films produced on HOPG and the films represented by Fig. 3.9: 1, 3 and Fig. 3.10: 1, leading to larger islands and nodules. Since the oxidant concentration is constant, the most likely possibility is that the amount of pyrrole remaining on the surface after removing the mica from the adsorbing solution was higher in the latter case. Supporting this possibility is that higher concentrations of pyrrole showed larger islands and nodules, while lower concentrations did not, although admittedly the polymerization represented by Fig. 3.9: 3 was done using a low monomer concentration as well.

CTAB normally forms either bilayers or cylindrical structures [55–58] by replacing the exchangeable cations on mica at the intercalary sites or by direct adsorption to SiO_2 tetrahedra due to the negative lattice frame. With a high degree of confidence, one can assert that pyrrole is not going to localize at the head groups of both an anionic and cationic surfactant. Since the morphologies are substantially different between mica and graphite at low monomer concentrations but similar for the two surfactants, it is logical to assume that the location of the monomer is different for mica and graphite, but the same for SDS and CTAB. Hence, the most likely location of the monomer is between the surfactant and the surface for the graphite and within the bilayer for the mica. If this reasoning is correct, then the polymerizations on the mica surface do truly represent what is termed an admicellar polymerization. This reasoning depends primarily on the appearance of micrographs, and since the morphology is not totally consistent (as well as our procedures not being totally reproducible for certain conditions), this conclusion should not be regarded as definitive.

Since mica is negatively charged at pH 4.0–6.0, SDS is not supposed to form a well-organized bilayer in SM samples, but less patchy islands are formed after the polymerization than in HM200. The morphology of films made with SDS at low monomer concentrations appears very similar to that of films produced with CTAB. The mechanism by which a better film is formed with SDS versus no surfactant is not clear. One possibility is that anionic SDS may be adsorbed to mica at the intercalary sites associated with cationic ions. The intercalary sites are the centers of hexagonal rings formed by SiO_2 tetrahedra. Since the spacing between intercalary sites is larger than that of hydroxyl sites on silica or alumina, an SDS bilayer would be very incomplete. Since the surfactant concentration was below the CMC, surfactant coverage had probably not reached its maximum value for any of the surfaces; however, the fractional coverage was not quantified in this study.

CR200 and CM200 have larger Rq than SR200 and SM200, indicating films made with CTAB are rougher than films made with SDS. On the contrary, films made with CTAB have smaller FD than films made with SDS, because SR200 and SM200 have an average lower island density than CR200 and CM200 and resemble a lacunal surface morphology better. HM200 has the smallest FD due to the largely exposed mica and a middle Rq contributed by the discrete islands.

3.4 Conclusions

Admicellar polymerization was used to create thin films of poly(pyrrole) on the surface of hydrophobic pyrolitic graphite and freshly cleaved mica. Separate adsorbing and reacting solutions were used to eliminate diffusion of monomer from the bulk solution to the reacting surface, as well as to prevent solution polymerization. Film thicknesses via this method were approximately an order of magnitude smaller than those where the two solutions were identical. For the hydrophobic substrate, the differences between films formed with and without surfactant were minor; although films made with sodium dodecyl sulfate did have smaller aspect ratios, which indicates that the growth rate in the plane of the substrate versus that vertical to the substrate was larger in these systems. The general morphology of these films was islands connected with small nodules in a web-like pattern; the number density of the islands and nodules depended on the surfactant type and monomer concentration. Differences were much more pronounced in the case of the hydrophilic substrate; without surfactant only very discrete islands of poly(pyrrole) were seen. For one of the two concentrations of SDS and for two of the four concentrations with CTAB, the morphology was very similar to that for the hydrophobic substrate. Morphologies of the films for the other concentrations were much different, no web-like pattern was evident and no large islands were present. The differences in the CTAB results are not understood at present; most likely the cause is poor reproducibility of transfer between the adsorbing and reacting solutions.

Bibliography

[1] Hutchins, R. S.; Bachas, L. G. *Anal. Chem.* **1995,** *67,* 1654–1660.

[2] Shiu, K. K.; Chan, O. Y.; Pang, S. W. *Anal. Chem.* **1995,** *67,* 2828–2834.

[3] Yamato, H.; Ohwa, M.; Wernet, W. *Anal. Chem.* **1995,** *67,* 2776–2780.

[4] Wong, J. Y.; Langer, R.; Ingber, D. E. *Proc. Natl. Acad. Sci. U. S. A.* **1994,** *91,* 3201-3204.

[5] Momma, T.; Nishimura, K.; Osaka, T. *J. Electrochem. Soc.* **1994,** *141,* 2326.

[6] Bruschi, P.; Cacialli, F.; A., N.; B., N. *J. Appl. Phys.* **1994,** *76,* 3640–3644.

[7] Gorman, C. B.; Biebuyck, H. A.; Whitesides, G. M. *Chem. Mater.* **1995,** *7,* 526.

[8] Decher, G.; Hong, J. D.; Schmitt, J. *Thin Solid Films* **1992,** *210/211,* 831–835.

[9] Shimazaki, Y.; Mitsuishi, M.; Ito, S.; Yamamoto, M. *Langmuir* **1997,** *13,* 1385–1387.

[10] Berlot, I.; Labbé, P.; Moutet, J.-C. *Langmuir* **2000,** *16,* 5814–5819.

[11] Shimoda, S.; Smela, E. *Electrochim. Acta* **1998,** *44,* 219–238.

[12] Barr, G. E.; Sayre, C. N.; Connor, D. M.; Collard, D. M. *Langmuir* **1996,** *12,* 1395–1398.

[13] Kaplin, D. A.; Qutubuddin, S. *Polymer* **1993,** *36,* 1275-1286.

[14] Sasano, K.; Nakamura, K.; Kaneto, K. *Jpn. J. Appl. Phys. Part 2* **1993,** *32,* L863.

[15] Hong, X.; Tyson, J. C.; Middlecoff, J. S.; Collard, D. M. *Macromolecules* **1999,** *32,* 4232–4239.

[16] Shen, Y.; Wan, M. *J. Polym. Sci.: Part A: Polym. Chem.* **1999,** *37,* 1443–1449.

[17] Chu, X.; Chan, V.; Schmidt, L. D.; Smyrl, W. H. *J. Appl. Phys.* **1995,** *77,* 6658–6663.

[18] Chen, X.; Devaux, J.; Issi, J.; Billaud, D. *Polym. Eng. Sci.* **1995,** *35,* 642–647.

[19] Sayre, C. N.; Collard, D. M. *Langmuir* **1997,** *13,* 714–722.

[20] Hsueh, C. C.; Brajter-Toth, A. *Anal. Chem.* **1994,** *66,* 2458-2464.

[21] Nishizawa, M.; Miwa, Y.; Matsue, T.; Uchida, I. *J. Electroanal. Chem.* **1994,** *371,* 273-275.

[22] Nishizawa, M.; Miwa, Y.; Matsue, T.; Uchida, I. *J. Electrochem. Soc.* **1993,** *140,* 1650.

[23] Nishizawa, M.; Shibuya, M.; Sawaguchi, T.; Matsue, T.; Uchida, I. *J. Phys. Chem.* **1991,** *95,* 9042-9044.

[24] Pigois-Landureau, E.; Nicolau, Y. F.; Delamar, M. *Synth. Met.* **1995,** *72,* 111-119.

[25] Bsiesy, A.; Nicolau, Y. F.; Ermolieff, A.; Muller, F.; Gaspard, F. *Thin Solid Films* **1995,** *255,* 43–48.

[26] Nicolau, Y. F.; Davied, S.; Genoud, F.; Nechtschein, M.; Travers, J. P. *Synth. Met.* **1991,** *41–43,* 1491–1494.

[27] Nicolau, Y. F.; Davied, S.; Nechtschein, M. Layer-by-Layer Chemical Deposition of Conducting Polymer Thin Films. In *Science and Applications of Conducting Polymers*; Salaneck, W. R.; Clark, D. T.; Samuelsen, E. J., Eds.; IOP Publishing Ltd: Bristol, 1991.

[28] Wu, J.; Harwell, J. H.; O'Rear, E. A. *Langmuir* **1987,** *3,* 531–537.

[29] Lai, C. L.; Harwell, J. H.; O'Rear, E. A. *Langmuir* **1995,** *11,* 905–911.

[30] Funkhouser, G. P.; Arévalo, M. P.; Glatzhofer, D. T.; O'Rear, E. A. *Langmuir* **1995,** *11,* 1443–1447.

[31] O'Haver, J. H.; Harwell, J. H.; O'Rear, E. A. *Langmuir* **1994,** *10,* 2588–2593.

[32] Yuan, W.-L.; Cho, G.; O'Rear, E. A.; Glatzhofer, D. T. *Thin Solid Films* **2001,** *385,* 96–108.

[33] Cho, G. *Bull. Chem. Soc. Jpn.* **1997,** *70,* 2309–2316.

[34] Wu, J.; Harwell, J. H.; O'Rear, E. A.; Christian, S. D. *AIChE Journal* **1988,** *34,* 1511–1518.

[35] Lima-de-Faria, J. *Structural Mineralogy : An Introduction;* Kluwer Academic Publishers: Dordrecht, the Netherlands, 1994.

[36] Griffen, D. T. *Silicate Crystal Chemistry;* Oxford University Press, Inc.: New York, 1992.

[37] Tilton, R. D.; Blomberg, E.; Claesson, P. M. *Langmuir* **1993,** *9,* 2102–2108.

[38] Narkiewicz-Michalek, J. *Langmuir* **1992,** *8,* 7–13.

[39] Lin, F.; Meier, D. J. *Langmuir* **1994,** *10,* 1660–1662.

[40] Tang, H.; Joachim, C.; Devillers, J. *J. Vac. Sci. Technol. B.* **1994,** *12,* 2179–2183.

[41] Yeskie, M. A. *Various Aspects of Surfactant Aggregates Adsorbed on an Oxide Surface : The Hemimicelle/Admicelle Transition, and the Interaction of Alcohols and Alkanes,* Ph.D. Dissertation, University of Oklahoma, 1988

[42] Adamson, A. W. *Physical Chemistry of Surfaces;* John Wiley & Sons, Inc.: New York, 5th ed.; 1990.

[43] Digital Instruments, Santa Barbara, CA "NanoScope Command Reference Manual", 1997.

[44] Russ, J. C. *The Image Processing Handbook;* CRC Press, LLC: Boca Raton, Florida, 3rd ed.; 1999.

[45] Eriksson, L. G. T.; Claesson, P. M.; Eriksson, J. C.; Yaminsky, V. V. *J. Colloid Interface Sci.* **1996,** *181,* 476–489.

[46] Chen, Y. L.; Helm, C. A.; Lsraelachvili, J. N. *Langmuir* **1991,** *7,* 2694–2699.

[47] Manne, S.; Cleveland, J. P.; Gaub, H. E.; Stucky, G. D.; Hansma, P. K. *Langmuir* **1994,** *10,* 4409–4413.

[48] Manne, S.; Gaub, H. E. *SCIENCE* **1995,** *270,* 1480–1482.

[49] Sokolov, I.; Yang, H.; A.Ozin, G.; Henderson, G. S. *Advanced Materials* **1997,** *9,* 917–921.

[50] Király, Z.; Findenegg, G. H. *J. Phys. Chem.* **1998,** *102,* 1203–1211.

[51] Wanless, E. J.; Davey, T. W.; Ducker, W. A. *Langmuir* **1997,** *13,* 4223-4228.

[52] Wanless, E. J.; Ducker, W. A. *J. Phys. Chem.* **1996,** *100,* 3207–3214.

[53] Stokes, R. J.; Evans, D. F. *Fundamentals of Interfacial Engineering;* Advances in Interfacial Engineering Series Wiley-VCH, Inc.: New York, 1997.

[54] Staikov, G. *Nanoscale Probes of the Solid/Liquid Interface;* volume 288 of *NATO ASI Series E: Applied Science* Kluwer Academic Publishers: Dordrecht, the Netherlands, 1995.

[55] Liu, J.-F.; Ducker, W. A. *J. Phys. Chem. B* **1999,** *103,* 8558-8567.

[56] Ducker, W. A.; Wanless, E. J. *Langmuir* **1999,** *15,* 160-168.

[57] Patrick, H. N.; Warr, G. G.; Manne, S.; Aksay, I. A. *Langmuir* **1999,** *15,* 1685-1692.

[58] Lamont, R. E.; Ducker, W. A. *J. Am. Chem. Soc.* **1998,** *120,* 7602-7607.

Symbol	*Meaning*	*Symbol*	*Meaning*	*Symbol*	*Meaning*
R	Graphite	**C**	CTAB	**050**	50.0 mM
M	Mica	**S**	SDS	**012**	12.5 mM
H	Water	**200**	200 mM	**003**	3.13 mM

Table 3.1: Symbols used in PPy sample names

	S		C		H	
mM	**M**	**R**	**M**	**R**	**M**	**R**
200. (**200**)	HI	HI	HI	PHI	HI	HI
50.0 (**050**)	HI	PHI	HI	HO		
12.5 (**012**)	HI	HO	HI	HO		
3.13 (**003**)	HI	HO	HI	HO		
HI: Hydrophilic, HO: Hydrophobic, PHI: Partially Hydrophilic						

Table 3.2: Visual determination of relative wettability of PPy coated samples before etching.

	S		C		H	
mM	**M**	**R**	**M**	**R**	**M**	**R**
200. (**200**)	HO	HI	HO	HO	HO	HI
50.0 (**050**)	HO	HO	HO	HO		
12.5 (**012**)	HO	HO	HO	HO		
3.13 (**003**)	HO	HO	HO	HO		
HI: Hydrophilic, HO: Hydrophobic						

Table 3.3: Visual determination of relative wettability of PPy coated samples after etching.

	H				C				S			
	M200	R200 (Thick)	R200 (Thin)	R200 (Etched)	M200		R200		M200		R200	
nm or none	Island	Island	Island	Island	Island	Nodule	Island	Nodule	Island	Nodule	Island	Nodule
Thickness	5.9± 3.5	80± 30	3.9± 1.1	3.9± 0.4	2.9± 2.4		2.6± 0.7		1.3± 0.3		2.0± 0.5	
AR	0.34± 0.20	0.30± 0.14	0.10± 0.04	0.13± 0.05	0.05± 0.03	0.02± 0.01	0.11± 0.05	0.04± 0.02	0.07± 0.02	0.02± 0.01	0.07± 0.03	0.03± 0.02
Rq	0.8± 0.0		1.2± 0.0	1.1± 0.2	1.1± 0.2		1.7± 0.7		0.3± 0.0		0.5± 0.0	
FD	2.1± 0.0		2.3± 0.0	2.1± 0.0	2.2± 0.1		2.2± 0.1		2.3± 0.0		2.4± 0.0	
AR: Island/Nodule Aspect Ratio, Rq: Root-Mean-Square Roughness, FD: Fractal Dimension												

Table 3.4: PPy film parameters

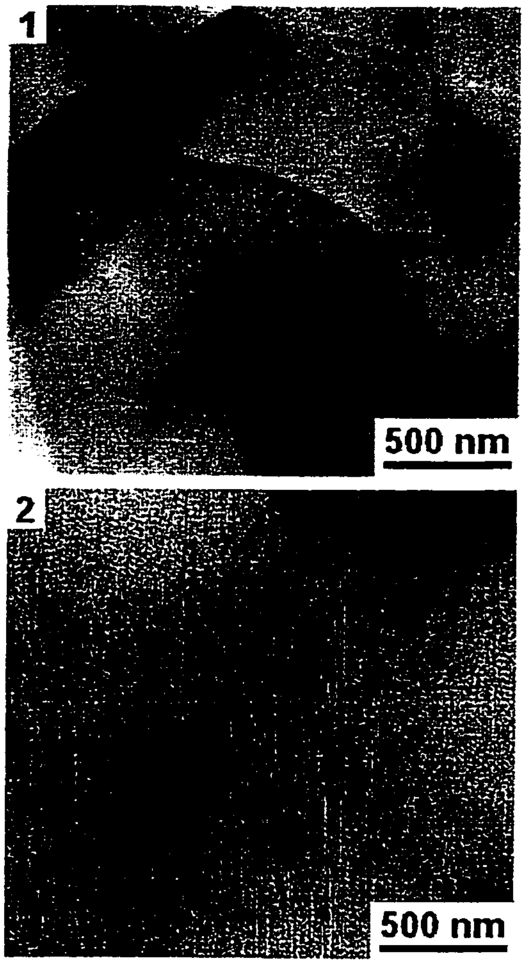

Figure 3.1: Bare substrates. (1) Bare HOPG; (2) bare mica.

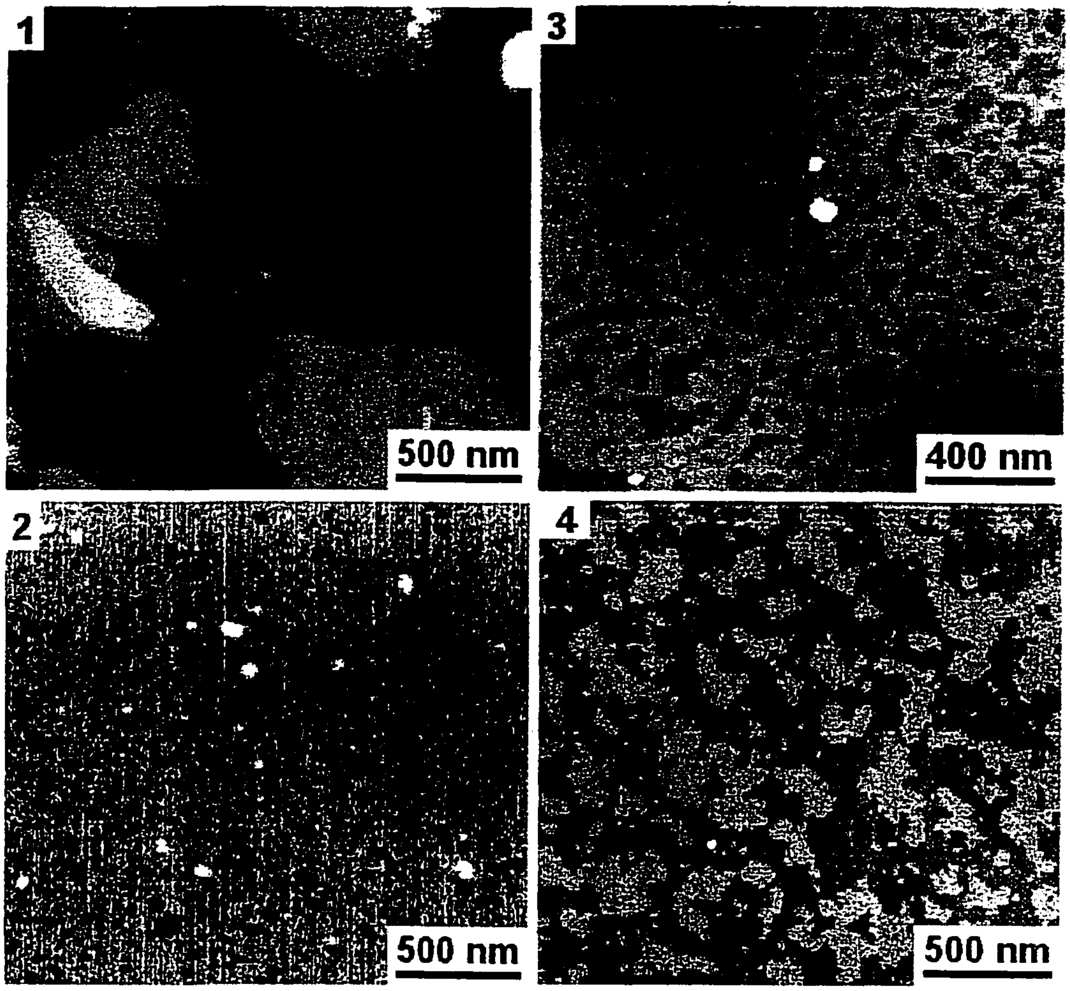

Figure 3.2: Surfactants on mica. (1) Multiple CTAB bilayers; (2) single CTAB bilayer; (3) SDS multiple monolayer; (4) SDS single monolayer.

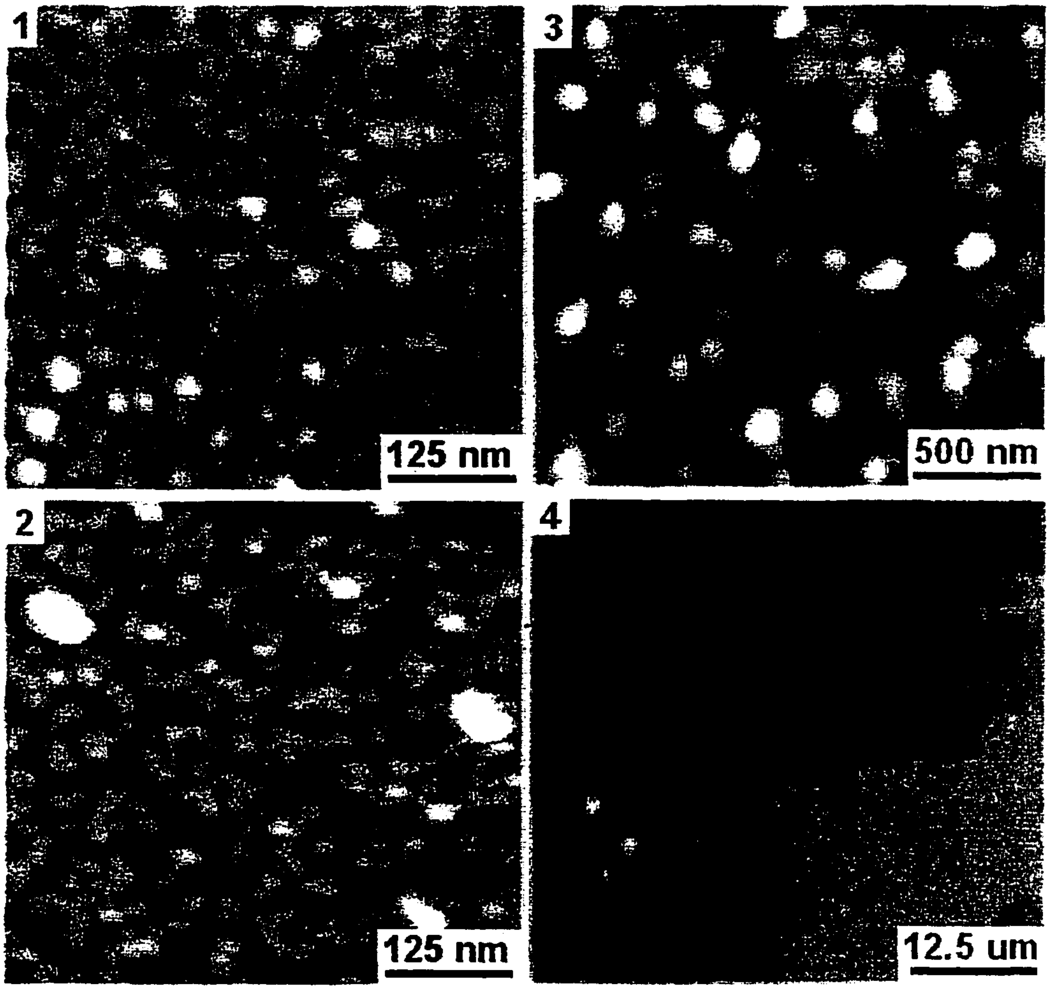

Figure 3.3: PPy films formed on HOPG in the absence of surfactant. Either thin or thick films may be deposited. The initial pyrrole concentration is 200 mM. (1) HR200 (thin); (2) etched HR200 (thin); (3) HR200 (thick) (4) film edges of HR200 (thick).

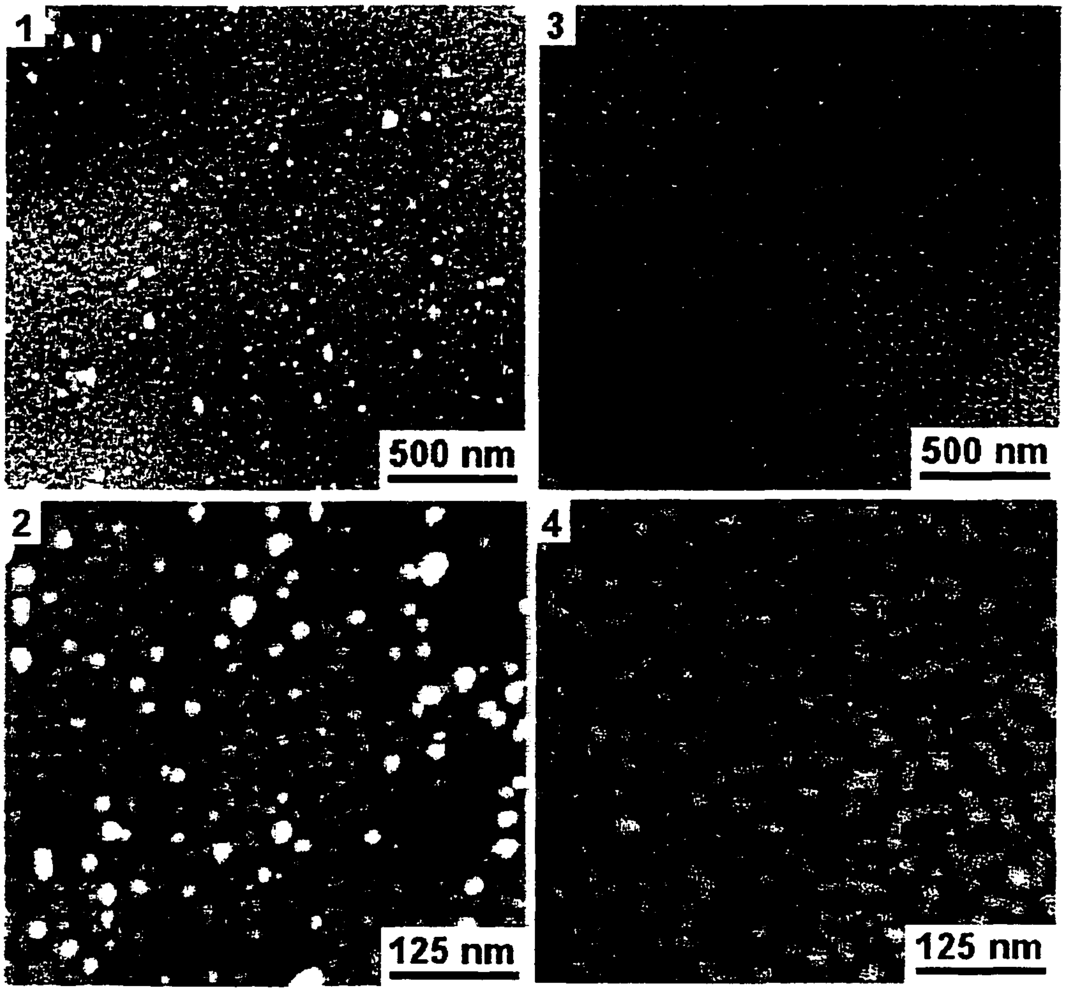

Figure 3.4: PPy films formed on HOPG in the presence of CTAB or SDS. Well connected layers of PPy islands are observed. The initial pyrrole concentration is 200 mM. (1) and (2) CR200; (3) and (4) SR200.

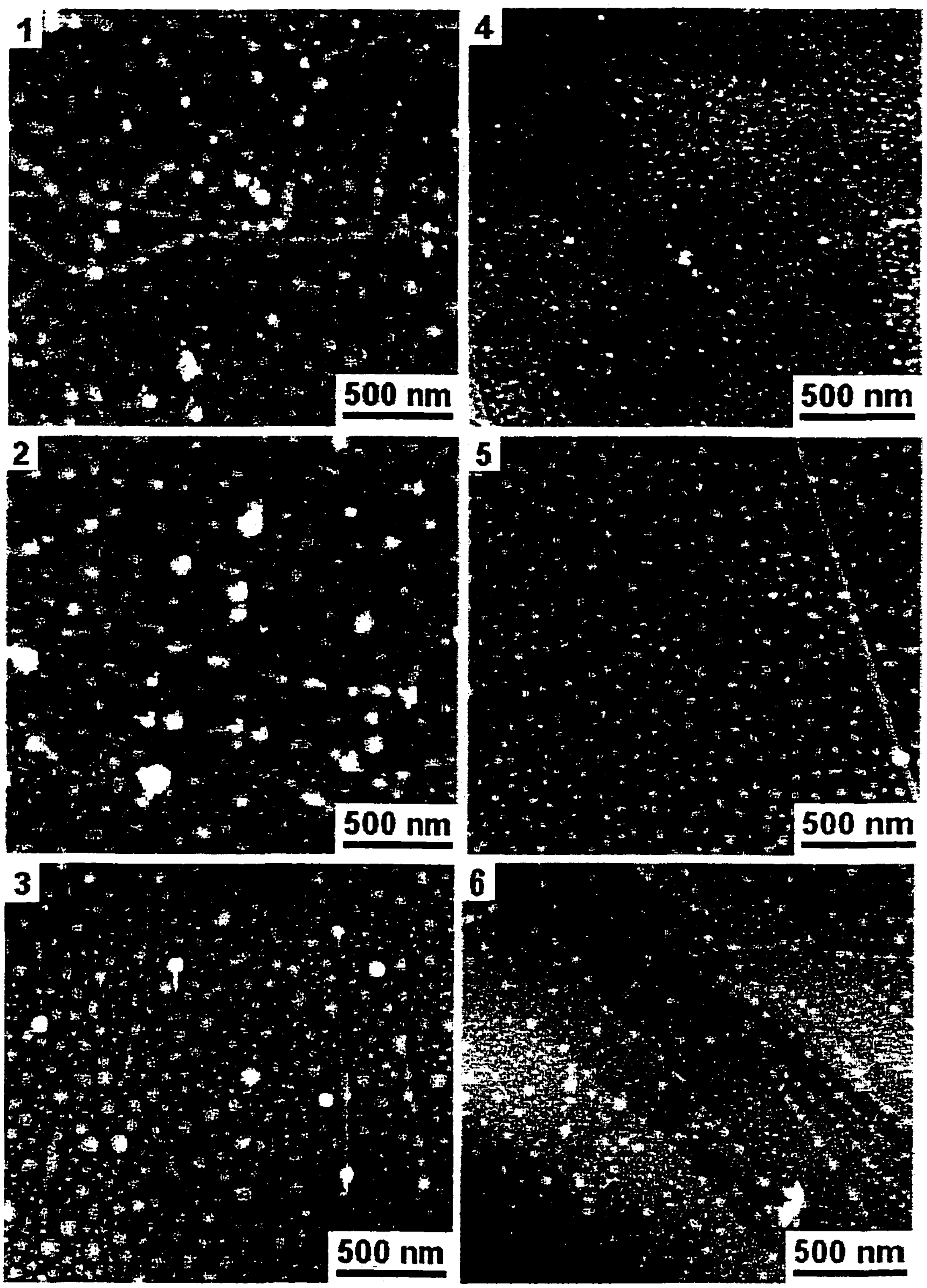

Figure 3.5: PPy formed on HOPG in the presence of CTAB or SDS at lower initial pyrrole concentrations. Discontinuous islands with a layer of fine nodules are observed. The island density increases with initial concentration. (1) CR050; (2) CR012; (3) CR003; (4) SR050; (5) SR012; (6) SR003.

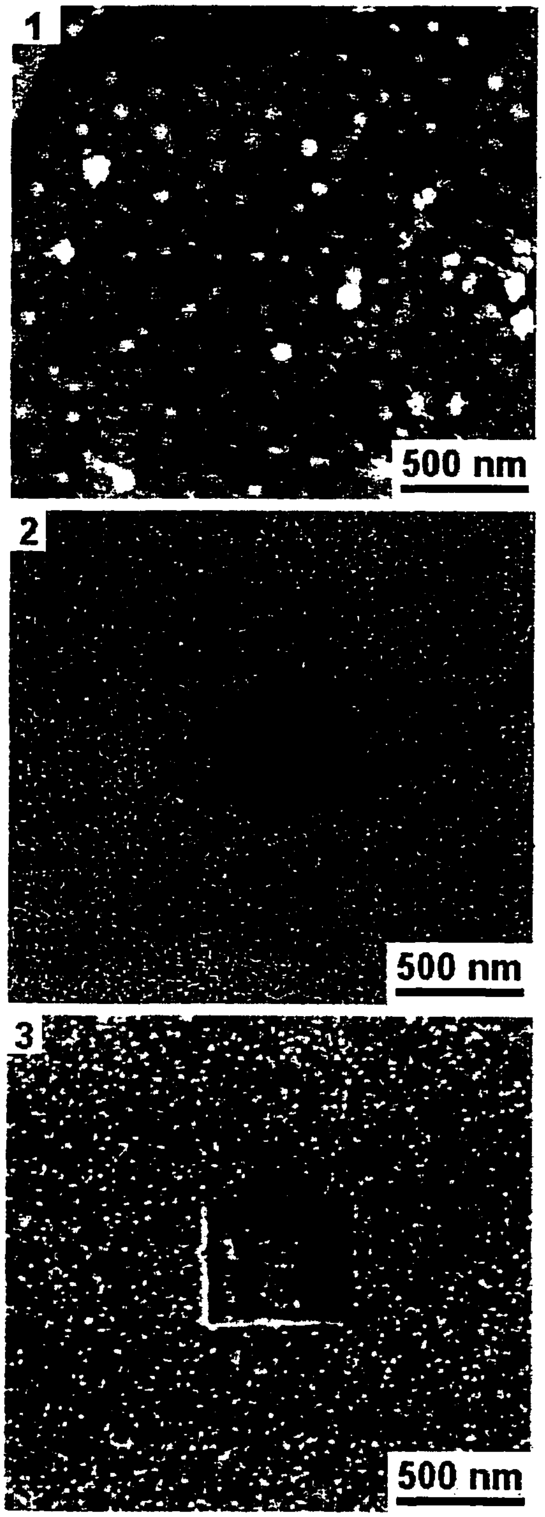

Figure 3.6: Scratched PPy films by AFM tips. PPy ultrathin film, smoothed film, and pushed aside polymer are observed respectively. (1) CR012; (2) SR200; (3) SM200.

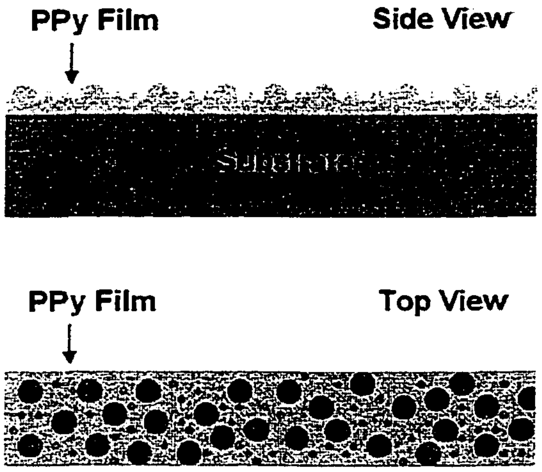

Figure 3.7: A schematic of the PPy film formed on a substrate with islands and nodules.

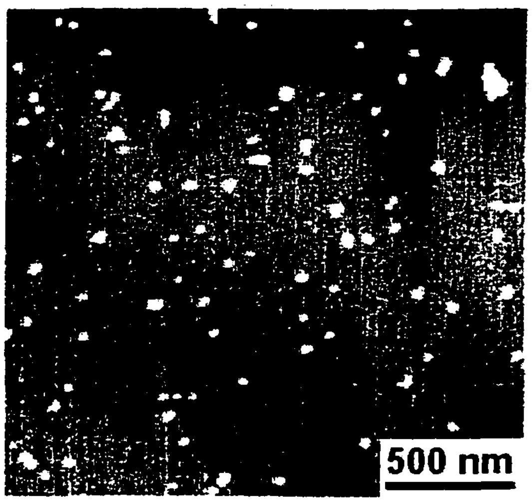

Figure 3.8: PPy formed on mica in the absence of surfactant. Only discrete islands are observed. The initial pyrrole concentration is 200 mM.

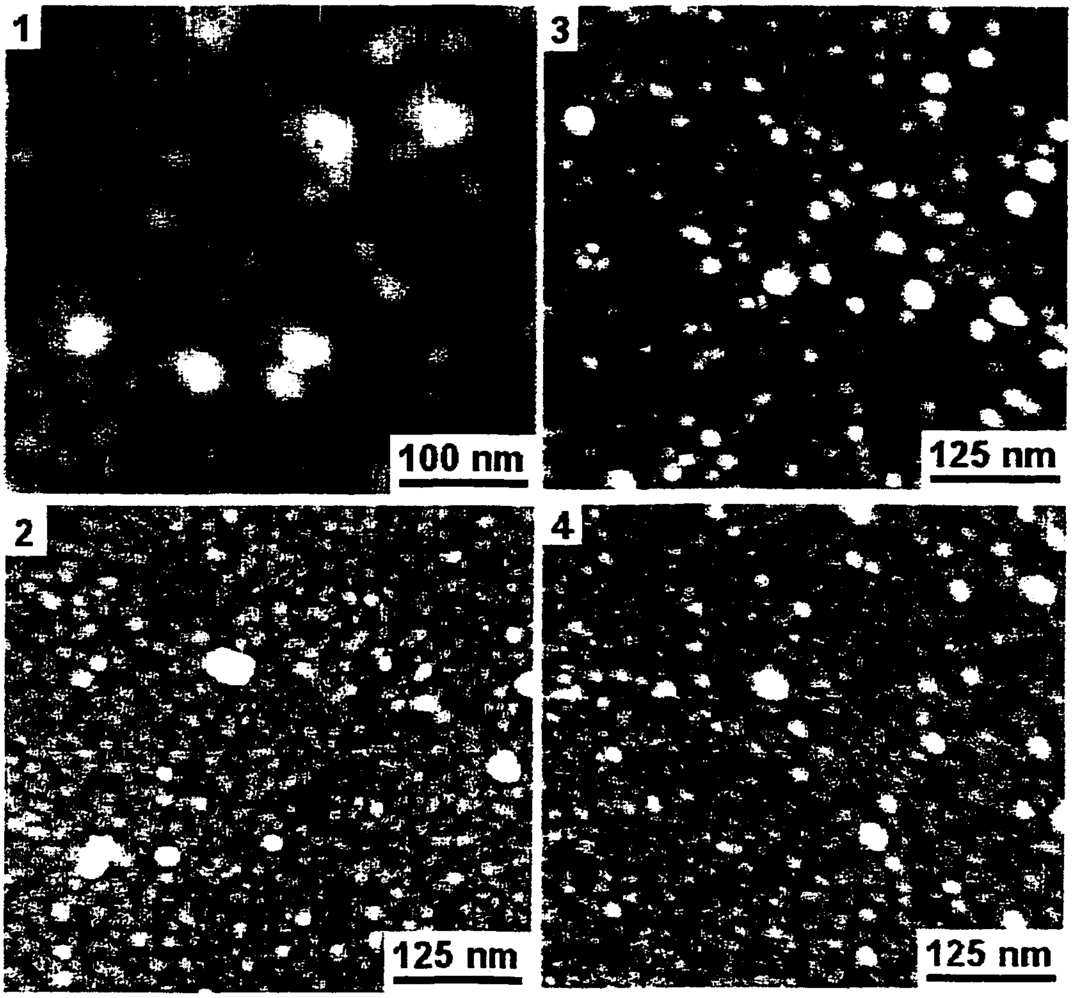

Figure 3.9: PPy films formed on mica in the presence of CTAB at different initial pyrrole concentrations. Islands and nodules are observed at nearly all concentrations. (1) CM200; (2) CM050; (3) CM012; (4) CM003.

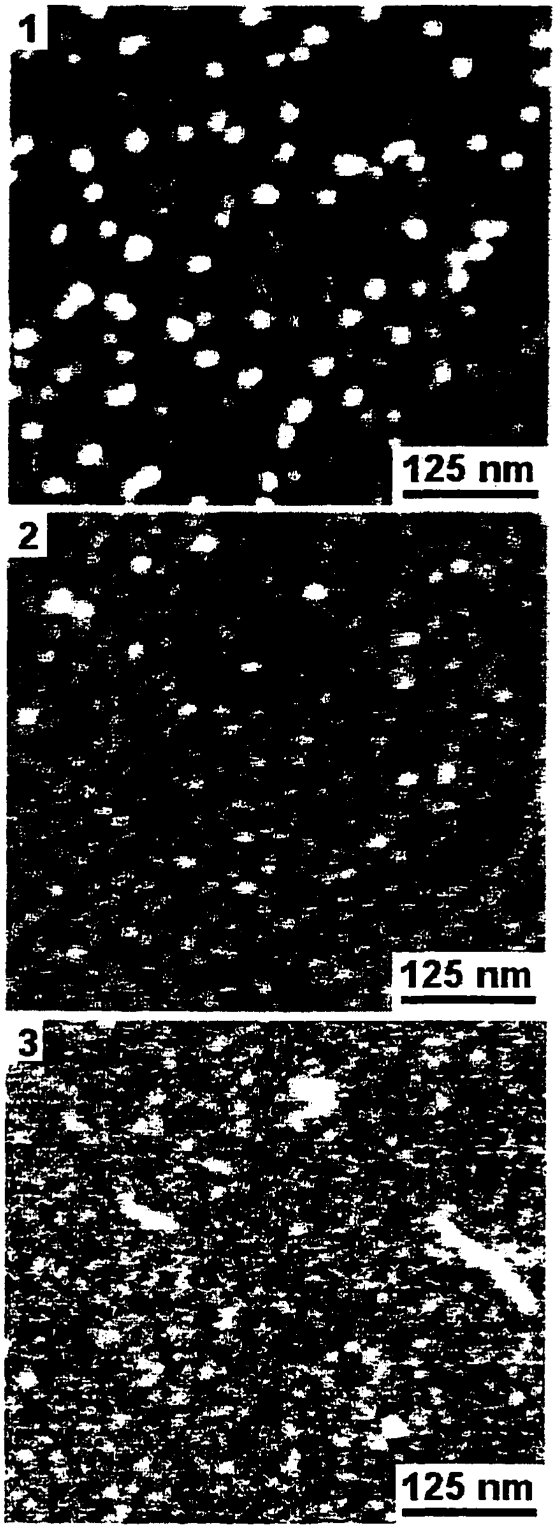

Figure 3.10: PPy films formed on mica in the presence of SDS at different initial pyrrole concentrations. Islands and nodules are observed in the images. (1) SM200 (200 mM pyrrole); (2) SM020-a (20 mM pyrrole); (3) SM020-b (20 mM pyrrole).

Chapter 4

Volume Change Upon Solidification*

4.1 Solidification of InSb

The volume change of solidification is a fundamental thermodynamic property of practical and theoretical interests. In casting and metals processing, for example, volume shrinkage may cause cavities so as to reduce product quality. To find the volume change during phase transition usually involves measuring the specific volume or density at temperatures surrounding the melting point. Common methods of determining the volume change of solidification require either the handling of significant amounts of the molten metal/alloy or the use of specially designed apparatus [1, 2]. In this letter, we describe the fortuitous discovery of a prospective nanogram scale alternative experimental approach made possible with scanning probe technology.

---

*W.L. Yuan, W.K. Liu, E.A. O'Rear, and M.B. Santos, Nanogram Scale Determination of the Volume Change of Solidification of an Indium-rich Alloy by AFM, Journal of Materials Science Letters 17 (1998) 943-946

There are three stages of volume shrinking upon cooling: liquid-state contraction, solidification, and solid-state contraction. With different techniques, one can by experiment construct a plot of specific volume vs. temperature to ascertain the phase transformation component. An important property, the volume change upon melting aids in determining the slope of the coexistence line in phase space through the Clausius-Clapeyron equation

$$\frac{dP}{dT} = \frac{\Delta H}{T \Delta V}$$

where dP/dT is the slope of pressure with transition temperature, ΔH is the enthalpy change (latent heat), and ΔV is the molar volume change due to phase transition [3].

The sample investigated in this work arose from over-annealing during an experiment on the thermal desorption of native oxides from the InSb (001) surface. These oxides can be removed by heating the sample slowly to about 450 °C in an ultrahigh vacuum and under an Sb overpressure. If the temperature is too high, however, Sb atoms will be desorbed and an excess of In atoms will remain on the surface. After cooling, the sample displayed solidified droplets with diameters on the order of 10 microns, observed by metallograph (Fig. 4.1: top) and verified by atomic force microscopy in height mode (Fig. 4.1: bottom). Data from the Energy Dispersive Analysis of X-rays technique indicated that these droplets were composed primarily of In with at most 16% Sb. The mechanism of forming droplets is probably the joint effect of substrate roughness serving as nucleation sites and the contribution of interfacial tension due to the compositional shift of the surface layer from the sublayers, which is similar to that for the formation of quantum dots. In an AFM surface plot, we discovered a distinct nick(s) in each droplet (Fig. 4.2) which we interpreted as the residual volume change from passage of a solidification front(s) through the droplet. This hypothesis was tested by determining the percent volume change, $(V_{liquid}-V_{solid})/V_{solid} \cdot 100$, for a series of 20 semi-spheroidal droplets and comparing the average to values from the literature. The AFM is ideal for this purpose since it maps out the surface topography in the height mode. Droplet volumes were found from numerical double integration (Simpson's rule with end correction) on computer of the experimental pixel 'height' data of the AFM (Nanoscope III, Digital Instruments, Inc.) for the actual surface (Fig. 4.3: top). A similar calculation was done for the 'repaired' spheroidal surface, completed by polynomial interpolation of the height data with the nick region excluded (Fig. 4.3: bottom). The value found for the volume change of solidification of the indium-rich alloy is 2.2 which compares favorably with the reference value of 2.5% for pure indium [4]. Since pure antimony contracts during solidification by an average of 0.23% [2], a linear mixing model using our experimental result and the reference values for the pure components yields an estimate of composition as 87% indium, in reasonable accord with the X-ray chemical analysis. Nicks observed on each droplet are of different size and in different azimuthal and meridional positions which indicated they were not affected by vertical orientation of the substrate during deposition. A small number of nucleation sites seems essential with the number and location of the nicks reflecting the number and position of nucleation sites within the droplet. Clear indentations thus formed as a result of the molecular motion toward the solidification fronts caused by internal shrinkage associated with the phase change. Larger inclined droplets in other over-annealed samples came from coalescence of small droplets, clearly evident by a 'trail' from movement (Fig. 4.4). That indentations were not observed on the large droplets suggests that quiescence, substrate temperature, and rate of cooling are critical to sample preparation for determination of the volume change of solidification. We believe circulation in these larger droplets led to multiple nucleation sites and an affine contraction. As a result, no nicks were observed.

In this study, AFM provides a novel nano-scale technique for measuring the thermodynamic property of volume change upon solidification. Solidified, indented indium-rich droplets on a flat substrate were examined and their average ratio of volume change was found to be 2.2% which compared well with the literature value for pure indium of 2.5%.

Details about how to recover the nicks using interpolation and how to calculate the volume of the droplet can be found in Appendices G and H.

Bibliography

[1] B. W. Rossiter and R. C. Baetzold. in "Physical Methods of Chemistry, volume VI" (John Wiley & Sons, Inc., New York, 2nd. edition, 1992) p.79.

[2] M. Rittich. *NASA TM-77817* (1985).

[3] R. C. Dorf. in "The Engineering Handbook" (CRC, Boca Raton, Florida, 1995) p.496.

[4] J. I. Kroschwitz and M. Howe-Grant. in "Encyclopedia of Chemical Technology" (John Wiley & Sons, New York, 4th edition, 1995) p.156.

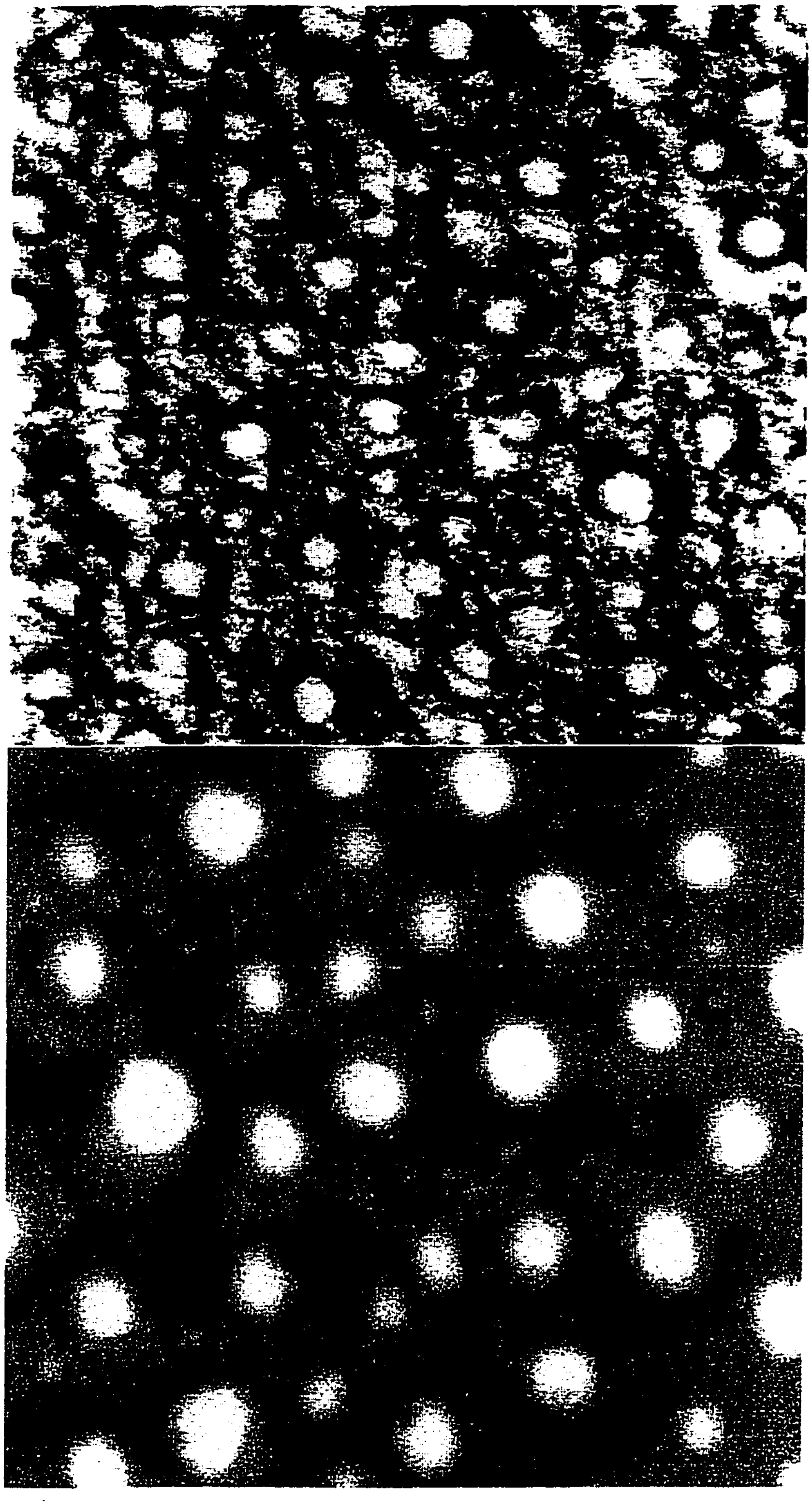

Figure 4.1: (a) Optical image of InSb/InSb (001) surface. Size: 70 × 70 μm^2. (b) AFM height image of InSb/InSb (001) surface. Size: 70 × 70 μm^2.

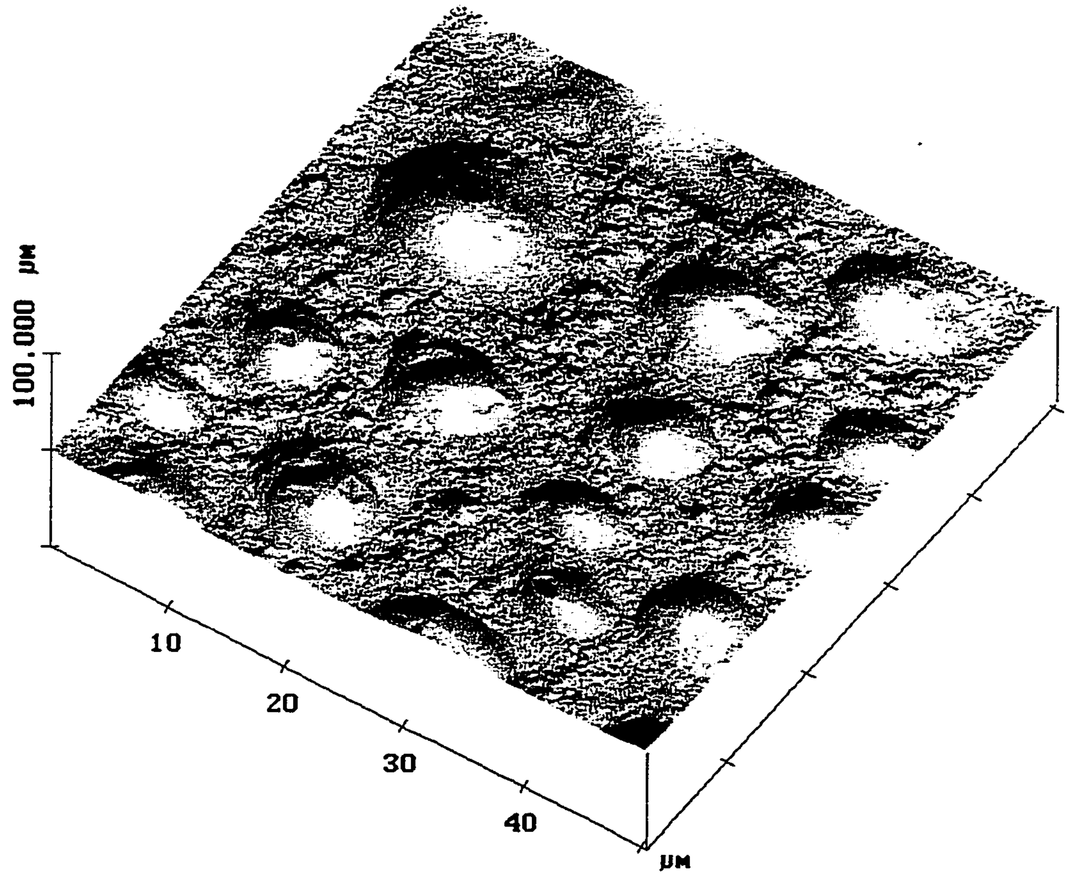

Figure 4.2: AFM surface plot of solidified droplets of InSb on InSb (001) substrate. Note the nick(s) were observed on the droplets. Size: 50 × 50 μm^2.

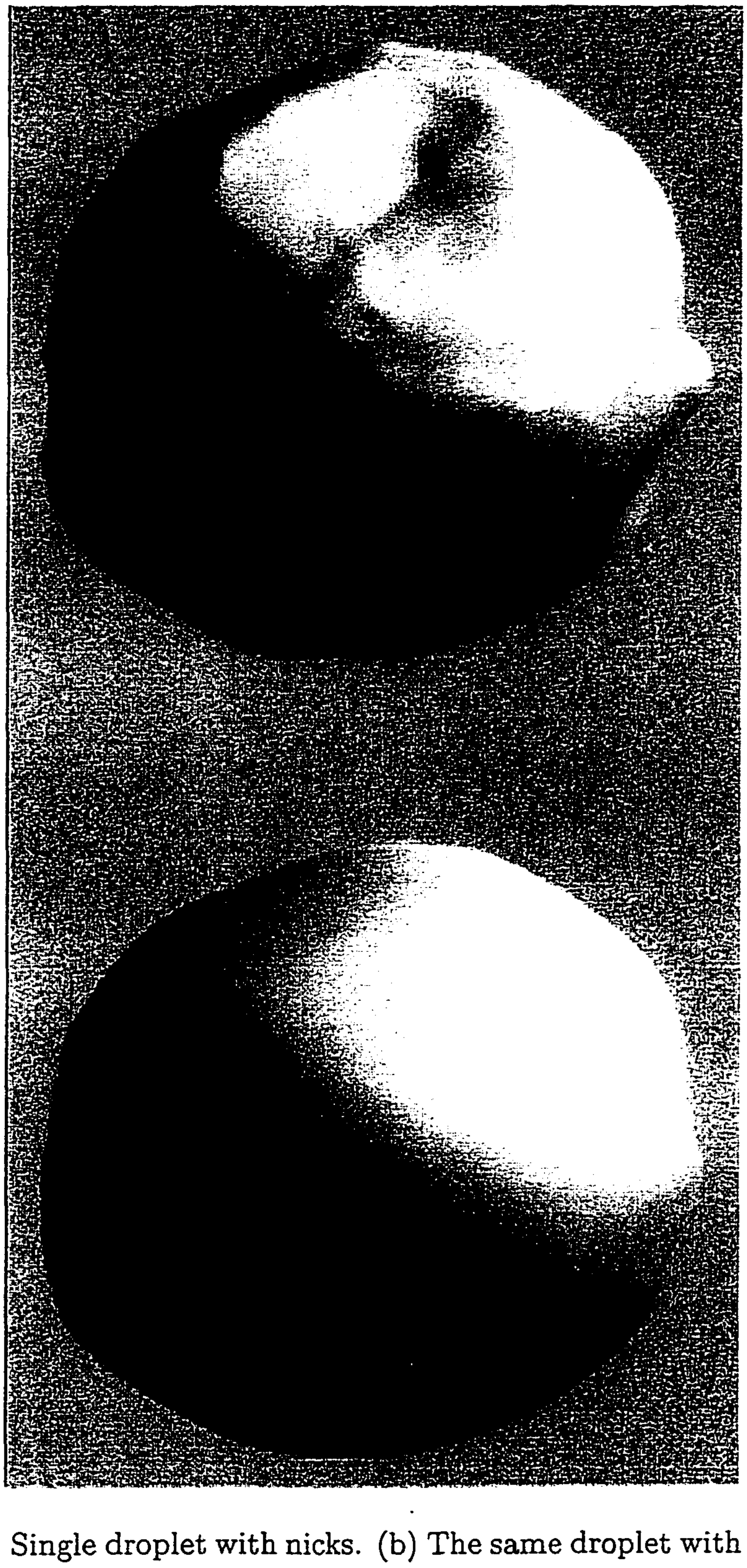

Figure 4.3: (a) Single droplet with nicks. (b) The same droplet with nicks repaired by computer.

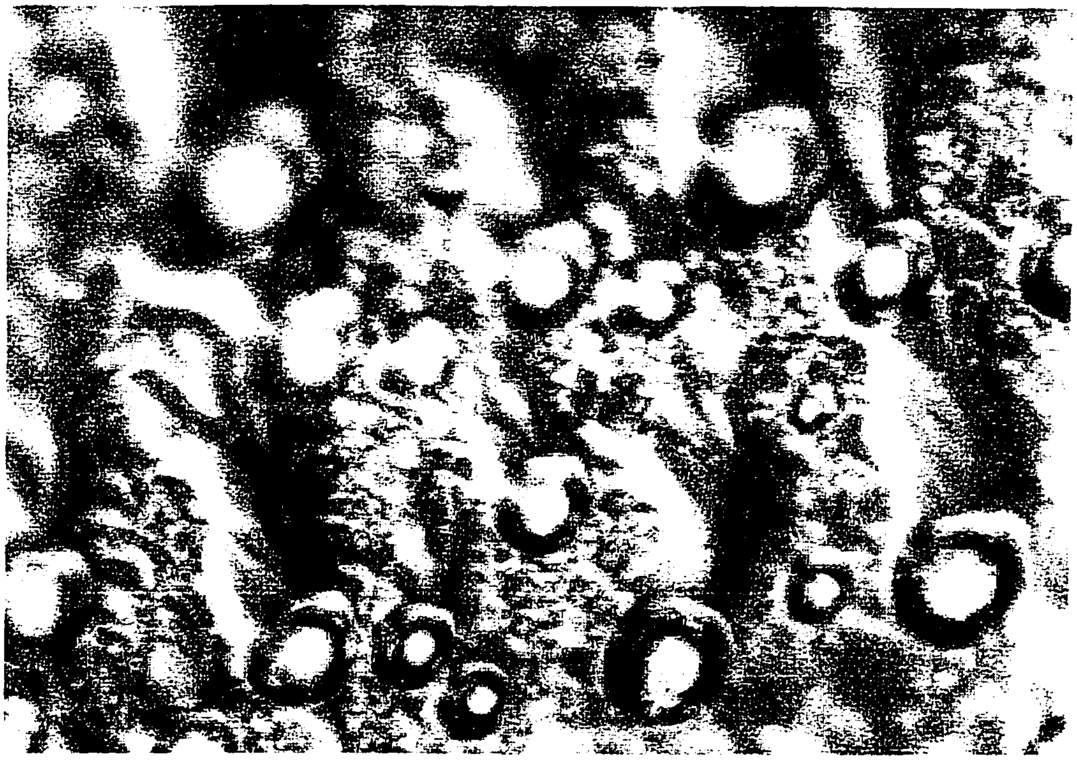

Figure 4.4: Large droplets with trails. Size: 250 × 190 μm^2.

Chapter 5

Annealed CaF_2 Thin Films*

In order to form a continuous thin layer of CaF_2 on Si(100), effects of annealing on rectangular single crystals of CaF_2 with polycrystals deposited using MBE were studied. Morphological evolution and film parameters were investigated and analyzed by AFM. After rapid thermal annealing, crystals were flattened on the tops and amorphous clusters appeared. Polycrystals were not suppressed by annealing but rather promoted the formation of amorphous CaF_2. Loss of film material after annealing was also observed based on the volume change calculated using AFM.

5.1 Introduction

5.1.1 CaF_2 Thin Films and MBE.

CaF_2 is an insulating material that can be used in microelectronic device fabrication. Recently, Si based materials with CaF_2 layers were found to show opto-electronic properties [1,2]. CaF_2 films are normally deposited by molecular beam epitaxy (MBE) [3,4]. The morphology of CaF_2 thin films is of either triangular or rectangular 'islands', depending on the crystalline orientation of the substrate.

---

*Wei-Li Yuan, Edgar A. O'Rear, T. Chatterjee, Patrick J. McCann, W. K. Liu, X. M. Fang, M. B. Santos, Characterization of Annealed CaF_2 Thin Films On Si(100) by Atomic Force Microscopy, to be submitted for publication

5.1.2 Film Annealing and AFM Analysis.

Annealing is a common approach to reshape and toughen material. It helps build high quality solid films grown by MBE (i.e., films that are thin, smooth, continuous, and free of defects). Also, annealing is used to transform amorphous silicon (a-Si) into polycrystalline silicon (poly-Si) in the manufacturing of high speed semiconductor transistors. Examination of film structures by scanning electron microscopy (SEM) or transmission electron microscopy (TEM) generally gives limited information of morphology. SEM and TEM images are 2D micrographs mapped from 3D surfaces. Much 3D information is lost and can only be restored with difficulty by observing 2D photos.

Atomic force microscopy (AFM), in contrast, generates 3D images by recording a set of line profiles over the sample surface. This offers an important metrological capability for semiconductor materials characterization. An AFM image can be saved as a computer file comprising an array of height data (z) captured according to a grid of points in a reference xy-plane and the surface can be represented by $z = z(x, y) = z_{i,j}$. Through image processing, one can obtain information about film thickness, surface roughness, grain size, and volume enclosed under the surface. In addition to AFM, its related techniques such as friction force microscopy (LFM) and scanning tunneling microscopy (STM) are also being widely used in characterizing semiconductor films [5–8]. In this report, we exploited the analytical power of AFM to understand the effects of *ex situ* rapid thermal annealing

(RTA) on CaF_2 films deposited on Si(100).

5.2 Experimental

5.2.1 Preparation of CaF_2 Thin Films

CaF_2 was deposited on Si(100) at a substrate temperature of 580 °C by MBE [9]. The sample mass gives an equivalent film thickness of 200 Å. After deposition, the MBE films were scanned using AFM under ambient conditions and then submitted to RTA. Samples were stored in a plastic box and handled with tweezers. Before AFM and RTA operations, samples were cleaned by Dust-Off pressurized gas (Falcon Safety Products).

5.2.2 Rapid Thermal Annealing (RTA)

RTA was operated for 30 seconds at 700 °C in ambient N_2 (1 atm) for 4 cycles with a 30-second gap in between (Heatpulse 410, AG Associates). Samples were scanned by AFM again to compare the morphologies before and after annealing.

5.2.3 AFM Equipment and Analysis

AFM work was done using a NanoScope III Multimode AFM (Digital Instruments) at a constant force between probe and sample. Several different probes were used, including ESP etched silicon probes (Digital) and ULTRASHARP silicon tips (Silicon-MDT), both with a half-cone angle as sharp as 10 ° to ensure the scanned images were free of tip artifacts. Images were then analyzed by software supplied with the AFM. Several film parameters were calculated to characterize CaF_2 films on crystal dimensions and film roughness. In addition, grain size analysis was also performed to examine the change of polycrystal size and height with annealing.

Section Analysis

Section analysis can be applied to the film image to determine the crystal width, height, and side angle. Since the Si substrate is smooth and partially exposed, the average height obtained is a measure of film thickness and is called in this study the 'section thickness'.

Bearing Analysis

The bearing analysis gives a height histogram of the image. The volume under the surface above a particular height level can be calculated and is called the bearing volume. The bearing volume with respect to the lowest point of the image is designated the total volume in this study. If we divide the total volume by the image area, an average height is calculated as the 'bearing thickness'.

In addition, for a film with exposed substrate, two peaks that represent the most probable heights will be observed in the height histogram. Namely, one peak refers to the substrate height and the other, the film height. The height difference of the two peaks is called the 'two-peak thickness'. The volume enclosed between these two heights is called the 'two-peak volume'.

Roughness Analysis

One parameter to express the surface irregularity is called the 'excess surface area' (Rs). Rs, also called surface area difference or roughness factor, is the normalization of surface area excess with respect to the image area as defined in Eq. 5.1 [10–12]

$$\mathrm{Rs} = \frac{|Surface\ Area - Image\ Area|}{Image\ Area} \times 100\%. \tag{5.1}$$

For a substrate with deposits, Rs depends on height, width (size), and spacing of the distributed features and is able to reveal the short-range roughness of a surface.

Another parameter, the root-mean-square roughness (Rq), is mathematically equivalent to the square root of the total power of the image based on a fast Fourier transform (FFT) algorithm [10] and is by statistics called the standard deviation with respect to the surface mean. Rq best describes the long-range surface roughness and is defined in Eq. 5.2 as

$$\mathrm{Rq} = \sqrt{\frac{\int\int (z - \bar{z})^2\, dx\, dy}{\int\int\, dx\, dy}}, \tag{5.2}$$

where $\bar{z}$ is the mean of z for the whole surface and expressed as

$$\bar{z} = \frac{\int\int\, z(x,y)\, dx\, dy}{\int\int\, dx\, dy}. \tag{5.3}$$

Rq is also called the interface width in the realm of thin film growth [13].

5.3 Results and Discussion

5.3.1 MBE Films of CaF_2

Morphologies

The AFM images of CaF_2 thin film on Si(100) after MBE deposition are shown in Fig. 5.1. In the large sized image (top) three features are observed, the polycrystals (polycrystalline CaF_2 shown as bright spots), pinholes (dark spots), and a film maze. Polycrystals may come from the substrate defects or from lack of ideal growth parameters introduced during deposition, which promote multiple CaF_2 nucleation.

Pinholes are observed associated with polycrystals or stand alone. They are not artifacts induced by AFM tip or image processing because they are not all located to the right (or left) of polycrystals. Since MBE is theoretically modeled by a so called DDA scheme which includes deposition, (surface) diffusion, and aggregation [13], formation of pinholes is a result of surface diffusion and aggregation of CaF_2 molecules due to interception by polycrystals, lack of nucleation sites, long diffusion lengths, and insufficient growth time.

The CaF_2 film, though discontinuous, has a high coverage on the substrate with an apparently uniform thickness. The higher magnification image of the film (bottom) reveals a network of extended rectangular islands with long grooves, inverted pyramidal pits, and pyramids at the ends. An elongated island resembles a 'hut' similar to the structures reported for Ge clusters on Si(001) [14]. Therefore, we will use the term 'crystal huts' to refer to those (grooved) rectangular islands in the following text. The huts can be either in contact with or very close to the neighboring polycrystals.

Hut Side Angle and Orientation

The MBE film of CaF_2 deposited on Si(100) showed (111) facets, which can be inferred from the reference (110) plane of the notched wafer edge. By marking the direction of (110) plane on our sample, after scanning the orientation of crystal huts (Fig. 5.1: bottom) was found to take the [110] directions. Therefore, the facets of crystal hut were determined to be (111) planes according to crystallography and minimization of surface energy.

In addition, the facet angle of the crystal huts with respect to the substrate can be measured directly from AFM images (Fig. 5.2). Cross-section analysis of CaF_2 crystals yielded an angle of $55.8^\circ \pm 4.3^\circ$ (Table 5.1), agreeing well with the theoretical $\sim 54.7^\circ$ of a (111) plane.

5.3.2 Annealed Films of CaF_2

Annealing promoted the formation of flattened crystal huts and amorphous CaF_2 clusters small in height (Fig. 5.3). The amorphous structures appeared in the neighborhood of polycrystals and covered up the pinholes. The polycrystals, considered as defects formed in the film deposition process, seemed to promote the formation of amorphous structures. Amorphous structures might come from thinner crystal huts which changed to flattened huts upon annealing and then to spherical clusters with smoother boundaries which further minimize the surface energy.

Hut Width and Section Thickness

The average width of the crystal huts increased from 49.4 nm to 61.6 nm after annealing, indicating the movement and wetting of CaF_2 on the substrate (Table 5.1). The section thickness of the crystal huts decreased from 26.5 nm to 15.8 nm, indicating the spreading and possible evaporation of CaF_2. The pyramidal peaks of the huts disappeared and flat tops representing the (100) plane appeared (Fig. 5.3: bottom). The replacement of the original low energy (111) facets by the (100) planes indicates a tendency of the surface structure to match the substrate lattice at an elevated temperature. The increased total surface energy may be compensated by wetting the otherwise more energetic substrate surface. It is possible for those flattened and spreading huts to reach one another and render a stable (100) surface with the hut sides eliminated totally. In addition, inverted pyramidal pits and long grooves in the crystal huts were also found to be covered after annealing. The merging and disappearance of the (111) facets of those features decreased the total surface area of the crystal huts as indicated by the change in Rs (Table 5.1), which may lower the total surface energy and favor the surface transformation.

Amorphous clusters were also found interspersed with the flattened huts (Fig. 5.3: bottom), indicating a delayed or uneven annealing rates compared with the polycrystal neighborhoods (Fig. 5.3: top). Since amorphous clusters covered pinholes and the empty regions between the crystal huts, they might result from the sublimation of CaF_2, in addition to direct transformation or surface diffusion of the flattened huts. That is, sublimed material from the huts landed on the exposed substrate and nucleated to form amorphous clusters. In consequence, after annealing, pinholes and crystal huts mostly disappeared, taken over by amorphous structures and flattened huts.

Two-Peak Thickness and Volume

In addition to the section thickness measured using the cross-sectional analysis capability of the SPM software, bearing analysis was also applied to the CaF_2 film images. The height histogram of SPM image pixels shows two prominent peaks (Fig. 5.4). The bottom peak refers to the silicon substrate and the top one to the CaF_2 film. The difference between these two peaks gives an estimate of the average film thickness. The MBE film gives a value of 20.6 nm (Table 5.1) which is basically the same as the aforementioned equivalent film thickness. The annealed sample gives a smaller value of 13.1 nm, indicating the spreading or loss of material.

From the bearing analysis, the volume of CaF_2 enclosed between the two peaks was also calculated. After annealing, the volume decreased from 305.1 nm^3 to

103.3 nm^3, indicating a loss of volume due to evaporation. After annealing, the top peak in the histogram moved down while the bottom one moved up undesirably due to the contribution of amorphous layer. Therefore, the two-peak thickness and volume for the annealed sample both gave smaller values due to a raised bottom peak, resulting in a change of two-peak volume larger than that of total volume which is to be discussed below.

Total Volume and Bearing Thickness

The total volume measured with respect to the lowest point of the image using the bearing analysis was also measured and shown to decrease after annealing (Table 5.1). The lost material, however, ($\sim$ 150 nm^3) is very small compared to the image area and attributed to evaporated CaF_2 molecules with a small amount of desorbed F atoms [15]. Sublimation may introduce a compositional change of the crystal surface which promotes the formation of amorphous structures due to minimization of surface energy. Other impurities such as oxygen may also react with the crystal and change the surface composition and conformation.

The bearing thickness derived from the total volume based on an area of 5 μm × 5 μm decreased from 22.2 to 16.2 nm after annealing, also indicating the flattening of the film. The bearing thickness is mathematically the same as the average height of the image (i.e., $\bar{z}$) and agrees well with the equivalent film thickness (20 nm).

Although the three kinds of thickness gave different values, each is meaningful based on its definition. The section thickness is usually used to represent individual heights of huts. Since the film is non-wetting, it is reasonable to have a section thickness larger than the equivalent film thickness. The two-peak and bearing thicknesses are both similar to the equivalent one for the MBE films but the former is not as accurate as the latter for the annealed films.

Rs and Rq

The flattening, spreading, and merging of CaF_2 islands changed the film morphology and its roughness. The decrease of Rs after annealing from 21.0% to 7.4% (Table 5.1) indicates local structural change of the crystals from sharp tops to flat ones with the elimination of pyramids, grooves, and pits. In contrast, the decrease in Rq from 11.0 to 6.6 nm indicates a long-range morphology change from flattened huts to amorphous clusters. In calculation, amorphous clusters falsely raised the substrate level and further decreased the value of Rq.

Grain Size and Maximum Height of Polycrystals

In order to see any possible change in the polycrystals before and after annealing, their average grain size and maximum grain height were measured (Table 5.1). The grain size is measured using the 'grain analysis' function of the SPM software by averaging the base areas of the first 100 largest grains found in the image (Fig. 5.5). However, we did not see substantial changes. One reason may be the grain boundaries inside the polycrystals have higher resistance against structural change upon annealing. The other reason may be the imaging artifacts such as the leftward trailing tails associated with the polycrystals masked the dimensional change.

The maximum height of polycrystals of the annealed films is slightly larger than that of the MBE films, which may imply a small increase in size due to addition of sublimed CaF_2 from the single crystals. However, the size change of polycrystals needs to be confirmed in the future by better resolved SPM images.

5.4 Conclusion

CaF_2 deposited on Si(100) using MBE forms a discontinuous film composed of hut-like crystals with pinholes and polycrystals. After rapid thermal annealing, the crystal huts flattened and spread on the substrate. Amorphous clusters appeared after annealing at a faster rate around the polycrystals and covered the pinholes. The mechanisms of forming amorphous clusters were discussed based on energy minimization and included surface transformation, diffusion, and sublimation of CaF_2. In order to build a thin and continuous film, rapid thermal annealing was shown to increase the coverage of deposited CaF_2 on the substrate, but finding the optimal annealing parameters such as temperature and time remains a task to be done. Further, avoiding the formation of polycrystals in the MBE process was deemed important to suppress the formation of undesired amorphous clusters in the annealing process.

Bibliography

[1] Watanabe, M.; Maruyama, T.; Ikeda, S. *Journal of Luminescence* **1999,** *80,* 253–256.

[2] Degoli, E.; Ossicini, S. *Journal of Luminescence* **1999,** *80,* 411–415.

[3] Liu, W. K.; Fang, X. M.; Yuan, W. L.; Santos, M. B.; Chatterjee, T.; McCann, P. J.; O'Rear, E. A. *Journal of Crystal Growth* **1996,** *167,* 111–121.

[4] Kim, B. M.; Ventrice, Jr., C. A.; Mercer, T.; Overney, R.; Schowalter, L. J. *Applied Surface Science* **1996,** *104/105,* 409–416.

[5] Viernow, J.; Petrovykh, D. Y.; Men, F. K.; Kirakosian, A.; Lin, J.-L.; Himpsel, F. J. *Applied Physics Letters* **1999,** *74,* 2125–2127.

[6] Petrovykh, D. Y.; Viernow, J.; Lin, M. J.-L.; Leibsle, F. M.; Men, F. K.; Kirakosian, A.; Himpsel, F. J. *J. Vac. Sci. Technol.* **1999,** *17,* 1415–1419.

[7] Klust, A.; Pietsch, H.; Wollschläger, J. *Applied Physics Letters* **1998,** *73,* 1967–1969.

[8] Sumiya, T.; Miura, T.; Fujinuma, H.; Tanaka, S. *Surface Science* **1997,** *376,* 192–204.

[9] Fang, X. M.; McCann, P. J.; Liu, W. K. *Thin Solid Films* **1996,** *272,* 87–92.

[10] Digital Instruments, Santa Barbara, CA "NanoScope Command Reference Manual", 1997.

[11] Yuan, W.-L.; Cho, G.; O'Rear, E. A.; Glatzhofer, D. T. *Thin Solid Films* **2001,** *385,* 96–108.

[12] Silk, T.; Hong, Q.; Tamm, J.; Compton, R. G. *Synth. Met.* **1998,** *93,* 65–71.

[13] Barabási, A. L.; Stanley, H. E. *Fractal Concepts in Surface Growth;* Cambridge University Press: Cambridge, Great Britain, 1995.

[14] Mo, Y. W.; Savage, D. E.; Swartzentruber, B. S.; Lagally, M. G. *Phys. Rev. Lett.* **1990,** *65*, 1020–1023.

[15] Wollschläger, J.; Pietsch, H.; Kayser, R.; Klust, A. *Thin Solid Films* **1998,** *336*, 120–123.

Film Parameters	MBE Films	Annealed Films
Hut Side Angle (°)	55.8±4.3	
Hut Width (nm)	49.4±10.5	61.6±12.8
Section Thickness (nm)	26.5±3.5	15.8±3.1
Two-Peak Thickness (nm)	20.6±0	13.1±0.7
Two-Peak Volume (nm^3)	305.1±16.0	103.3±0.7
Total Volume (nm^3)	555.2±38.0	403.9±39.0
Bearing Thickness (nm)	22.2±1.5	16.2±1.6
Rs (%)	21.0±5.9	7.4±2.7
Rq (nm)	11.0±0.1	6.6±0.1
Grain Size/10^3 (nm^3)	4.4±0.9	4.4±1.4
Max. Grain Height (nm)	172.0±22.2	180.2±14.3

Table 5.1: CaF_2 film parameters before/after rapid thermal annealing

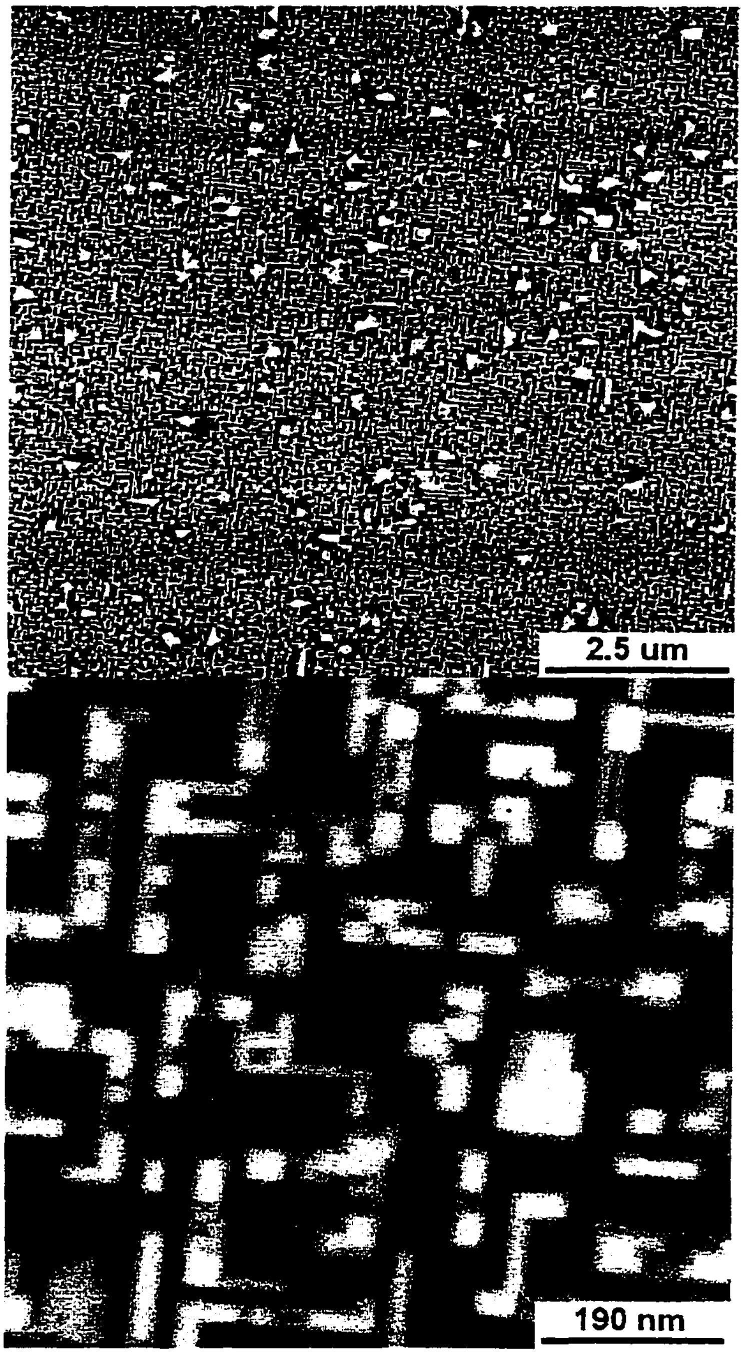

Figure 5.1: SPM images of MBE films of CaF_2. (Top) 10 μm × 10 μm. Single crystals, polycrystals, and pinholes are observed. (Bottom) 760 nm × 760 nm. Detailed single crystal structures such as pyramids, pyramidal pits, and elongated hut-like crystals are observed and mixed together.

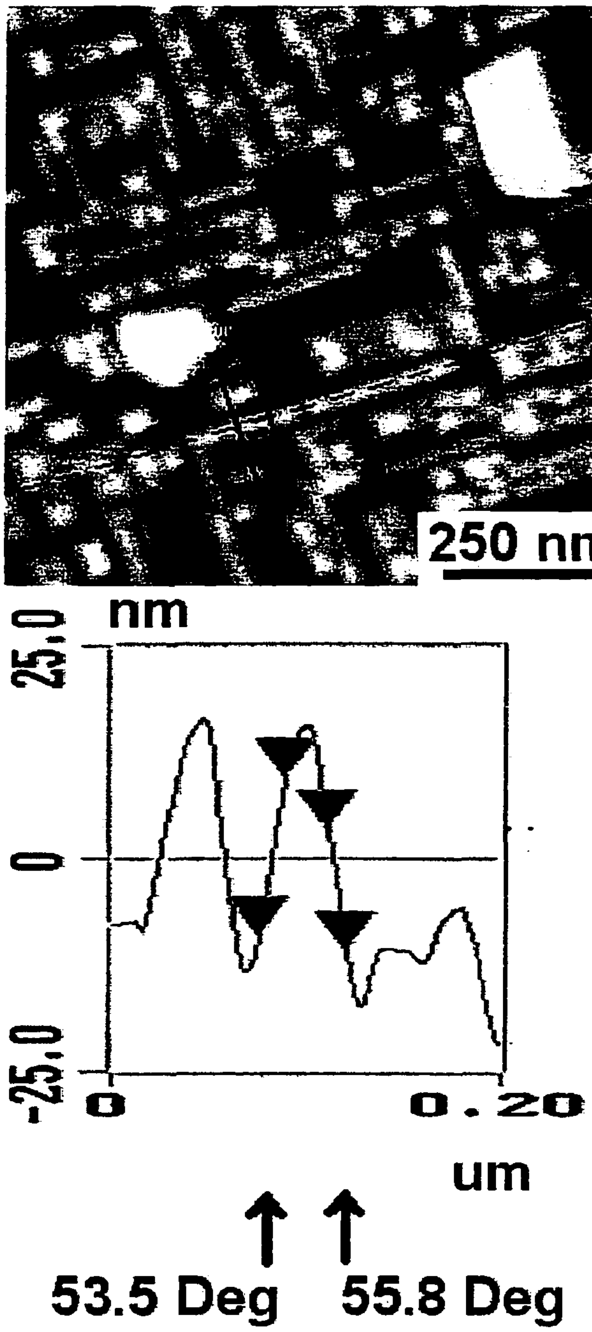

Figure 5.2: Side angles of the crystal huts. 1 μm × 1 μm. The average of the side angles is 54.7° in this case. The angle on each side is also an average within the boxed region of the image. The side angle reported in Table 5.1 is an average based on several boxed regions. The cross section of a crystal hut is also depicted by the line profile.

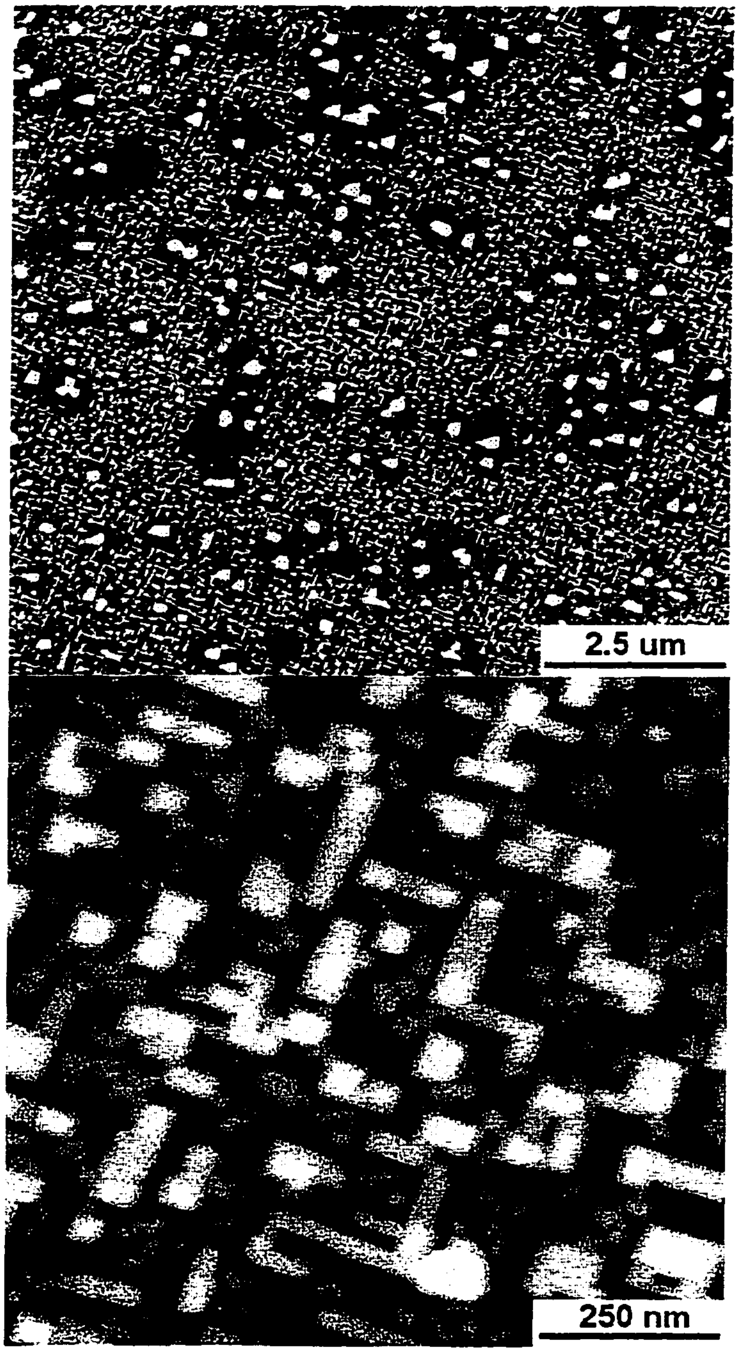

Figure 5.3: SPM images of Annealed films of CaF_2. (Top) 10 μm × 10 μm. Amorphous structures are observed to surround polycrystals. (Bottom) 1 μm × 1 μm. Flattened huts are clearly seen. Pyramids are flattened and pyramidal pits are filled. Amorphous structures are formed among the single crystals.

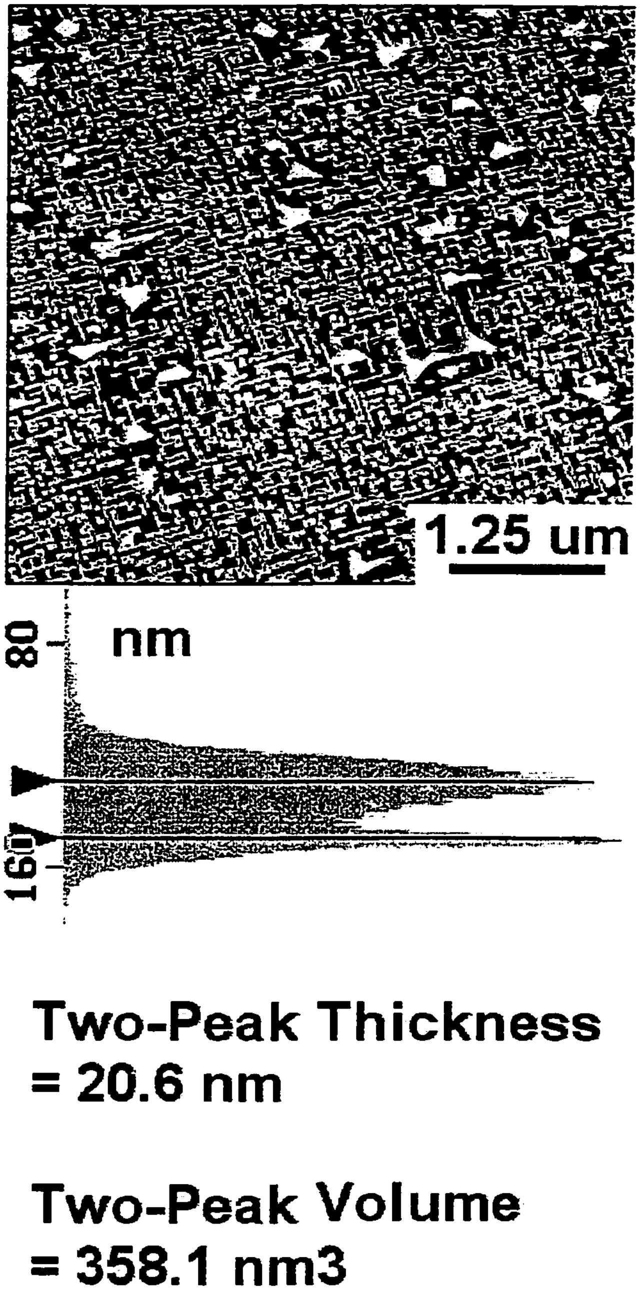

Figure 5.4: Height histogram of a MBE film showing two peaks. 5 μm × 5 μm. The values of two-peak thickness and volume are shown at the bottom. After annealing, the two peaks will move closer due to flattening of the film. The total volume of the film can be calculated using the same bearing function.

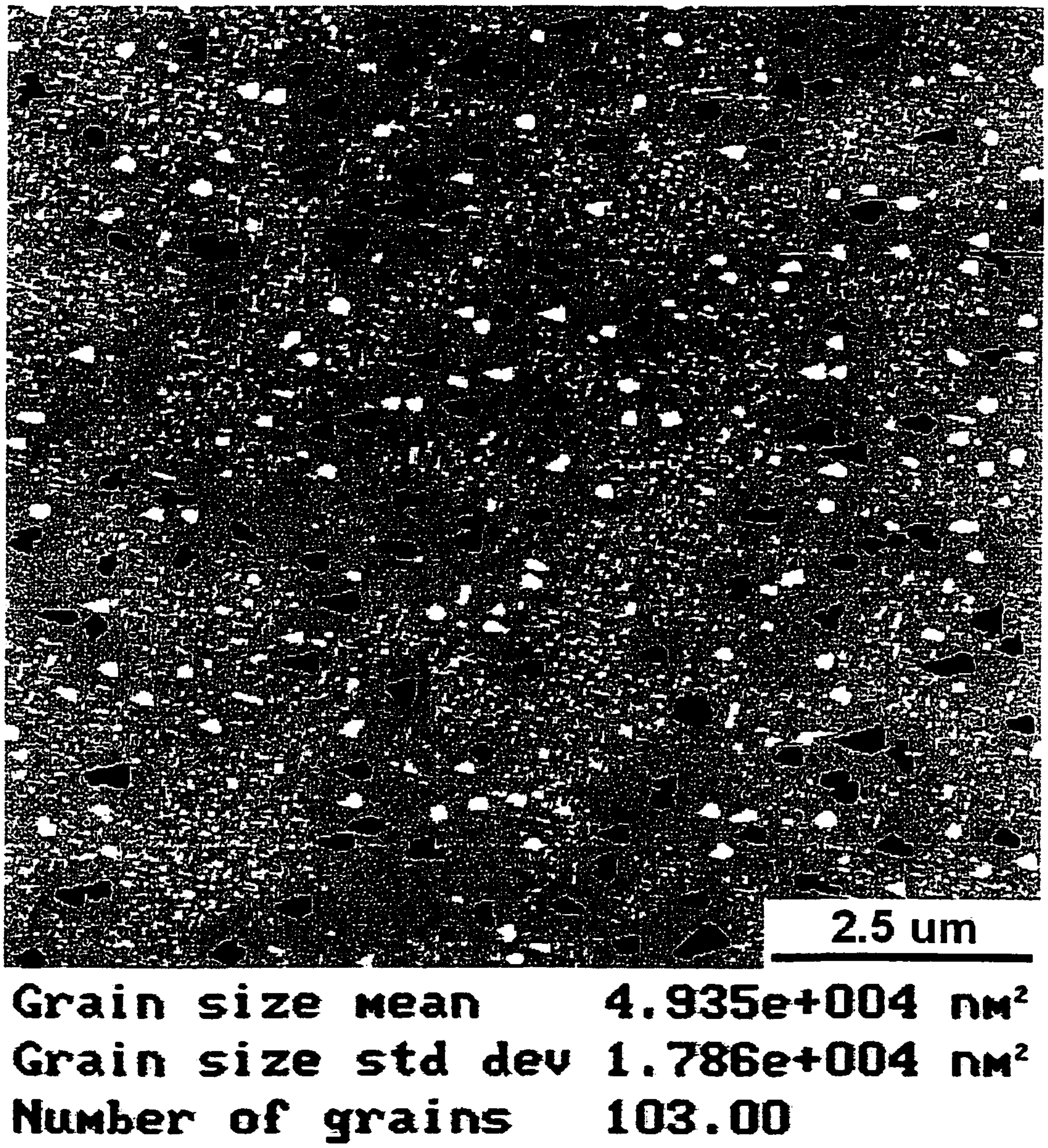

```
Grain size mean     4.935e+004 nm²
Grain size std dev  1.786e+004 nm²
Number of grains    103.00
```

Figure 5.5: The average grain size of the largest 100 polycrystals. 10 μm × 10 μm. The dark particles participate in the calculation. The number of grains per unit area or the grain distribution density may also be calculated by dividing the total number of grains with the image area.

Appendix A

Laser Tuning

Once we put the sample on the piezotube and cover the scan head over it, we have to lower the tip with the help a monocular optical microscope. Meanwhile, from the optical image shown on the tip monitor (or tip screen), we should be able to locate the probe by moving the *sample* $x - y$ positioners.

After locating the probe, we change the focus from the probe to the sample surface. If the surface is reflective enough, we can find a shiny laser spot reflected by the sample. Tune the *laser* $x-y$ positioners, one at a time with x direction first, to move the spot around while checking the 'sum' signal (the reflection received by the whole photo-detector) expressed as an elliptical bar in the bottom LED panel of the body. Stop tuning when the bar reaches maximum and indicates the laser beam has been relocated onto the tip. Then tune the y positioner and stop when the signal reaches maximum. At this point, the laser beam is supposed to shine upon the probe. If we view the tip with the monocular microscope, we should be able to see a red laser spot focused on the cantilever.

If the sample has a poor reflection, it will become difficult to find the dim spot from the tip monitor, in which case we can use the so called ‘paper test’. Sliding a slip of paper into the scan head in front of the photo-detector, we may see reflected laser light on the paper by tuning the mirror and the laser positioner. Tune the laser positioner one by one and stop when we see a focused laser spot. After removing the paper, the sum signal in the LED panel should have reached a reasonable value. For TappingMode silicon I-tip, the value should be 3.5 volts or higher. For contact mode Si_3N_4 V-tip, the value can be as large as 9 volts, depending on the available reflection area of the cantilevers.

After focusing the laser beam on the cantilever, lower the probe again using the monocular optical microscope. One red spot will be observed which roughly indicates the position of the free end of the probe. However, we need to bear in mind that the lowest point of the crystal beneath the cantilever is below the red spot. When the tip is close to the sample, we will start seeing 2 red spots. The top spot is the one reflected by the cantilever while the bottom one, by the sample. When the two red spots are drawn reasonably close , stop lowering the tip and fine tune the laser beam. Note for transparent samples like mica, the reflected red spot may come from the deeper layers of mica. So care must be taken not to crash the tip. Getting the tip close to the sample helps save the automatic tip engaging time and position the tip in the desired region of the sample more accurately. If the tip touches the sample physically during the tip lowering, we will see on the screen the tip bend with an intense reflection. Sometimes the cantilever is found broken with debris.

At this point, we should be able to see clearly both the cantilever and the laser spot on the screen. Normally, we want to move the spot closer to the free end of the cantilever so the laser beam may have maximum sensitivity to small tip deflection. However, if the spot goes over the free end, the sum signal will drop quickly and the spilled laser light over the free end will be reflected back from the sample surface, causing unwanted interference with the directly reflected laser beam and resulting in wavy SPM images. There is a trade off between sensitivity and intensity so optimization and practice are required.

If the sum signal seems too low after tuning the laser positioners and photodiodes. We need to tune the mirror. If tuning the mirror still does not help. We need to realign the tip in the tip mount, namely, to take it out and re-slide it in. Sometimes the tip is bent heavily by electrostatic charges on the sample and a shiny tip is seen on the screen. We can try to neutralize the static charge by using ionized air or grounding the sample. In most cases, replacing the tip is the best solution.

Appendix B

Probe Cleaning

In addition to sample preparation, the quality of the tip is another key to successful SPM work. Poor quality images may come from the tip defects such as split tip or broken tip. The tip may be worn out or get blunt due to scanning on hard surfaces, which reduces the image quality. In both cases replacing the tip is unavoidable. If scanning plastic or soft materials, the tip may be contaminated by the sample and render noisy images. Cleaning the tip before/after use is a good way to maintain the image quality. Practical ways of tip cleaning are presented below.

B.1 Ultrasonic Bath

Ultrasonic bath is a good way to clean organic contaminants. Ethanol, acetone, or detergent may be added in proper quantity to help remove dirt from the tip. Several baths may be necessary to ensure satisfactory cleaning. However, care needs to be taken to smoothly immerse and take out the tip from the solution without breaking the cantilever.

B.2 UV Laser

In scanning polymer samples, UV laser was proved to be very useful for burning out or degrading the sample debris picked up by the tip. Be sure to wear a UV proof goggle in using the UV laser pen. During the irradiation the whole setup including the laser and tip should be at least well covered by a common paper box to avoid direct contact of the eye with invisible UV light. The time duration can range from 40 min to 1 or 2 h.

UV laser can also be used to remove a portion of a thin film sample and create a film edge for thickness measurement.

B.3 In Situ High Frequency Shaking

Sometimes the tip catches dirt particles close to it during scanning. One is able to remove such particle attachment by increasing the integral gains to a large value (say, from 5 to 30) for a few seconds. Mostly the particle will be cast away. Care must be taken, however, as doing this may crash the tip on the tall features of the sample if the surface is rough.

Appendix C

Tip Handling

C.1 General Care

In no case should you blow the tip with air or the mouth because the cantilever will be broken. The side of the tip with the crystal should always face up. If not, the crystal should have touched some foreign surface already. Be careful not to drop the box with tips even at a small distance above the table. Otherwise the tips may break.

C.2 Use Tweezers

90° curved tip tweezers are found to be most useful in handling SPM probes and samples. For an experienced worker, one such tweezers is enough to take a new tip from the wafer without damaging the tip or something else. However, practice is needed.

To insert the tip into the groove of the tip mount (Fig. 1.1: f). Release the spring clip fully by pressing down the tip mount with one hand while sliding in the tip quickly with the other hand. After inserting the tip, align the tip with respect to the groove with the clip only slightly released.

C.3 Use All the Cantilevers

SPM tips usually come with several cantilevers, 2 or 3 with different sizes on each of the short sides of the substrate. For routine scanning on smooth samples, one can use the longest cantilever first and then go on with shorter ones. The long cantilevers will touch the surface before the short ones so we need to use them first and leave others intact. After using up the cantilevers on one side, we can take out the whole tip and slide it back with the new cantilevers on the other side ready for use. In this way we can use the tip more economically. However, if the sample is rough, some of the short cantilevers may be damaged before use.

C.4 Store Used Tips

After the tip needs to be replaced, it can be stored in a plastic dish/box with a layer of weak glue or a piece of double sided tape for future use like practicing new scanning techniques (Fig. 1.8).

Appendix D

Image Processing

The SPM comes with an off-line software which allows us to modify or analyze the captured images in addition to the real-time control console interface. An image will only offer descriptive information but image processing and analysis will provide more quantitative data as needed in scientific work.

A few essential functions of SPM image processing will be discussed below. Image processing basically changes or modifies the images in order to extract more and meaningful results while not to distort or introduce artifacts to the images. The most commonly used functions remove the image tilting due to unevenly mounted samples or pendulum-like motion of the piezotube, remove the noise lines due to unstable interaction between the tip and sample, and isolate a portion of the image to save as a new file. Other functions such as sharpening, smoothing, inverting, and resizing are used less.

D.1 Plane Fit: Polynomial Fit

Plane fit is the most important function used to level the image. It is simply a 2D curve fitting of the imaged surface with first (plane), second, and third order polynomials. The fitting polynomial is the 'model' of shape we assume our fitted surface follows. A surface can be modeled by a function like $z^* = f(x, y)$ where z^* is the modeled or regressed height of each constituent element of the surface at the location (x, y) of a basal plane. If the surface resembles a plane, we may assume $z^* = f(x, y) = a + bx + cy$, which is first order. If the surface is like a cylinder, it can be modeled by $z^* = f(x, y) = a+bx+cy+dx^2+ey^2+gxy$ (second order) or by some simpler forms with fewer terms. When we do the plane fit with the SPM software, we can only work along one direction (x or y) at a time which indicates a simplified form like $z^* = f(x) = a + bx + dx^2$ (x direction, second order) or $z^* = f(y) = a + cy$ (y direction, first order) is used. However, we are able to export our image to Mathematica (to be discussed) and perform the 2D regression using $z^* = f(x, y)$.

D.1.1 First Order

First order plane fit did not distort the image at all except for leveling so it is performed on almost every image. Note we can save our image in 'offset' or 'line' mode (specified in the real-time control panel). The offset mode will normally give us an unrecognizable image half bright and half dark due to the tilting of the sample (Fig. D.1: top). First order plane fit can be applied to such an image to remove the tilting and reveal the surface morphology. If we save the image in line mode, the image will be processed by the 'flatten' function (to be discussed) which normally distorts the image (permanently) and leads to artifacts. Therefore we better save the image in offset mode while we can view it during scanning in line mode. We can still apply the flatten function to the image later in off-line processing if needed.

The first order plane fit subtracts the regression model, $z^* = f(x)\ or\ f(y)$, from the image $z = an\ array\ of\ data$. We can express our image by $z = z^* + \Delta z$ where Δz is the error between the data z and the model z^* and can, in a sense, be considered as random noises to the model. After subtraction what we get is simply Δz which is suitable for measuring the surface roughness (Fig. D.2: second row) because tilting may exaggerate the value.

D.1.2 Second Order

If we want to measure the surface roughness of fiber, we can utilize the second order plane fit such as $z^* = f(x, x^2)$ to flatten the fiber (Fig. D.2: third row). However, before capturing an image, the scan direction should be adjusted to either parallel or perpendicular to the fiber because second order plane fit will not work if the feature in the image is aligned in the diagonal direction. Second order plane fit is good at flattening a hemicylindrical surface.

If an image shows large particles scattered on a surface, the planar regions around the particles can be selected to produce a model surface for leveling the whole image. Fig. 1.5 shows the two steps to level a tilted image of the calibration grid. Either x or y direction can be taken first for leveling. The y direction is regressed in second order while the x direction, in first order. In this case,the so called 'passband' was used to select several regions of interest as regression reference at the same time.

The passband is a 2D box. For regression in the x direction, data of each column in the box (e.g., $z_{3,j}$) are averaged first to give a value like $\overline{z_3}$. Next all the $\overline{z_i}$ in the box are fitted by a polynomial. Therefore, plane fit works on a list of averaged heights.

D.1.3 Third Order

Third order plane fit (Fig. D.2: bottom row) is useful in removing the bow or wave of an image (Fig. D.1: bottom) at a large scan size and the processed result is shown in Fig. 1.4: top. Note second order plane fit may also work in this case. However, for a wave- or saddle-like surface, third order plane fit (e.g., $z^* = f(x, x^2, x^3)$) is more efficient.

D.2 Flatten

Flatten is a stronger function to level a surface by smoothing out the tall/deep features in the image. For example, after applying a third order flatten to the calibration grid, false protrusions are observed (Fig. D.3). The result substantially changed the height distribution and roughness of a surface, resulting in significant distortion of the surface. The mathematics of flatten is similar to that of plane fit but flatten works on the image line by line. That is, each line but not a group of lines produces a polynomial. Therefore, stopband instead of passband is used to exclude the regions of little interest.

D.2.1 Stop Band/Box

In order to avoid the artifact contribution from tall features, one needs to use stopbands or excluding boxes to cover those features (Fig. D.4). For example, if we want to flatten an image with a lot of particles, we need to cover each particle with a stopband.

D.2.2 Zeroth Order

The purpose of the flatten function is to remove the image bow or sudden jump between successive scan lines induced by vibration or vertical thermal drifting of the piezotube. Sometimes the discontinuity between scan lines is not avoidable and we normally apply the lowest level of flattening (the zeroth order) to the image. Higher order flattening may still be used for a smoother surface. The zeroth order flatten actually removes the offset of each profile (i.e., its mean height) from the zero line (i.e., the x axis). Therefore, each profile is shifted to the zero line and the discontinuity is removed (Fig. D.2: top row).

D.3 Erase

Sometime the scanning tip makes a jump due to unstable interaction with the sample and result in noisy lines in the images. If the noisy lines are few, they can be removed by the function 'erase' which simply drops the noisy line and interpolates the lines beside it. Many noisy lines, however, suggest poor scanning parameters, sticky sample, electrostatic charge, contaminated tip, small force constant, and need to change the tip.

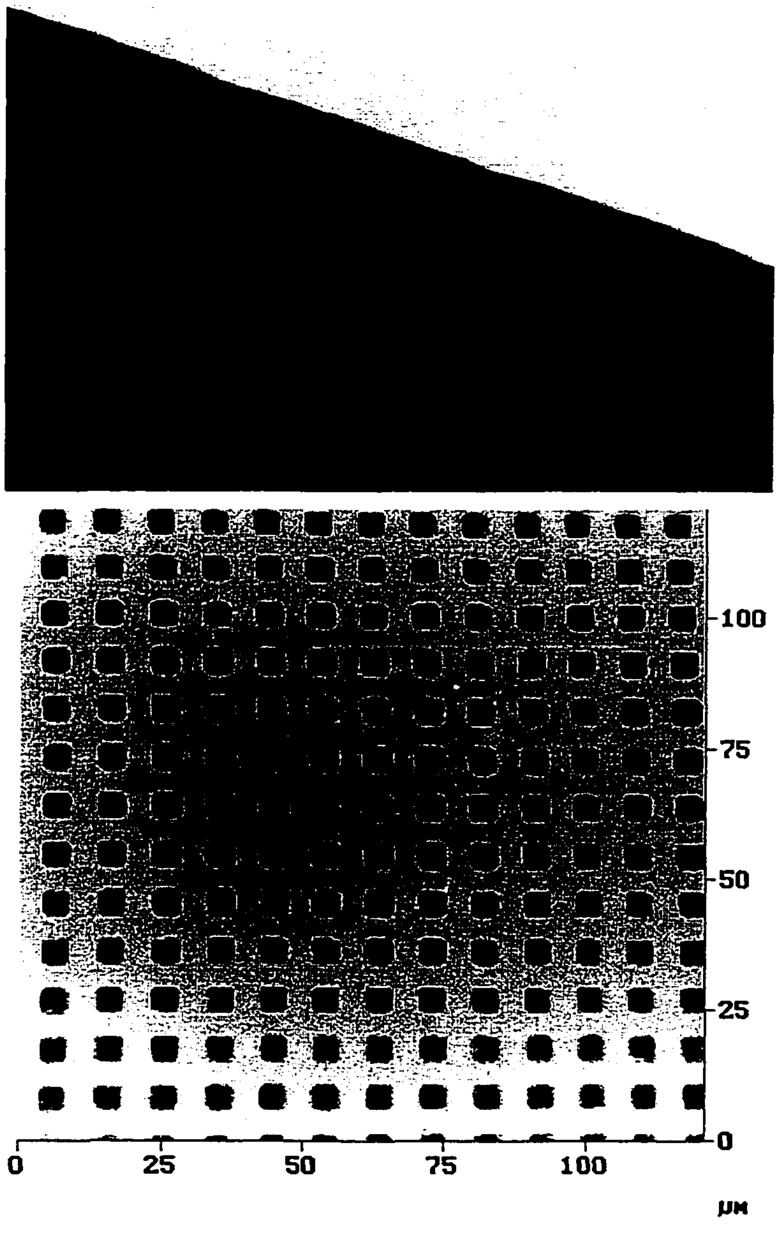

Figure D.1: Top: an inclined image due to the relative tilting of a sample with respect to the scanning tip. Bottom: a bow (a concave region) observed in the SPM image of a truly flat surface. It mostly occurs when the scan size is large.

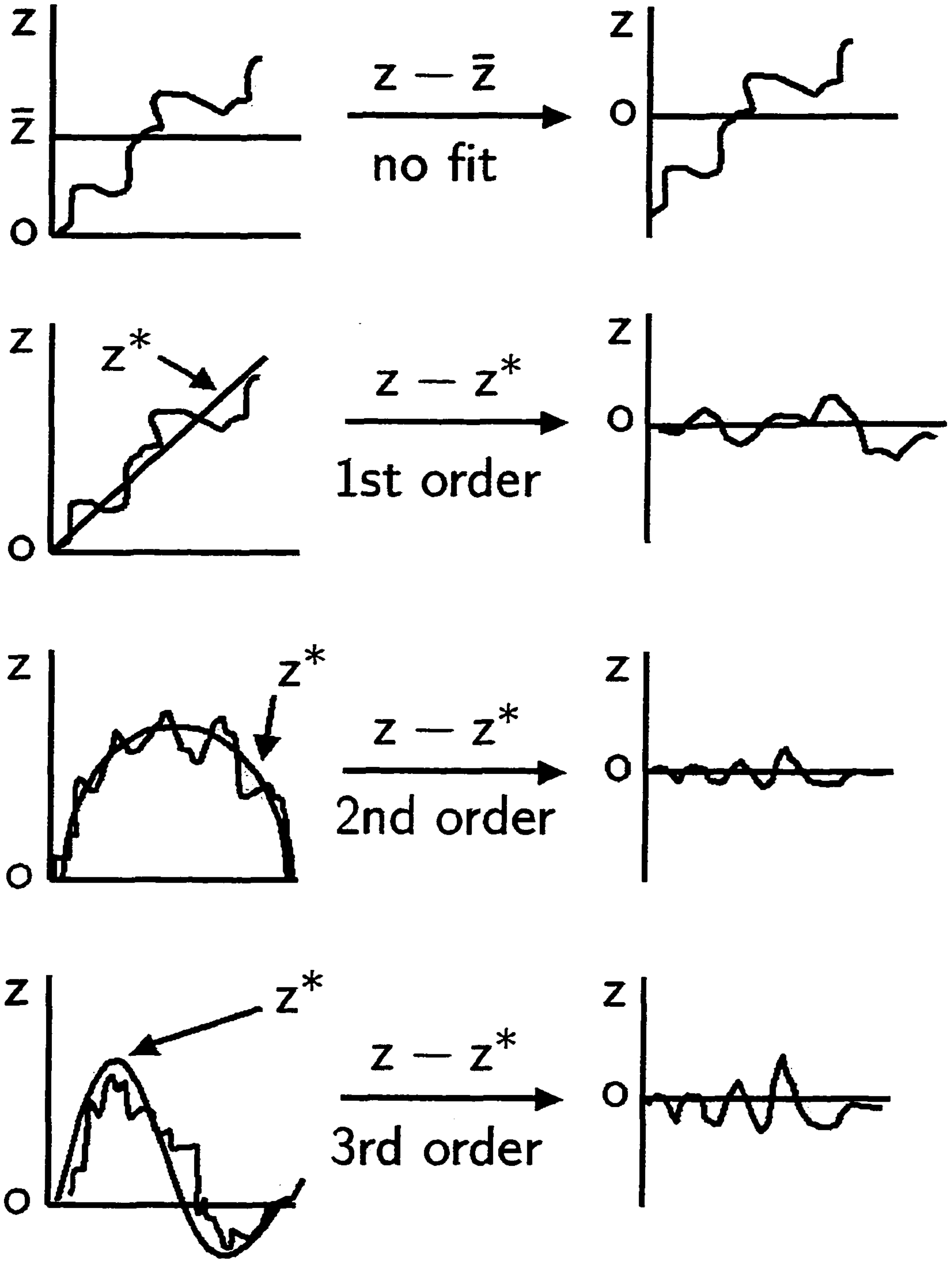

Figure D.2: Schemes of plane fit used in image leveling. Top row: subtracting a surface profile by its mean to remove the 'offset' from the zero line (x axis). Second row: first order (linear) least-squares fit of the surface profile to remove the 'tilt'. Third row: second order (parabolic) least-squares fit of the surface profile to remove the 'bow'. Bottom row: third order least-squares fit of the surface profile to remove the 'wave' of the profile.

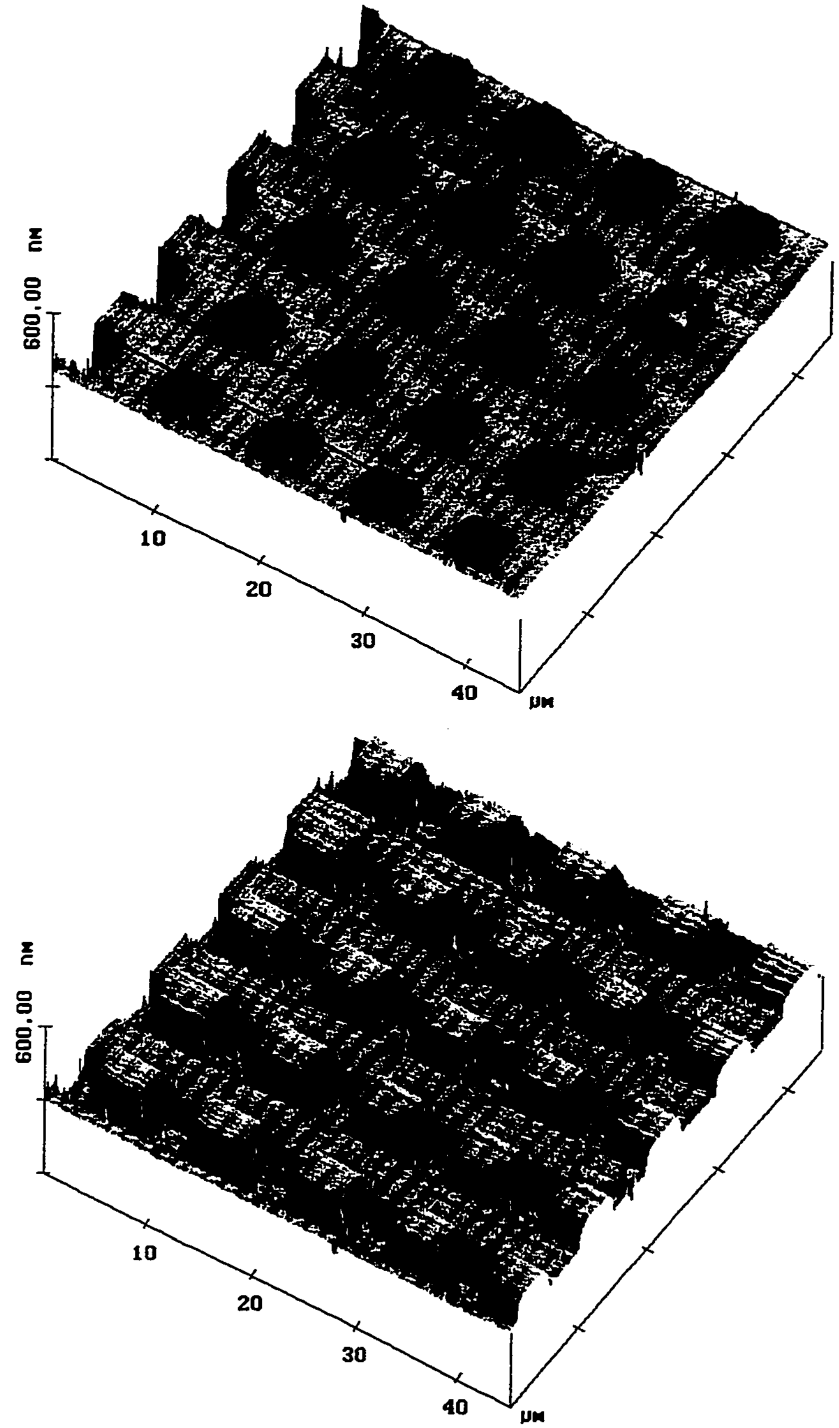

Figure D.3: Top: 3D view of a calibration grid imaged using SPM. Periodic pits are observed. Bottom: 3D view of the grid after a second order flattening applied to the image. Several bands of the no-pit region were pressed down.

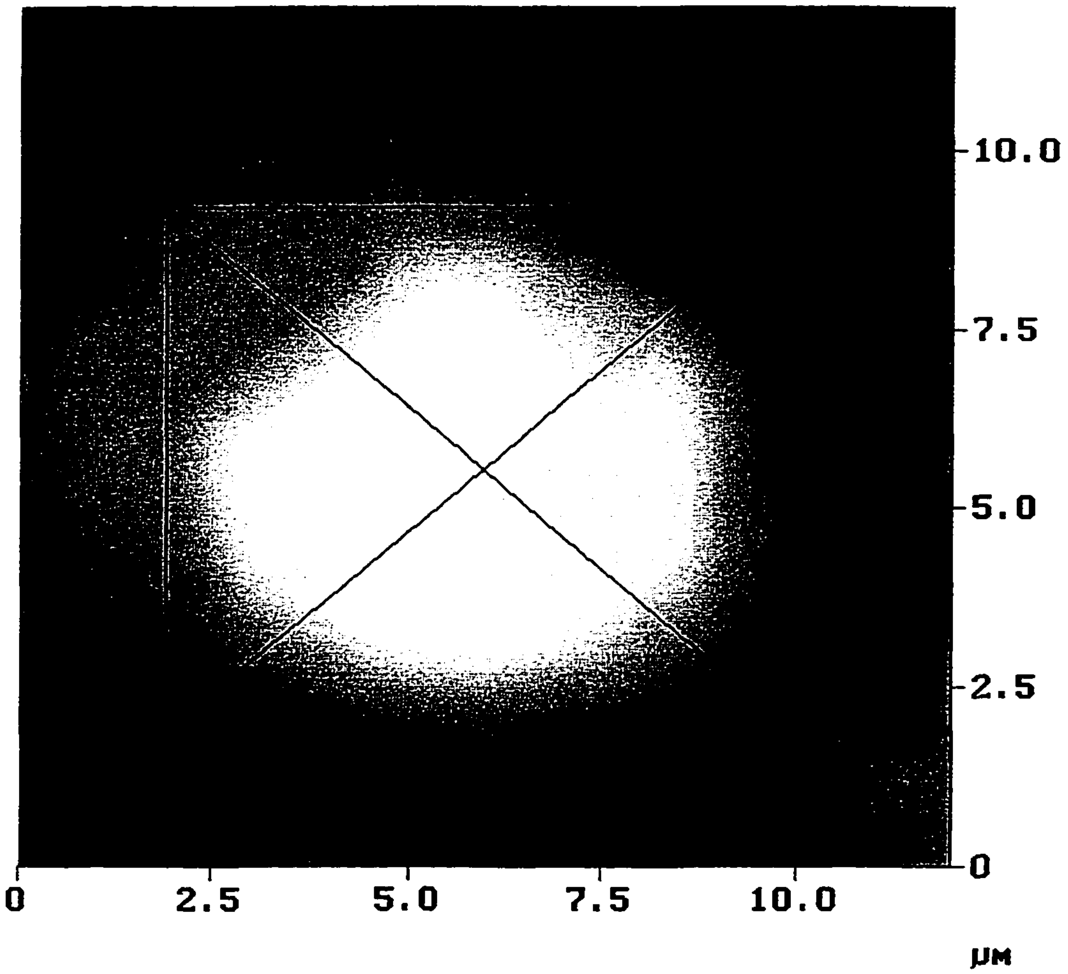

Figure D.4: In order to avoid artifact due to image processing on a surface with pits or particles, stopband is normally used to exclude those prominent features from being processed. The stopband is a box with a cross inside. Sometimes we need to use the passband (a box without a cross) to select the regions for processing, depending on which band is more efficient.

Appendix E

Image Analysis

Image analysis is important to establish structure-property relations of the sample in a quantitative way. Image analysis can be done with the supplied SPM off-line functions or by exporting it to a third-party software like Mathematica or NIH image. The third-party software allows the user to write their own programs or macros for specific purposes that have not been addressed by the SPM software. Several commercial softwares are also available but writing one's own programs can be very instructive in learning image analysis.

E.1 Observation Under Optical Microscope

One important purpose of image analysis is to identify specific features to compare any small difference or to contrast any large difference between samples prepared under different conditions. Some features may have a size beyond the capacity of

SPM that we may need other techniques such as optical microscopy to complement our analysis. For example, in samples with corroded surface, there may be large pores present which can be readily seen under an optical microscope in addition to the nanopores detected by SPM. It is a good habit to make a careful and complete observation of a sample before interpreting the SPM images.

E.2 Statistics

Image analysis requires understanding and application of statistics. SPM images are mostly on the μm scale, referring to only several 'points' on the sample. In order to show the reproducibility of a sample, three different locations on the sample are the minimum requirement to be scanned. All the measured quantities from the sample images are then averaged and analyzed statistically. A statistical study simply means you collect a set of numbers to sum up and average.

Sometimes, for a large sized image which is known to be typical of the surface, one can analyze different locations of the image based on a suitable small processing area and obtain several values for statistical calculation. For example, on a surface 5 μm × 5 μm, we can measure the roughness of a 1 μm × 1 μm area at several locations if the area is large enough to encompass the features of interest. Working with multiple images, which further increases the number of samples and improves the average, we still need to avoid anomalous features like huge particles or defects by specifying excluded regions (stopbands) to reduce any unrelated bias that might get in the statistics.

E.3 Surface Mean and Variance

The mean height of a surface can be mathematically expressed in either continuous or discrete form

$$\bar{z} = \frac{\int\int z\,dx\,dy}{\int\int dx\,dy} = \frac{\sum_i \sum_j z_{i,j}}{N}, \tag{E.1}$$

where N is the total number of pixels in the image. An important property of the surface mean is

$$0 = \int\int (z - \bar{z})\,dx\,dy = \sum_i \sum_j (z_{i,j} - \bar{z}), \tag{E.2}$$

which means the total volume above (a positive value) and below (a negative value) the surface mean is zero. Surface mean as a plane is parallel to the $x - y$ plane. In a 2D case, it means the total areas above and below the profile mean are equal.

The variance of the surface is the second moment of z. Its square root is called the standard deviation (σ_z), root-mean-square roughness (Rq), or the interface width (ω). Its continuous and discrete forms are expressed as

$$\sigma_z^2 = \frac{\int\int (z - \bar{z})^2\,dx\,dy}{\int\int dx\,dy} = \frac{\sum_i \sum_j (z_{i,j} - \bar{z})^2}{N}, \tag{E.3}$$

where σ_z is the standard deviation of z and N is the total number of pixels in the image.

E.4 Mean Roughness: Ra

The mean roughness, Ra, is measured relative to the so called 'center plane' (z_c) which slices through the surface, giving an equal amount of enclosed volume above and below the plane. As mentioned before, surface captured by SPM can be taken as a mapping of plane point (x, y) into height z and modeled by $z^* = f(x, y)$. From z we get the 'mean plane' as termed in the manual or the 'fitting plane' (z^*) which is the first order least-squares fit of the surface, $z^* = a + bx + cy$, and the 'fitted surface', $z_2 = z - z^*$. From z_2 (the leveled surface) we can calculate its new mean $\overline{z_2}$ which is just the center plane, $z_c = \overline{z_2}$ for all (x, y), and the final 'shifted surface' (z_3) of which the mean $\overline{z_3}$ becomes zero and $z_3 = z_2 - z_c$. The total volume (with signs) enclosed by z_2 with respect to z_c is zero and so does z_3 to the xy (zero) plane (Fig. E.1: the signed areas of the shaded regions cancel out). Consequently, Ra is defined as the mean deviation of z_3 which can be expressed by

$$\mathrm{Ra} = \frac{\int\int |z_3|\; dx\, dy}{\int\int dx\, dy} = \frac{\sum_i \sum_j |z_3|_{(i,j)}}{N} \tag{E.4}$$

and is generally used as a measure of global surface roughness.

Note here we have two kinds of deviation. One is the standard deviation and the other, the mean deviation. The former is calculated with respect to the surface mean while the latter, the center plane. Both the square and absolute operators incorporated in the respective definitions are meant to make all the deviations positive. Therefore, the average of the positive deviations becomes a measure of 'distance' between the surface and the reference plane used.

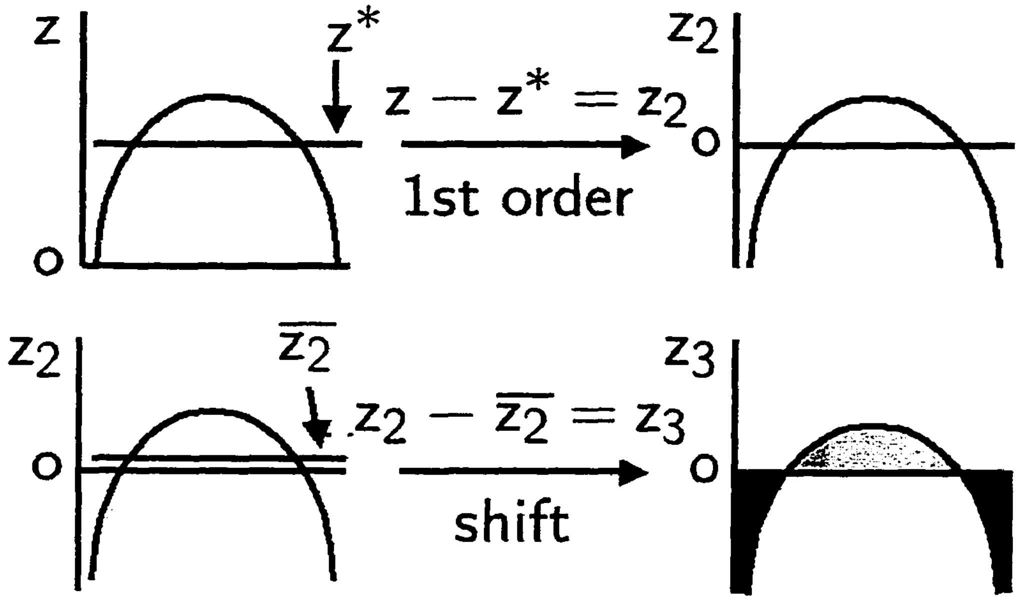

Figure E.1: Schemes for calculating mean roughness. Top row: first order plane fit is applied to the surface profile to remove any tilting. Bottom row: the leveled profile is shifted with respect to its mean line. The mean roughness is calculated as the mean deviation of the shifted profile. The integration of the shifted curve or the sum of the shaded and signed areas is zero.

Appendix F

Image Files

F.1 Image Export and Print

In the laboratory setup, both optical and SPM images can be printed by a thermal (dye-sublimation) printer or saved as electronic image files. Electronic images are getting more important and attractive because they save the cost of printing and can be converted into other formats and incorporated into a computer document or presentation easily.

Recently, a low cost digital camera designed for internet meeting has been successfully set up to import the signals from the optical microscope directly into a computer. Since the scanned AFM images on a small scale can also be saved as common computer graphics (such as TIFF), the saved graphic files of optical images provide additional useful and large scale information of the sample surface. The saved images can either be printed by the thermal printer or other ink-jet color printers at a reduced cost.

F.2 File Format

The original AFM image files are composed of a header part and a data part. The file header contains all the scanning parameters (in recognizable text) while the data part, an array of height data in binary format (unreadable). Each binary data (representing one pixel) has two bytes (two ASCII characters) and can be converted into an 'integer' (with signs but no decimals) between -32,768 and +32,767. The header part (ended with an ASCII code, Ctrl-z) occupies a total of 8192 bytes (characters) for a single image file and the data part has $256 \times 256 \times 2 \approx 131$ Kb (kilo-bytes) for an image resolution of 256×256 pixels. That is, if we open the image file by a text editor, starting from the data part, every two symbols represent the height of a pixel. The total number of symbol pairs is equal to the total number of pixels, starting form left to right and bottom to top in the image. However, for a 512×512 image, the file size increases by 4 times and reaches 0.5 Mb (mega-bytes) which is quite a large size and the computer hard drive will soon be consumed if we keep using such a high resolution.

If we convert the binary data into signed integers (in LSB format, least-significant-byte-first, 16 bit), we need to further use a formula to convert those integers into the real heights with units (nm or μm)

$$z = \frac{zscale * (height\ datum)}{65,536}\ nm, \tag{F.1}$$

where *zscale* can be found in the image file header.

In summary,

$$\begin{aligned}
\textit{one height datum} &= \textit{signed integer between } -2^{15} \sim +2^{15} \\
&= \textit{one binary number} \\
&= \textit{two bytes} \\
&= \textit{two ASCII characters} \\
&= 128 \times 128 \textit{ variations} \\
&= 2^{16} \textit{ variations} \\
&= 64\ K \textit{ variations} \\
&= \textit{unsigned integer between } 0 \sim 65,536.
\end{aligned}$$

F.3 Mathematica Program

A Mathematica program has been written to import the original AFM image file and re-display it on screen (2D or 3D) or save it into common computer graphics. The program can and has been expanded to perform some analytical calculations and image processing, including roughness, volume, plane fit, etc., as the SPM software does.

```
(****************************************************)
Programs to import, export, and display SPM images
of Digital Instruments in Mathematica4
Written by Wei-Li Yuan
(****************************************************)
(*turn off spelling warning*)
Off[General::spell];
Off[General::spell1];
(****************************************************)
(*set up the Working, Input, and Output directories*)
dirW = "c:\\WLY.MMA\\work";
dirI = "c:\\wly.mma\\input";
dirO = "c:\\wly.mma\\output";
(*change the directory*)
SetDirectory[dirW];
(*given an input image file name*)
fnI = "spm-image.007";
(*define the output image file name, here we change the file extension*)
fnO = StringJoin[{StringDrop[fnI, -4], ".txt"}]
(****************************************************)
(*input the MMA packages for binary file input*)
<< Experimental`
```

```
Experimental`BinaryImport;

Experimental`BinaryExport;

(*************************************************)

(*the program is used to import the original SPM images*)

(*this program is able to discern multiple images in one file*)

Clear[fetchB16];

fetchB16[fname_] := (

      fB1601 = OpenRead[fname, DOSTextFormat -> False];

      SetStreamPosition[fB1601, 8192];

      fB1602 = BinaryImport[fB1601, {"Integer16" ..}];

      Close[fB1601];

      fB1603 = Length[fB1602];

      fB1604 = Sqrt[Length[fB1602]];

      Which[fB1603 <= 512, fB16flag = "1D"; fB1605 = fB1602, IntegerQ[fB1604],

        fB16flag = "2D"; fB1605 = Partition[fB1602, fB1604],

        IntegerQ[Sqrt[fB1603/2]], fB16flag = "2Dx2"; fB1604 = Sqrt[fB1603/2];

        fB1605 = Partition[fB1602, fB1604], IntegerQ[Sqrt[fB1603/3]],

        fB16flag = "2Dx3"; fB1604 = Sqrt[fB1603/3];

        fB1605 = Partition[fB1602, fB1604]];

      fB1602 = Null;

      fB1605

      );
```

```
(***************************************************)
(*this program is used to export the processed (new) image to be displayed
by DI's software using the same file header of the imported image*)
Clear[backUpB16];
backUpB16[x_, fname_:fnO, fin_:fnI] :=
  Module[{r, w},
    SetDirectory[dirO];
    If[MemberQ[FileNames[], fname], DeleteFile[fname]];
    w = OpenAppend[fname];
    SetDirectory[dirI];
    r = OpenRead[fnI, DOSTextFormat -> False];
    SetDirectory[dirO];
    BinaryExport[w, BinaryImport[r, "Integer16", 4096],
                {"Integer16" ..}];
    BinaryExport[w, Round[x], {"Integer16" ..}];
    Close[r];
    Close[w];
    SetDirectory[dirW];
    ]
(***************************************************)
(*this program searches the last value of scan size because
if the image has been resized or zoomed, two scan sizes will appear
```

```
in the file header and the latter is the new scan size we want*)

(*this program also convert the scan size into nm*)

Clear[findLast];

findLast[stream_, s_] :=

    Module[{t, p},

        SetStreamPosition[stream, 1];

        t = FindList[stream, s];

        If[t != {},

            t = ToString[Last[t]];

            t = StringDrop[t, StringLength[s]];

            t = StringReplace[t, "~m" -> "1000 nm"];

            p = StringPosition[t, "nm",

                    Overlaps -> False];

            If[Length[p] != 0,

                t = StringTake[t, p[[1, 2]]]

            ];

            t = ToExpression[t];

        ];

        t

    ];

(**************************************************)

(*this program searches the important parameters of the file header,
```

```
which can also read old DI image files*)

Clear[param];

param[fname_] := (

      dataFile = fname;

      stmI = OpenRead[dataFile];

      nm = 1.;

      um = 1000.;

      old = False;

      p[1] = findLast[stmI, "\Z atten.:"];

      p[2] = findLast[stmI, "\Z sensitivity:"];

      p[3] = findLast[stmI, "\Z max:"];

      p[4] = findLast[stmI, "\Samps/line:"];

      If[p[4] > 512, p[4] = Sqrt[p[4]]];(*for the old DI file format*)

      p[5] = findLast[stmI, "\Scan size:"];

      p[6] = findLast[stmI, "\Z scale:"];

      If[p[6] == {},

        p[6] = findLast[stmI, "\Z scale height:"];

        p[7] = findLast[stmI, "\Z scale auxa:"];

        p[8] = findLast[stmI, "\Z scale defl:"];

        old = True];

      Close[stmI];

      zAtten = p[1];
```

```
zSense = p[2];

zMaxn = p[3];

sPnts = p[4];

sSize = p[5];

If[TrueQ[old],

  Print["*Note: This image is in OLD format"];

  Print["The \Z scale height = ", p[6]];

  zScale = p[6]*(zAtten/65536)*(zMaxn*2/65536)*zSense,

  zScale = p[6]

  ];

cvf = (sSize/ (sPnts))^2 * (zScale/ 65536);

cvLine = sSize/ (sPnts);

cvArea = (sSize/ (sPnts))^2;

cvHeight = (zScale/ 65536);

cvVolume = cvArea*cvHeight;

sj = StringJoin[

    "1. dataFile = ", dataFile, "\n",

    "2. Conversion Factor = ", ToString[cvf], "\n", "\n",

    "a. sSize = ", ToString[sSize], "\n",

    "b. zSense = ", ToString[zSense], "\n",

    "c. zMaxn = ", ToString[zMaxn], "\n",

    "d. sPnts = ", ToString[sPnts], "\n",
```

```
        "e. zAtten = ", ToString[zAtten], "\n",
        "f. zScale = ", ToString[zScale // N]
        ];
    Print[sj]
    );
(****************************************************)
(*this program calculate the total volume under the surface
by simply adding up all the pixel heights and multiplying
the sum with the conversion factor*)
Clear[tV];
tV[tva_?MatrixQ] := tV[Flatten[tva]];
tV[tva_] := (
    tvb = Plus @@ tva;
    Print["The Conversion Factor = ", cvVolume];
    Print["The volume w/o conversion = ", tvb];
    tvc = tvb * cvVolume;
    Print["The volume w/ conversion = ", tvc];
    tvc // N
    );
(****************************************************)
(*this program can display one or several SPM images in 2D*)
ClearAll[ldp];
```

```
ldp[0][mt_ /; Length[mt] <= 3, opts___] := Map[ldp[0][#, opts] &, mt];

ldp[1][mt_ /; Length[mt] <= 3, opts___] := Map[ldp[1][#, opts] &, mt];

ldp[0][mt_, opts___] :=

    ListDensityPlot[mt, opts, Mesh -> False, ColorFunction -> GrayLevel,

      AspectRatio -> Automatic, DisplayFunction -> Identity];

ldp[1][mt_, opts___] :=

    ListDensityPlot[mt, opts, Mesh -> False, ColorFunction -> GrayLevel,

      AspectRatio -> Automatic];

(*************************************************)

(*this is the main program to import and display the image*)

(*Volume under the surface is also calculated*)

Clear[dimg];

dimg[fname_String, opts___] := (

      SetDirectory[dirI];

      (*Print["The image dir = ", Directory[]];*)

      zor = fetchB16[fname];

      Print["*All the image file parameters : "];

      param[fname];

      n = sPnts;

      Print["Image size = ", n, " x ", n];

      Print["The Conversion Factor = ", cvf];

      zmn = Min[zor];
```

```
      Print["zMin = ", zmn];

      zmx = Max[zor];

      Print["zMax = ", zmx];

      Print["zor => zos"];

      zos = zor - zmn;

      Print["D[zos] = ", Dimensions[zos]];

      zvol = tV[zos];

      Print["The calculated volume = ", zvol];

      Print["The image size = ", sSize];

      SetDirectory[dirW];

      mdP1 = ldp[1][#, opts]&@zos;

      );

(*****************************************************)

(*run the main program*)

dimg[dirI <> "\\" <> fnI]

(*****************************************************)
```

Appendix G

Nick Recovery by Interpolation

Nicked droplets in the AFM images are each recovered line by line by replacing the points inside the concave regions with the interpolated ones based on the convex points of the profile. As shown in Fig.G.1, the interpolated curves (dark) cover the gray profiles of the nicks and render a recovered droplet. The volume between the recovered and the nicked droplets can be calculated numerically. Sometimes, several nicks are present in one droplet (bottom) and careful interpolation is required.

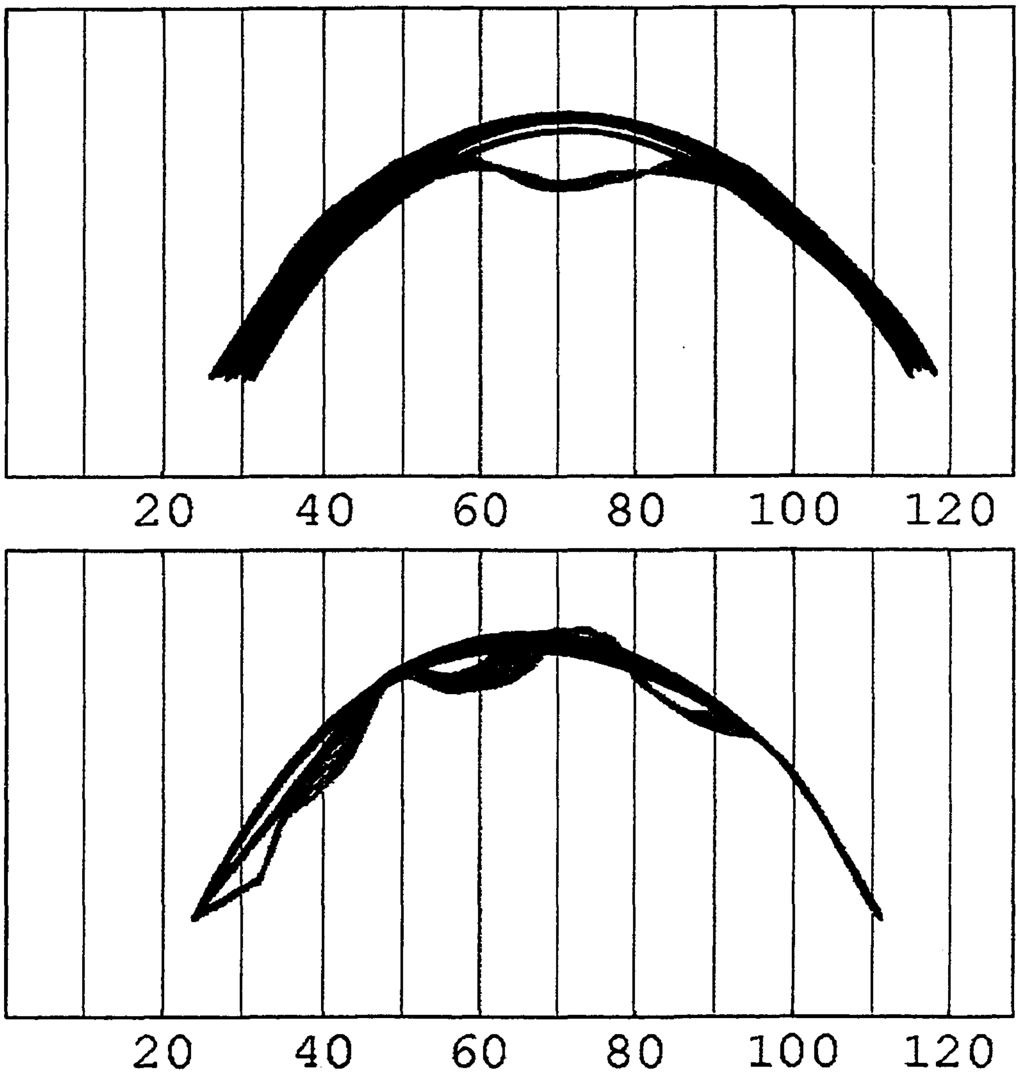

Figure G.1: Interpolation profiles (dark) and the original nick profiles (gray).

Appendix H

Volume Calculation

The volume of a droplet is calculated numerically from the data of an AFM image. Assuming all the pixel heights, $z_{i,j}$, have been shifted upward to be positive and the minimum height is zero, the simplest formula for the volume would be

$$V = (\sum_i \sum_j z_{i,j}) \times \Delta x \, \Delta y \tag{H.1}$$

where $\Delta x = \Delta y = \textit{pixel width} = \textit{Scan size/Number of points per line}$. More accurate formulae for calculating the droplet volume involve the use of Simpson's 1/3 and 3/8 rules.

The Simpson's 1/3 rule for calculating the area under a curve $(z_i)_j$ is shown in Eq. H.2

$$A_j = \frac{1}{3}\Delta x(z_1 + 4z_2 + 2z_3 + \ldots + 4z_{n-1} + z_n)_j \quad . \tag{H.2}$$

where Δx is the pixel width and n is the number of points per line. After the area under each line profile is calculated and collected, the volume can be calculated by applying the Simpson's rule to the list of areas.

$$V = \frac{1}{3}\Delta y(A_1 + 4A_2 + 2A_3 + \ldots + 4A_{n-1} + A_n) \tag{H.3}$$

where Δy is the spacing between neighboring line profiles and n is the number of A_j.

Since the number of points per line in an AFM image is even, the number of intervals in each line is odd. Therefore, we need to use Simpson's 3/8 rule to deal with the last three panels of a profile as shown in Eq. H.4

$$(A_{last\,3\,panels})_j = \frac{3}{8}\Delta x(z_{n-3} + 3z_{n-2} + 3z_{n-1} + z_n)_j \tag{H.4}$$

where Δx is the pixel width and n is the number of points per line.